Copyright Undertaking

DYNAMICS COMPUTATIONAL ANALYSIS OF PEO/PVDF/SN COMPOSITE SOLID-STATE ELECTROLYTE FOR LITHIUM-ION BATTERIES

SAIQA HAFEEZ

MPhil

The Hong Kong Polytechnic University

2024

The Hong Kong Polytechnic University

Department of Mechanical Engineering

Dynamics Computational Analysis of PEO/PVDF/SN Composite Solid-State Electrolyte for Lithium-Ion Batteries

Saiqa Hafeez

A Thesis Submitted in Partial Fulfilment of the Requirement for
the Degree of Master of Philosophy

February 2024

CERTIFICATE OF ORIGINALITY

I hereby declare that this thesis is my work and that, to the best of my knowledge and belief, it reproduces no material previously published or written, nor material that has been accepted for the award of any other degree or diploma, except where due acknowledgment has been made in the text.

HAFEEZ, SAIQA

Abstract

Lithium-ion batteries (LIBs) are widely employed in electric tools, electric cars, and mobile gadgets because of their high energy density, great power capability, and reasonable lifespan. However, conventional organic liquid electrolytes may be flammable and lead to danger of explosion at high temperatures. The demand for all-solid-state Li-ion batteries (ASSLIBs) is high because it can address the abovementioned safety concerns, and also increase energy density by using lithium metal as anode. However, ASSLIBs have several inherent issues that have to be addressed before their practical deployment, such as limited room temperature (RT) ionic conductivity (σ), and low lithium ion transference number (t^+). For polymer-based solid electrolytes, modifying the polymer host or adding some inorganic fillers or plasticizers into the polymer is shown to be effective in addressing the issues.

In the present study, polyethylene oxide (PEO), the well-known lithium ion conductive polymer is chosen as a host polymer, polyvinylidene fluoride (PVDF) as a blended polymer or binder, succinonitrile (SN) as a plasticizer to create a new plasticized blended solid polymer electrolyte (PBSPE), and lithium bis(trifluoromethane sulfonyl)imide (LiTFSI) as salt for lithium-ion sources. Before experimentally testing the new material, its properties are desired to be predicted theoretically. In this regard, the classical molecular dynamics (CMD) simulation method was employed to design and study the dynamics of ions in the proposed PEO/PVDF/SN/LiTFSI PBSPE. The concentrations of LiTFSI salt and PEO [Li: EO] varied from 0.02 to 0.20. The mass percentages of PVDF and SN changed from 0 to 40 wt.% and 0 to 25 wt.% under operating temperatures varying from 298.15 K to 363.15 K. The g(r) obtained from the CMD simulation in

this work is per the investigation in neutron diffraction experiments. The Nernst-Einstein equation was employed to measure the Li-ion and TFSI-ion diffusion coefficients.

In all cases, the first peak of radial distribution function g(r) was observed at r ≅0.210 Å, indicating the strong interaction between Li-ion and O_{PEO}. The Li-O_{PEO} coordination number (CN) of 4.9-6 has been observed. The trend for diffusion coefficients of both Li^+ and $TFSI^-$ ions are in good agreement with the literature with the highest values of 2.1×10^{-8} cm^2 s^{-1} and 4.73×10^{-8} cm^2 s^{-1}, respectively at room temperature (RT = 298.15 K). The highest ionic conductivity at RT was 1.45×10^{-4} S cm^{-1} achieved at 25 mass% of SN, which increases to 1.37×10^{-3} S cm^{-1} as the temperature reaches 363.15 K. High Li-ion transference number of 0.45 at RT has also been obtained at 10 mass % of SN. This study shows that the new composite solid-state electrolytes can be experimentally investigated for potential utilization in ASSLIBs with high performances.

Acknowledgments

All praise and adoration to Allah Almighty, the most beneficent and merciful. Firstly, I would like to thank my chief supervisor, Dr. Xiaoliang Yu from the Hong Kong Polytechnic University, and co-supervisor, Prof. Guohua Chen from City University Hong Kong, for their valuable advice, motivation and ongoing enthusiasm in following my progress on this research project. I could not have succeeded without their support. They nurtured me for an independent research program with a high impact on energy storage and ensured the availability of resources for my simulation work (from the advanced desktop system to HPC supercomputers). This is a valuable experience in the early stage of my scientific research. They also supported me in understanding the analysis of the results, report writing, and presentation, which is essential for this thesis.

I want to thank Prof. Deng Yonghong from SUSTech University, China, for providing me with a platform where I can meet people with simulation expertise. I learned a lot about the basics of simulation skills. She also helped me get financial assistance from the SUSTech University when I needed to stay there. Her research group was also very cooperative and helped me to live and adjust to a very different culture of China.

Moreover, I would like to thank Dr. Zhaowen Bai and one of my colleagues in my parent University (COMSATS), Pakistan, Mr. Ghulam Abbas Gohar. They also helped me understand some details of MD simulation software including LAMMPS and GROMACS. In addition, I am very grateful to my group member, Dr. Raza Hassan, for his great help and encouragement during my research. Finally, I would like to thank my parents, my husband, and my friends for their moral and emotional support and for taking care of my child in my homeland so that I can concentrate well on this research work. I hope everyone can be safe and happy.

Table of Contents

List of Figures

List of Tables

List of Abbreviations and Symbols

Abbrevations	**Description**
AIMD	Ab-initio Molecular Dynamics
AMBER	Assisted Model Building with Energy Refinement
ASSEs	All-Solid-State Electrolytes
ASSPEs	All-Solid-State Polymer Electrolytes
bcc	body-centered cubic
BSPE	Blended Solid Polymer Electrolyte
cg	conjugate gradient
CHARMM	Chemistry at Harvard Molecular Mechanics
CMD	Classical Molecular Dynamics
CN	Coordination Number
COM	Center of Mass
COMPASS	Condensed-phase Optimized Molecular Potentials
CSSEs	Composite Solid-State Electrolytes
DEC	Diethyl Carbonate
DFT	Density Functional Theory
DMC	Dimethyl Carbonate
DVB	Divinyl Benzene
EC	Ethyl Carbonate
EMC	Ethyl Methyl Carbonate
es	Electrostatic
ESP	Electrostatic Potential
EVs	Electric Vehicles
GROMACS	Groningen Machine for Chemical Simulations
GROMOS	Groningen Molecular Simulation
HNC	Halloysite Nano Clay
ICEs	Inorganic Ceramic Electrolytes
ISEs	Inorganic Solid Electrolytes
LATP	$Li_{1+x}Al_xTi_{2x}(PO_4)_3$
LAGP	$Li_{1+x}Al_xGe_{2x}(PO_4)_3$
LCO	$LiCoO_2$
LEs	Liquid Electrolytes
LFP	$LiFePO_4$
LGPL	Lesser General Public License
LIBs	Lithium-ion Batteries
LiBr	Lithium Bromide
LiBOB	Lithium bis(oxalate)borate

LINCS	Linear Constraint Solver
LISICON	Lithium Superionic Conductor
LiTFSI	Lithium bis(trifluoromethane sulfonyl)imide
LLZO	$Li_7La_3Zr_2O_{12}$
LLTO	Li3xLa2/3xTiO3
LMO	$LiMnO_2O_4$
LPEO	Long-chain PEO
MCS	Monte Carlo Simulation
MD	Molecular Dynamics
MS	Merial Studio
MSD	Mean Square Displacement
NASICON	Sodium Superionic Conductor
NMC	$LiNiMnCoO_2$
NPs	Nano Particles
NWs	Nano Wires
OPLS-AA	Optimized Potentials for Liquid Simulations- All atom
OPLS-UA	Optimized Potentials for Liquid Simulations- United atom
PBSPE	Plasticized Blended Solid Polymer Electrolyte
PAN	Poly(acrylonitrile)
PDB	Protein Data Bank
PE	Potential Energies
PEG	Poly(ethylene glycol)
PEGD	Poly(ethylene glycol) diacrylate
PEO	Poly(ethylene oxide)
PEI	Poly(ethyleneiodide)
PME	Particle Mesh Ewald
PMMA	Poly(methyl methacrylate
PS	Polystyrene
PSPE	Plasticized Solid Polymer Electrolyte
PVDF	Poly(vinylidene fluoride)
PVDF-HFP	Poly(vinylidene fluoride-co-hexafluoropropylene)
PVP	Polyvinylpyrrolidone
R&D	Research and Development
RDF	Radial Distribution Function
RMSD	Root Mean Square Displacement
RT	Room Temperature
sd	Steepest descent
SEI	Solid Electrolyte Interphase
SN	Succionitrile

SPEs	Solid Polymer Electrolytes
SPEEK	Sulfonated Polyether Ether Ketone
SPEO	Short-chain PEO
SSBs	Solid-State Batteries
SSEs	Solid State Electrolyte
Vdw	Van der waals forces
VMD	Visual Molecular Dynamics
VTF	Vogel-Tamman-Fulcher

Symbols	**Description**
1D	one-dimensional
3D	three-dimensional
D	Diffusion cefficient
E_{total}	Total energy
E_{kin}	Total kinetic energy
E_{pot}	Total potential energy
E_{bond}	Harmonic bond stretching
E_{angle}	Energy contribution from Angle bending
$E_{torsion}$	Torsional energetics
E_{vdw}	Total van der waals energy
E_{es}	Total electrostatic potential energy
g(r)	Radial distribution function
M_w	Molecular weight
N	Number of particles
R_g	Radius of gyration
T_g	Glass transition temperature
U_r	Interaction potential
t^+	Cationic transference number
t	time
k	force constants
r	Bond length
Θ	Angle
V	Fourier coefficients
Φ	Torsional angle
q	partial atomic charges
σ	Lennard-Jones radii
ε	well depths
ϵ_o	absolute dielectric permittivity
π	pi
ρ	Density

Chapter 1. Introduction

1.1 Background of Batteries

The role of energy in human civilization is of utmost importance, serving as a fundamental source of heat, light, and mechanical power. Over the past few decades, there has been a steady rise in the global population and also an increase in energy consumption per capita. [1] [2] Since the first industrial revolution, there have been significant issues with environmental pollution derived from energy generation. For instance, the release of CO_2 is unavoidable from the commonly used thermal power plant where fossil fuels are burned for power. The accumulation of CO_2 in the atmosphere has resulted in the greenhouse effects leading to global warming and climate change. Paris Agreement sets the target of curbing the atmosphere temperature increase to be below 1.5 ^{o}C by the end of this century in reference to the pre-industrial era. The recently convened COP28 noted that we have to stop fossil fuels to achieve the goal. Renewable and clean energy have to be adopted for a sustainable solution.[3] Scientists have worked to develop more energy-efficient renewable energy sources, which include solar, wind, hydro, geothermal, and to some extent nuclear energy.[4-6] However, because of the temporal mismatch between generation and demand, such renewable energy sources require energy storage to make them more energy efficient.[7] [8] Among all energy storage techniques, a secondary battery is a potential option with the development of electrochemical technologies. A battery can store electrical energy in the form of chemical energy.[9, 10] The lithium-ion batteries can now have sufficient energy density and redox cycling life with reasonable cost, thanks to Stanley Whittingham who found the lithium intercalation phenomena in layered metal oxides/sulfide (titanium disulfide initially), making such materials as cathode for LIBs.[11] The rechargeable LIBs have dominated the 3C market and found increasing application in electric vehicles (EVs). Intensive research is undergoing worldwide for grid-scale energy storage using this type of device.[12, 13]

1.2 Significance of LIBs

LIBs possess a high capacity because of the small ionic radius and low reduction potential of lithium, the smallest single-charged ion.[14] LIB with a carbon anode can have a voltage as high as 3.6 V. By varying the electrode materials and designs, LIBs can provide chemical potentials in different ranges along with other characteristics such as low self-discharge, high energy densities, and high Coulombic efficiency.[15] LIBs are used in several applications, from small electronic gadgets to massive power supplies for EVs.[13, 16] Different factors must be considered when using such batteries, including energy density, power, cycle life, cost, safety, and environmental impact.[12, 17] Cost, energy density, cycle life, and safety are the determining factors for EVs and grid-energy storage. At the same time, energy density and safety are the most crucial parameters for portable devices. A quick charge-discharge rate should also be desirable for the three applications. [18-20]

The performance of batteries is predominantly influenced by the characteristics and properties of the materials employed in the fabrication of their various constituents, as previously discussed because the inherent chemistry of the materials depends on the properties of the materials used.[21, 22] The state-of-the-art LIBs with an NCM/NCA/LFP cathode and graphite anode typically possess a volumetric energy density of 250-650 Wh L^{-1} and gravimetric energy density of 100-250 Wh L^{-1}.[23, 24] A considerable interest is in raising the energy densities to >1,000 Wh L^{-1} and 500 Wh L^{-1} globally.[25, 26] Since Sony Corporation [27-29] first announced the commercialization of lithium-ion technology in 1991. After that gradual increases in energy density have been achieved as the result of continous advancements in materials, manufacturing techniques, and battery management systems. It allows for improved performance and enhanced capabilities in various electronic devices. The ideal design of materials and battery components can favor the above-discussed parameters and reduce the risk of failure or malfunction, ensuring optimal performance and longevity.[30]

1.3 Components and Working Mechanism of LIBs

A LIB battery has three main components: a cathode, an anode, and a separator with an electrolyte facilitating the ion transfer between the electrodes. The three main components actively participate in the electrochemical process during cell operation. Figure 1.1 shows the schematic representation of the movement of ions in a Li-ion battery having Li_xC_6 as an anode and $Li_{1-x}MO_2$ (M = Mn, Co, and Ni) as a cathode material.

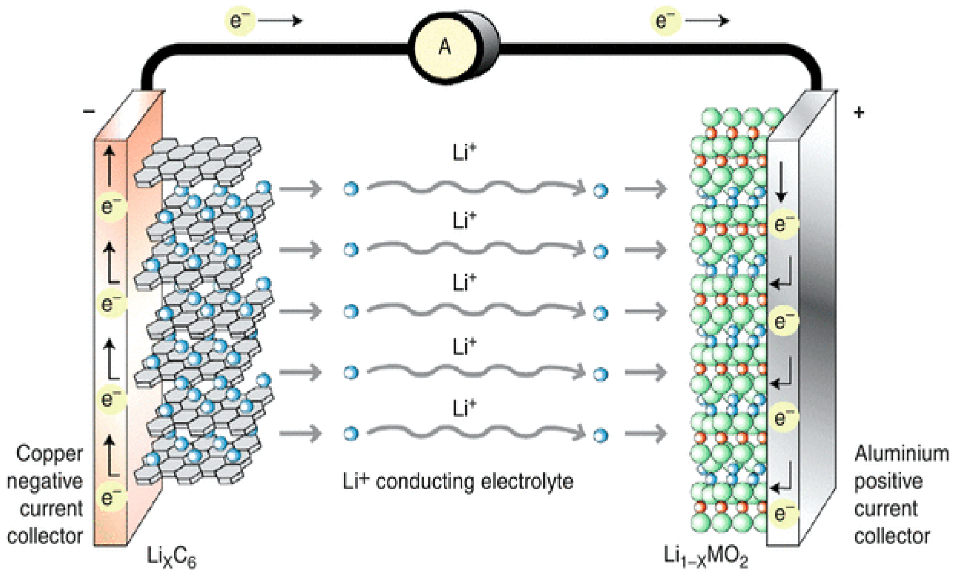

Figure 1.1: Schematic representation of LIBs. Reprinted with permission from Ref.[31] copyright © 2012, Springer.

Lithium migrates into the electrode during intercalation and deintercalation. Intercalation and deintercalation refer to the process of ions being inserted into and removed from the crystal structure of electrode materials respectively, typically in rechargeable batteries like LIB. This process occurs at the electrode-electrolyte interface and is crucial for the functioning of the battery. On the other hand, charging and discharging refer to the overall process of the battery gaining and losing electrical energy, respectively, which involves the flow of electrons through the external circuit. During the charging process, lithium ions are removed from the cathode and incorporated into the anode. While during discharging, lithium ions are taken out of the anode, move through the electrolyte, and become embedded in the cathode. The following are the electrode charging reactions using LCO/graphite as an example. [31]

Cathode (half-cell reaction): $LiCoO_2 \rightarrow Li_{1-x}CoO_2 + xLi^+ + xe^-$ 1.1

Anode (half-cell reaction): $xLi^+ + xe^- + C_6 + \rightarrow Li_xC_6$ 1.2

where x refers to moles of lithium.

Overall cell reaction: $LiCoO_2 + C_6 \rightarrow Li_{1-x}CoO_2 + Li_xC_6$ 1.3

In an electrochemical cell, such as a battery, the cathode is where reduction (gain of electrons) occurs. Electrons flow from the cathode to the external circuit. In contrast, the anode is where oxidation (loss of electrons) occurs. Electrons flow from the external circuit to the anode. The cathode is the positive electrode (where current flows out) and the anode is the negative electrode (where current flows in). The terms “positive electrode” and “negative electrode” are often used interchangeably with cathode and anode, respectively, but it’s essential to understand the underlying redox processes.

Typically, the cathode materials in commercial LIBs are $LiNi_xMn_yCo_{1-x-y}O_2$ (NMC), $LiCoO_2$ (LCO), $LiMn_2O_4$ (LMO), and $LiFePO_4$ (LFP).[30, 32, 33] Graphite is often used as an anode because of its stability and ability to accommodate lithium ions during charging and discharging cycles, contributing significantly to the battery system's overall performance.[34]

1.4 Electrolyte

While the electrode materials and their morphologies determine the energy density and voltage of a lithium-ion battery, the electrolytes influence the energy and power density along with the safety of the battery.[35] Modern battery electrolytes have to meet many requirements, and some of them have to be compromised as a trade-off. The electrolyte must have a high ionic conductivity to reduce the internal resistance of a battery cell. In addition to seeking robust electrochemical stability, there was also a need for the necessary chemical stability. This need stemmed from the challenge of unregulated solid electrolyte interphase (SEI) formation when introducing new materials.[36-38] This implies a reduced sensitivity to the large potential difference between the electrodes during the oxidation and reduction processes. Additionally, the electrolyte must be thermally stable throughout the whole temperature range that a battery operates in. Affordable access to the materials needed to make an appropriate electrolyte will help decrease the cost of producing LIBs.[38]

In current commercial LIBs, the electrolyte is usually made from organic solvent mixed with lithium salts, forming an electrolyte solution that facilitates ion transport between the electrodes in lithium-ion batteries.[39] High ionic conductivity (between 10^{-3} and 10^{-2} S cm^{-1} without a separator and close to 10^{-4} S cm^{-1} with a separator) and wettability on electrode surfaces characterize the liquid organic electrolyte.[40] However, LEs have several drawbacks including high flammability, limited operating temperatures, dendrite formation, and volume change.[41-44] The high flammability of LEs including some organic solvents, such as ethylene carbonate (EC) or diethyl carbonate (DEC) is because of their low flash point (below 30°C).[45-47] When electrodes generate heat during the charge/discharge process, LEs would serve as fuel. The possibility of an explosion increases if the heat dissipation is inadequate from inside to outside of a cell. In addition, organic liquid exhibits an unstable electrochemical property that renders it prone to volatility and potential degradation during electrochemical processes. The ionic liquid-based electrolytes solved the problem of flammability and volatility, but their relatively high viscosity resulted in a low ionic conductivity. Solid-state batteries (SSBs) are becoming increasingly popular in the research field because they promise to offer higher energy densities, longer lifespans, and improved safety due to the absence of flammable liquid electrolytes.[48-50]

1.5 All-Solid-State Electrolytes

ASSEs have evolved as an integral material for secure and energy-rich battery systems.[51] They have high mechanical strengths to suppress Li dendrite growth and show higher thermal and electrochemical stability, thus allowing the utilization of the high-capacity (3860 mAh g^{-1}) lithium metal as the anode. Compared to the graphite anode-based LIBs, the energy density of the lithium metal counterpart can rise by 50%.[26, 52] [53, 54] Generally, there are two different types of ASSEs, including solid polymer electrolytes (SPEs), also known as an organic polymer matrix swelled with lithium salts, and inorganic ceramic electrolytes (ICEs).[55, 56]

1.5.1 Inorganic Ceramic Electrolytes

ICEs are ion conductors with high lithium ionic conductivity and transference numbers at RT.[55] Compared to LEs and SPEs, they are more thermally stable and have low flammability, large electrochemical windows, and basic physical blockage of the lithium dendrite penetration. The silver ionic compound Ag_3SI, the first inorganic solid electrolyte (ISE), was discovered in the 1960s with a 10^{-2} S cm^{-1} ionic conductivity at ambient temperature. Sulfide-group and oxide-group electrolytes are the two commonly used types of inorganic SSEs. The materials in the oxide category include garnet-type (LLZO), perovskite-type (ABX_3), sodium superionic conductor-type (NASICON), and Li superionic conductor (LISICON)-type materials. Whereas in sulfide glasses (GeS_2 + Li_2S + LiI + Ga_2S_3 and La_2S_3), B_2O_3-Li_2O-LiX(X= F, Cl, Br, I) act as promising candidates for solid-state electrolytes due to their high lithium-ion conductivity and favorable electrochemical properties.[57]

1.5.1.1 Oxides

Thangadurai et al.[58] initially described an oxides family of fast conductive Li-ion called $Li_5La_3M_2O_{12}$ (M = Ta, Nb) with garnet structures in 2003. They show high lithium ionic conductivity and voltage (6V vs. Li^+/Li). A_3B_2 $(XO_4)_3$ is the general form of garnet-type oxides, where A is any of the following: Ca, Mg, La; B is any of the following: Al, Fe, Ni, Ge, Mn, V, Ga, and X is any of the following: Si, Ge, Al.[59] Lithium lanthanum zirconate ($Li_7La_3Zr_2O_{12}$, LLZO) is a frequently used oxide group electrolyte. It shows a large electrochemical operational window (6 V vs. Li^+/Li) and low electrical conductivity (10^{-8} S cm^{-1}) at RT, which makes it the most favorable garnet-type SSE. By using X-ray structure analysis on a single-crystal, Awaka et al.[60] identified the precise cubic (c-LLZO) and a tetragonal (t-LLZO) crystal structure of garnet material (LLZO) (Figure 1.2). A loop made by the Li1 and Li2 sites serves as the Li-ion migration pathway's fundamental building block. Ionic conductivity values for c-LLTO and t-LLTO at RT are 10^{-4} and 10^{-6} S cm^{-1}, respectively.

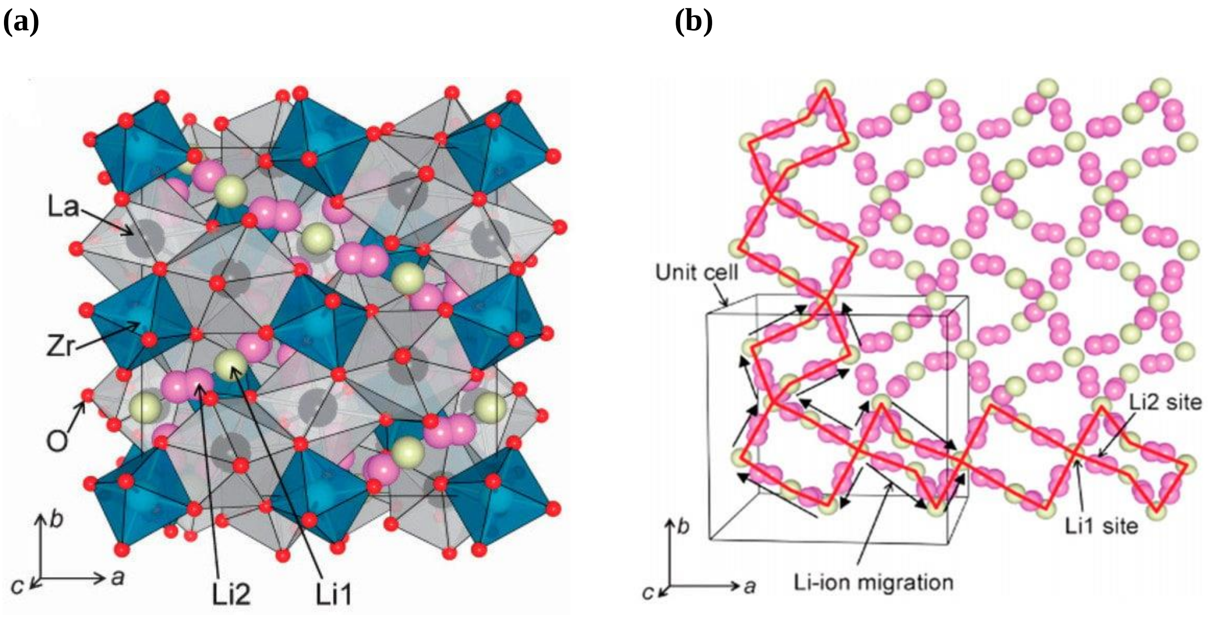

Figure 1.2: (a) Crystal structure of cubic LLZO, (b) Li conducting network in cubic LLZO. Reprinted with permission from Ref. [60] copyright © 2011, Chemistry Letters.

Such electrolytes exhibit high ionic conductivity and broad electrochemical windows, but they become unstable at room temperature while going through the Li^+/H^+ exchange in the presence of moisture to form an insulating Li_2CO_3 coating layer. Hence, their ionic conductivity decreases.[61] Another high Li ion-conducting crystalline inorganic solid electrolyte is perovskites. The general formula for perovskites is (ABO_3)-type where A = Li, La in 12-fold coordination and B = Ti are in 6-fold coordination. The crystal structure of tetragonal LLTO is shown in Figure 1.3. It has also become a good choice for SSEs because of its extraordinary thermal stability and low electric conductivity. However, certain restrictions also exist. First, ionic conductivity significantly decreases and becomes less than 10^{-5} S cm^{-1} at RT at grain boundaries. Primarily, the presence of grain boundaries causes a significant decrease in ionic conductivity, with values dropping below 10^{-5} Scm^{-1} at 298 K. Additionally, direct exposure to metallic lithium or graphite anodes triggers the reduction of Ti^{4+} to Ti^{3+} in crystalline LLTO, elevating its electronic conductivity.[62]

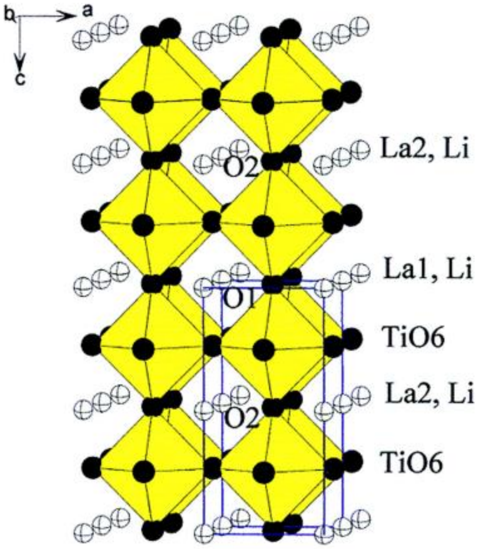

Figure 1.3: Crystal structure of cubic LLTO. Reprinted with permission from Ref. [63] copyright © 2014, Frontiers in Energy Research.

Another Li-rich superionic conductor is anti-perovskites having the general formula ABX_3, where (A = Cl, Br, I; B = O_2; X = Li^+).[64] Crystalline phosphates $Li_{1+x}Al_xTi_{2x}(PO_4)_3$ (LATP) and $Li_{1+x}Al_xGe_{2x}(PO_4)_3$ (LAGP) with NASICON-type structures are widely used oxides, because of their superior conductivity of Li-ion with a value approaching 0.7 mS cm^{-1} at RTs, and a large electrochemical window of 6 V. Commercialised LATP can deliver an ionic conductivity of up to 1.3 mS cm^{-1} at RT.[65] However, they are also unstable with Li-metal anodes.

1.5.1.2 Sulfides

The sulfide and phosphate groups are effective ionic conductors with the highest ionic conductivity of 10^{-4} S cm^{-1} at RT. The first and most popular sulfide glass electrolytes are Li_2S-P_2S_5, Li_2S-GeS_2, Li_2S-B_2S_3, and Li_2S-SiS_2.[66] The crystalline structure of thio-LISICON resembles that of Li_3PO_4 and has an orthorhombic unit cell with tetrahedrally coordinated cations.[67] Such materials can have an increased ionic conductivity of up to 2-3 orders of magnitude at RT. The reported value of high ionic conductivity of $Li_{3+x}(P_{1x}Si_x)S_4$ is 0.6 mS cm^{-1} at RT.[68] Compared to LISICON materials, thio-LISICON electrolytes often exhibit better conductivity and lower activation energy, because sulfides have larger ionic transport channels present. Kamaya et al.[69] has recently reported 1.2×10^{-2} S cm^{-1} ionic conductivity at RT for LGPS-type material. Such material has a novel three-dimensional (3D) framework structure, which is responsible for higher ionic conductivity than those reported for organic liquid electrolytes.

Figure 1.4 shows the one-dimensional (1D) chains of $(Ge_{0.5}P_{0.5})$ S_4 tetrahedra and LiS_6 octahedra joined by a shared edge making the framework structure of the LGPS. These chains share a corner with the PS_4 tetrahedra.[69] Such materials also have several benefits for battery manufacturing, electrochemical characteristics, and safety. Although computational investigations revealed a vast potential window (4.0 V vs. Li^+/Li) for LGPS, such material becomes unstable at low voltage when it comes in contact with Li-metal in the reduction process. Also, LGPS breakdown with Li extraction was possible at high voltage.[70] Sulfide-type SSEs are extremely sensitive when exposed to moisture, which causes hydrogen sulfide to form and severely restricts their commercial uses.

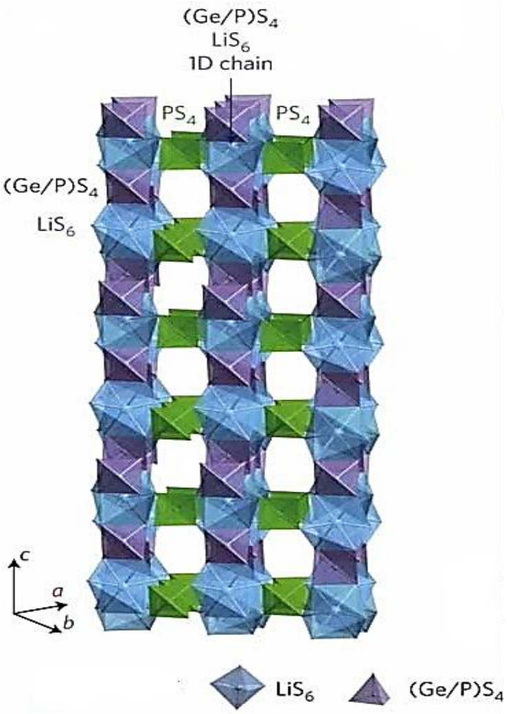

Figure 1.4: Crystal structure of cubic LGPS. Reprinted with permission from Ref.[69] copyright © 2011, Nature Materials.

1.5.1.3 Mechanism of Lithium-Ion Transport

ICEs are also called superionic conductors since they exhibit a high intrinsic bulk ionic conductivity. Defect sites facilitate the transport of Li-ion in crystalline inorganic materials. The main parameters affecting ionic diffusion are the concentration ratio and placements of such defect sites. Such defects result in a low activation energy and hop of numerous ions simultaneously rather than just one (Figure 1.5). [71] Also, ions can hop more easily across lattices because of the extreme disorder of the sublattice. Lithium-ion transportation mechanisms can be categorized into different types, including vacancy diffusion mechanism, direct interstitial mechanism, interstitial mechanism, and direct exchange and ring mechanism (Figure 1.6). [71] In the direct interstitial mechanism, the diffusion of lithium ions is governed by the free spaces in between molecules. The free spaces between molecules should be larger than the radius of the lithium-ion.

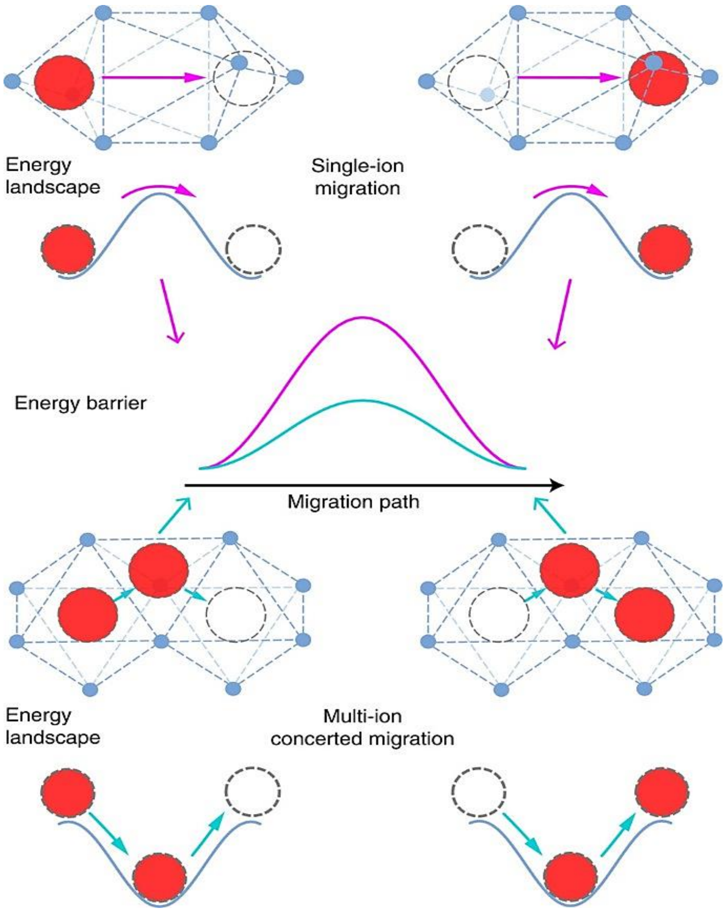

Figure 1.5. Illustration of the strong ion interactions resulting in a decreased energy barrier. Reprinted with permission from Ref.[71] copyright © 2017, Nature Communications.

The term "vacancy mechanism" describes how ions are transported by hopping to the next available vacancy. Ion transit can continue along this cycle since the moved ions will cause new openings in the initial place. Since vacancies are necessary for lithium ion transport, various strategies such as doping with various valence ions have been applied to boost the vacancy ratio and increase the ionic conductivity.

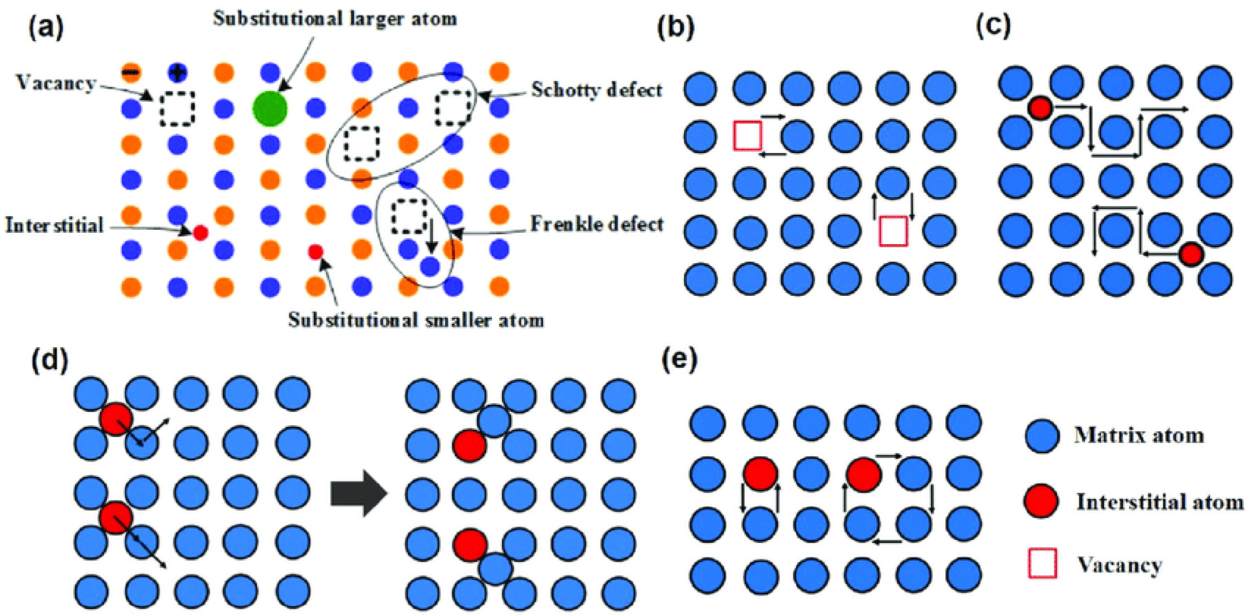

Figure 1.6: Lithium-ion transportation mechanisms in the inorganic region (a) types of point defects in ICSSE, (b) Vacancy diffusion mechanism, (c) direct interstitial mechanism, (d) interstitial mechanism, and (e) direct exchange and ring mechanism. Reprinted with permission from Ref.[72] copyright © 2020, Chemical Society Reviews.

However, in actual situations, the lithium ions transport mechanism may be more complex, including numerous ions ready to diffuse or to combine several methods of diffusion, e.g., the interstitial substitutional exchange mechanism.

1.5.2 Solid Polymer Electrolytes

SPEs are flexible, simple to make, and have strong electrolyte-to-electrode interfacial contact. Li-ion conduction is achieved by solvating different lithium salts ($LiClO_4$, $LiPF_6$, $Li[N(SO_2CF_3)_2]$, etc.) in the polymer matrix to form a heterogeneous system because of the imbalance ratio of polymer and ionic salt mixture. SPEs can be considered polymer-rich or polymer-poor depending upon the concentration of salts added to the polymer matrix. Differnet types of polymer matrix includes PEO,[73-76] PAN poly(acrylonitrile),[77, 78] PMMA poly(methyl methacrylate),[79] PVDF poly(vinylidene fluoride),[80, 81] etc. (Figure 1.7). Gel polymer electrolytes (GPEs) and SPEs are two categories into which polymer-based SSEs can be divided, based on the facts that LEs are involved or not.[80, 82] In GPEs, a small quantity of liquid is employed in the polymer to improve the adaptability, interfacial contact, and ionic conductivity. GPEs are widely used because their ionic conductivity may reach that of LEs. However, liquid in GPEs may raise safety issues when used with metallic Li anodes. SPEs are desirable alternatives to LEs because they are nonvolatile and noncombustible, have low density, are flexible, and have strong processing performance. Compared to ISEs, SPEs provide greater advantages in processability, flexibility, interfacial contact, lightweight, and affordability. Whereas, poor mechanical strength and less ionic conductivity are some drawbacks of SPEs.[83]

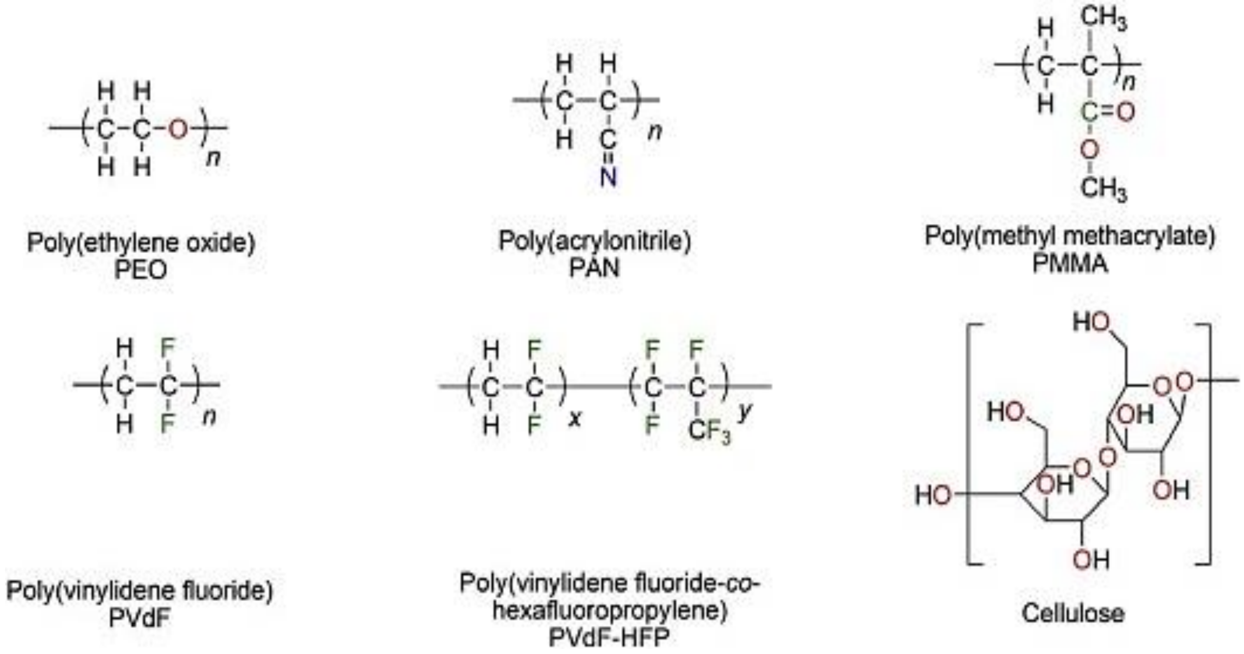

Figure 1.7: Chemical structures of polymer matrices used in solid-state electrolytes. Reprinted with permission from Ref.[84] copyright © 2017, Journal of The Electrochemical Society.

PEO with continuous oxygen vinyl group (CH_2CH_2O) are emerging as the best candidates to be employed in SPEs because of their ion transport capabilities and direct connections to the alkaline salt. Because of its resistance to clumping and diffuse charge distribution, LiTFSI remains the best choice to be added to PEO electrolytes compared to other salts ($LiClO_4$, $LiPF_6$, $LiBF_4$, and $LiSO_3CF_3$ (LiTF).[75] The usual coordination number of an individual Li-ion in PEO is 4-5 oxygen atoms. A distance of 0.255 nm typically separates the Li-ion and these oxygen atoms. Generally, lithium ions and their counterions are both moveable, making the system a dual-ion conductor. There is a strong coordination of Li-ion with the ether oxygen of PEO, which makes the Li-ion less mobile than the counterions. In the polymer matrix, Li-ions connect with oxygen at Lewis basic sites and hop between oxygen groups of the same chain (intrachain diffusion), different chains (interchain diffusion), or shifts. Such frequent interchain diffusion increases Li-ion conductivity.[85] One can infer from the mechanism that the conductivity will depend on how easily Li-ions can separate from the polymer chain. A further significant element that affects ion conductivity is the mobility of the polymer chain. Polymers having low molecular weight and higher amorphous regions exhibit a greater conductivity; however, in most cases, the ionic conductivity is less than 0.1 mS cm^{-1} at RT.[53]

1.5.2.1 Mechanism of Lithium-Ion Transport

PEO and the complex lithium salts make up the majority of the SPEs. The coordination between Li-ion and ether oxygen drives the Li-ion. During PEO chain segmental movement, Li-ion may continue to oscillate by coordinating with the oxygen on the same chain at one moment or a different chain at the next moment (Figure 1.8a). Repeating this procedure allows the lithium ions to move through the polymer electrolytes above the glass transition temperature (T_g) in an amorphous phase.[83] Figure 1.8b shows the movement of Li-ion in crystalline PEO_6-$LiAsF_6$. Li-ions move through the cylindrical tunnels created by pairs of PEO chains, which are folded together due to their interaction with Li-ions. Li-ion migration only occurs along the cylindrical tunnels. Thus, no segmental motion of the polymer chains happens in the crystalline phase of polymer electrolytes.[86]

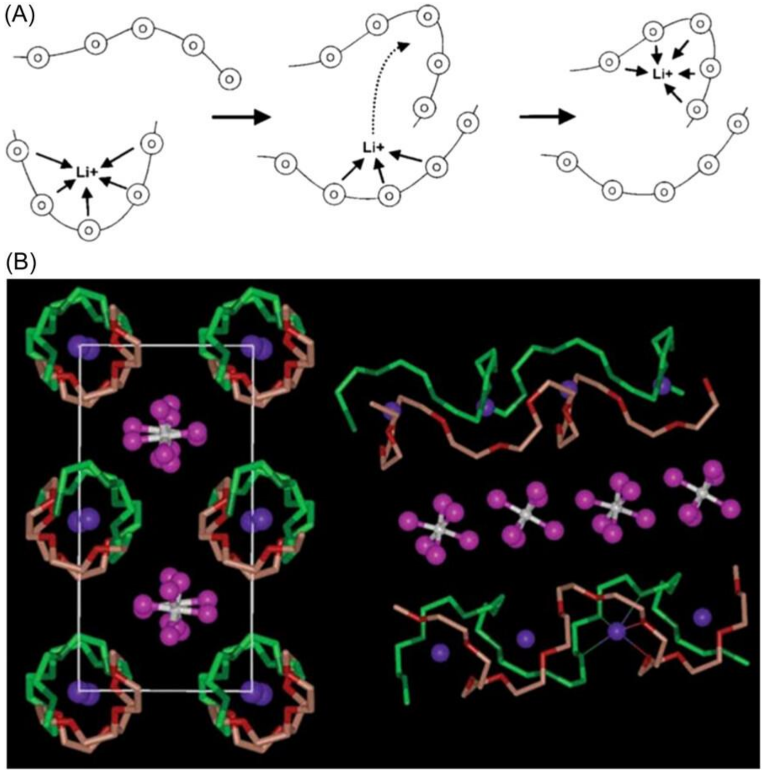

Figure 1.8: Schematic representation of (a) Li-ion transport in the amorphous phase, and (b) in the crystalline phase. Reprinted with permission from Ref.[86] copyright © 2005, Journal of the American Chemical Society.

PEO is known for its ability to form stable solid complexes as a host polymer compared to other solvating polymers. Despite this advantage, solid-state LIBs based on SPEs still provide low RT ionic conductivity and a suboptimal Li anode/SPE interphase, which results in the batteries falling short of the required theoretical specifications. Figure 1.9 shows the ionic conductivities of different SSEs as a function of temperature.

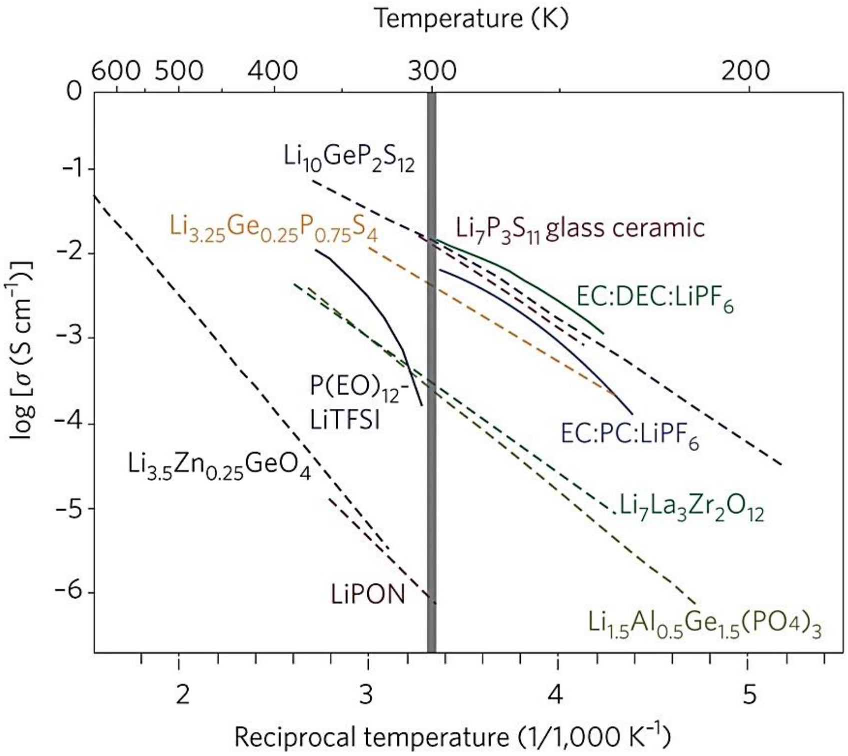

Figure 1.9: Ionic conductivities of various SSEs. Reprinted with permission from Ref.[87] copyright © 1994, Journal of Power Sources.

The crystallinity of SPEs significantly impacts the ionic conductivity of PEO. At temperatures lower than the T_g, crystalline phases are more prevalent in PEO, which slows down Li-ion movement and results in small ionic conductivity of 10^{-7} S cm^{-1}, which is insufficient for most practical applications.[88]

1.5.3 Composite Solid-State Electrolytes

CSSEs are a combination of SPEs and ICEs. Such electrolytes can be categorized into ceramic in polymer or polymer in ceramics, depending on the amount of ceramic filler supplied to the polymer. In most CSSE systems, the oxygen atom of polymer (e.g., PEO) tends to share its lone pair of electrons classified as a Lewis base, whereas the filler accepts that pair of electrons and is named as Lewis acid. The advantages of both SPEs and ICEs are combined in one frame. Therefore, CSSEs are more adaptable, stable, and interfacially compatible with the Li metal anode. Additionally, CSSEs have higher ionic conductivity and improved processability compared to SPEs.[57, 83] Inorganic fillers can be passive or active, as described in the subsections below.

1.5.3.1 Passive Fillers

In a CSSE system with passive filler, there is no conduction of Li-ion through such fillers, e.g., TiO_2, SiO_2, Al_2O_3, and ZrO_2, because the ceramic particles are not ion conductive. In composite electrolytes containing PEO and passive filler, Li-ion conduction happens in one of two ways shown in Figure 1.10. Path 1 involves segmental mobility of PEO molecular chains via the PEO, while Path 2 involves PEO/passive filler interactions. Since fillers can significantly increase the ionic conductivity of SPEs, path 2 is the primary cause of enhancing Li-ion diffusion. Capuano et al.[89] discovered in 1991 that inorganic fillers increase the ionic conductivity, stability, and mechanical strength of SSEs. Kumar and Scanlon[87] proposed that connecting surfaces of polymer and ceramic serve as the fastest routes for Li-ion transport and increase conductivity. Depending on their particle size, surface type, and concentration of such fillers in the CSSEs, such fillers affect the overall ionic conductivity of electrolytes differently. Ceramic particles also can increase amorphous regions by reducing PEO's crystallinity, which is another factor responsible for increasing ionic conductivity.[87]

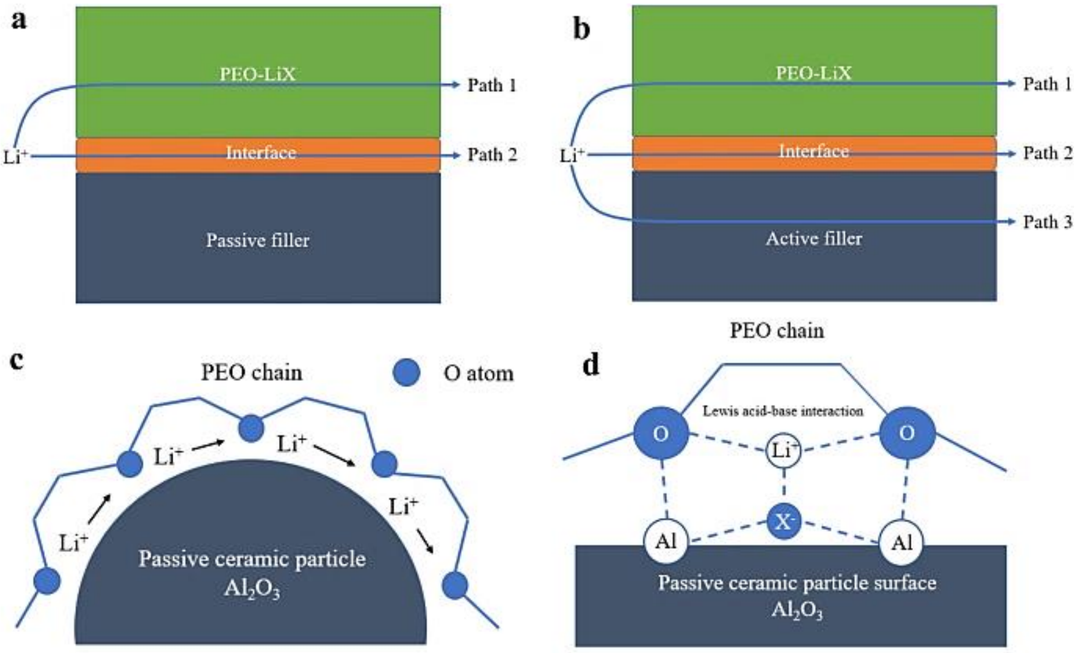

Figure 1.10: Possible transport channels of Li-ion in (a) PEO-passive fillers composite, (b) PEO-active fillers composite, (c) Effect of passive fillers distorting the regularity of PEO chains, (d) Lewis acid-base interactions between PEO and passive ceramics. Reprinted with permission from Ref.[90] copyright © 2021, Nano Convergence.

The filler functions also as the cross-linker of the polymer. As a result, PEO would have more amorphous structures, and the recrystallization process would be suppressed.[91] Tan et al.[92] studied PMMA/ LiTFSI SPEs containing SiO_2 and Al_2O_3 as passive fillers. Al_2O_3 increased the ionic conductivity from a low 1.36×10^{-5} S cm^{-1} to a high value of 2.05×10^{-4} S cm^{-1}. This may be attributable to the OH surface nature of alumina, which gave the oxygen atom in PMMA more coordination sites for the conduction of ions. Croce et al.[93] further support the findings that the acidic surface nature of alumina increased the conductivity of SPE. Contrarily, no interaction was found between the basic Al_2O_3 surface and salt anion or polymer, which ultimately affects the conductivity, resulting in a low 7.3×10^{-6} S cm^{-1} ionic conductivity at 30 °C. In addition to size, the morphology of the ceramic filler also affects the performance of CSSEs. With increased performance in lithium batteries, the 3D-structured SiO_2 nanofibers CSSEs showed greater mechanical strength and flexibility.

1.5.3.2 Active Fillers

Active fillers are the ones that contain lithium ions. $Li_7La_3Zr_2O_{12}$ (LLZO), Li_3N, $Li_{1+x}Al_xTi_{2-x}(PO_4)_3$ (LATP), $Li_{3x}La_{2/3x}TiO_3$ (LLTO), $Li_{1+x}Al_xGe_{2-x}(PO_4)_3$ (LAGP) and $LiAlO_2$ are some examples of materials that are frequently utilized as active fillers in CSSEs.[90] $Li_7La_3Zr_2O_{12}$ (LLZO) has a structure like garnet. It is the most stable towards lithium metal among the inorganic active fillers and is preferred because of its large electrochemical window (>5 V vs. Li^+/Li).[94] Keller et al. developed a CSSE by adding LLZO in PEO/LiTFSI SPE, showing an improved interfacial contact of an electrolyte with the electrode and higher electrochemical performance.[95] Cha et al. [96] added LLZO inorganic filler and PEG/DME plasticizer in PEO-LiTFSI SPEs and improved the electrochemical performance of CSSE alongside increased lithium ionic conductivity and transference number. However, LLZO is unstable at ambient temperature, making it reactive to moisture.[95]

Introducing LLZTO in SPEs is another strategy to improve ionic conductivity and Li-ion transference number. The corresponding values of high Li-ion conductivity and transference number after adding LLZTO in PPC/LiTFSI are 0.520 mS cm^{-1} at 20 °C and 0.75, respectively.[97] Similarly, another inorganic material that can be utilized as a nano-filler in SPEs is LAGP. It is also inert towards lithium metal electrodes like LLZO.[98] W. Liu et al.[99] demonstrated that adding random conductive nanowires (NWs) increases the composite electrolyte's ionic conductivity more than adding nanoparticles. The improved ionic conductivity value is 6.05×10^{-5} S cm^{-1} at 30 °C.

The schematic representation of regions that act as a pathway for conducting Li-ions on the surfaces of inorganic nanoparticles (NPs) and NWs (Figure 1.11). The authors also demonstrated that ionic conductivity can be enhanced more if NWs are added in a well-aligned arrangement typical to the direction of electrodes in polymer electrolytes rather than added randomly.

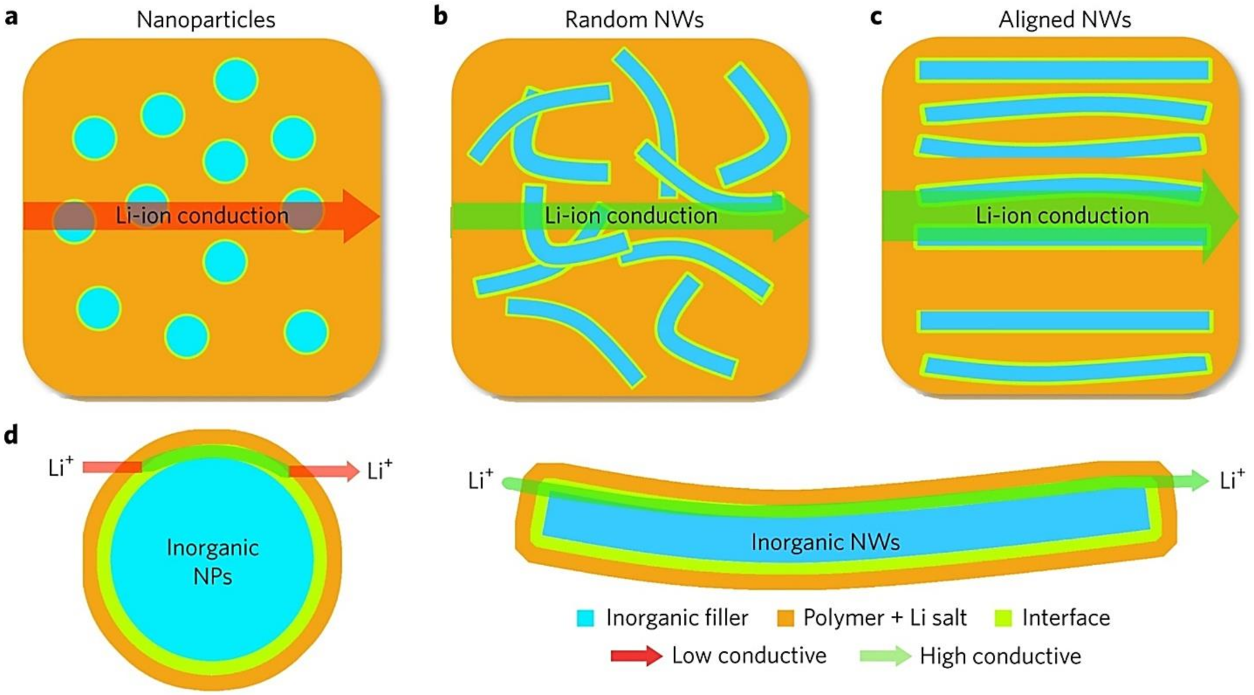

Figure 1.11: Li-ion transport channels in CSSEs (a) NPs, (b) random NWs, (c) aligned NWs, and (d) the surfaces of NPs and NWs. Reprinted with permission from Ref.[100]copyright © 2017, Nature energy.

Because aligned NWs in composite electrolytes may offer more continuous rapid transport channels for ions and electrons, leading to enhanced conductivity and improved overall performance of the electrolyte (Figure 1.11c). In general, ICEs exhibit greater ionic conductivity than other types of SSEs, with some even being similar to LEs. However, the use of inorganic-based electrolytes is severely hindered by the fragile nature of solid particles and high interface resistance at the electrolyte/electrode surfaces. Recent studies have shown that lithium dendrites can develop along grain boundaries and finally penetrate the ICEs, causing electrode contact.[101] Such challenges must be overcome to use inorganic electrolytes in large-scale commercial production.

1.6 Challenges to SPEs for LIBs and Motivation

The development of ideal SSE materials satisfying all the requirements still needs a long way to develop. SSE development is paying close attention to SPEs because a flexible polymer matrix shows good processability and interfacial wettability. Particularly, PEO-based electrolytes transport lithium ions using the segmental motion of polymers.[74] However, in crystalline PEO, Li-ions are found inside cylindrical tunnels formed by folded PEO chains that are ether oxygen-coordinated. Thus, no segmental motion of the polymer chains is present within the cylindrical tunnels. Li-ion migration only occurs along the cylindrical tunnels resulting in low conductivity at ambient temperature. Due to the crystal structure of the PEO matrix, the poor RT ionic conductivity of 10^{-8}-10^{-7} S cm^{-1} of PEO/LiTFSI is a significant drawback of such SPEs.[102] Optimizing the ionic conductivity in solid polymer electrolytes directly impacts the efficiency, safety, and commercial viability of lithium-ion batteries, making them more suitable for widespread real-world applications across various industries.[103]

The major issue of poor RT ionic conductivity and Li-ion transference number of SPEs can be handled by modifying the polymer host or adding some inorganic fillers or plasticizers to a polymer.[104] Polymer hosts can be modified by copolymerization, grafting, crosslinking, and blending with a second polymer to boost salt dissociation and inhibit recrystallization. Whereas, the inorganic fillers, including passive oxides (SiO_2, TiO_2, Al_2O_3, and ZrO_2), active oxides (perovskite, NASICON, and garnets), sulfides (LGPS and LSPS), and metal-organic framework (MOFs) can be added to SPEs to increase Li-ion transport pathways. Also, different types of plasticizers, including liquid such as ethylene carbonates (EC), polyethylene glycol (PEG), diethyl carbonate (DEC), dimethyl carbonate (DMC), glycerol and solid plasticizers including succionitrile (SN) can be added to solid polymers to increase lithium salts dissociation and decrease glass transition temperature to increase Li-ionic conductivity and transference number.[104, 105] Hence, polymer blending or adding a plasticizer in SPE is a simple, reasonable, and an efficient way to increase ionic conductivity.[104, 106, 107]

1.7 Research Objectives

Li-ion batteries built on SSEs are a new type of energy storage system. SPEs low room temperature ionic conductivity has to be improved. There are different techniques available, such as modifying the polymer host and adding a plasticizer in modified solid polymer electrolytes. Creating new materials or changing the properties of existing materials is frequently labor and time-intensive, and it depends heavily on human intuition. Research and development (R&D) of new solid electrolyte materials can be considerably accelerated by using computational methods to forecast the properties of novel materials. Thus, desired qualities of materials can be developed by rational design methodologies based on numerical simulation. Additionally, it might be challenging to properly characterize the intricate atomistic mechanisms of ion transport and dynamics in experiments. Computational modeling can supplement experimental investigations by offering a special perspective on the underlying mechanisms taking place in electrolytes of solid-state LIBs. [108]

This study aims to comprehensively explore the dynamic behaviors of Li-ions in PBSPEs under different operating conditions. For achieving high ionic conductivities (~10^{-5} and higher) of PBSPE, the research objectives of this study include:

- to develop a generalized model of PBSPEs with the ability to predict lithium ionic conductivity and transference number.
- to reveal the effects of varying salt concentration, polymer blending ratio, plasticizer concentration, and operating temperatures on the dynamic properties of ions through CMD simulations using PEO/PVDF/SN/LiTFSI PBSPE as a case study.

Chapter 2. Literature Review

2.1 Computational Technique to Study Electrolyte Systems

Computational techniques play a pivotal role in understanding and analyzing electrolyte systems, providing valuable insights into their behavior and properties at the molecular level. Due to the rapid evolution of computer technologies, various tools, theoretical algorithms, and simulating codes including CMD, ab initio molecular dynamics (AIMD), density functional theory (DFT), and Monte Carlo simulation (MCS), have been devised.[108] By employing these computational techniques, researchers can explore various aspects of electrolyte systems, including ion transport mechanisms, solvation behavior, interface stability, and the impact of electrolyte composition on battery performance. These simulations aid in the design and optimization of electrolyte materials, contributing significantly to the advancement of energy storage technologies like lithium-ion batteries.[109]

2.1.1 Classical Molecular Dynamics

CMD simulations are frequently employed in computational materials science to determine a molecular-level understanding of the properties of ions in electrolytes. Simple electrolyte systems can be simulated using the time-dependent Schrödinger equation. The state functions of quantum-mechanical systems are described by the time-dependent Schrödinger equation, which explains how systems change over time. The system's dynamic evolution may be seen with this technique, which allows atoms and molecules to interact for a specified duration. The trajectories of atoms and molecules can be calculated by quantitatively solving Newtonian equations of motion at predetermined time steps. The forces between the particles and their potential energy are calculated using interatomic potentials or molecular mechanics force fields.[110]

CMD has been used to show different mechanisms in which the Li-ion diffusion coefficient contributed to the movement of the polymer matrix. In PEO electrolytes, Muller-Plathe[111] investigated the transit of Li-ion and I-ion and their clustering characteristics. Neyertz and Brown investigated the local structure and kinetics of Na-ion and I-ion in PEO electrolytes.[112] These preliminary MD simulations illuminate PEO's structure and ion transport processes. Borodin and Smith's many-body polarizable force fields for polyelectrolyte systems with different anions later provided fundamental insight into the many mechanisms impacting Li-ion transport MD simulations and investigated the ion transport in polymer nanocomposites comprising TiO_2 nanoparticles within a PEO polymer electrolyte. Their findings indicated that the inclusion of nanoparticles reduced cationic mobilities compared to the pristine PEO matrix.[113]

2.1.2 Basic Working Principles of CMD Simulations

Structural information and dynamic properties of electrolyte systems can be extracted by resolving the total energy (E_{total}) for all the particles in the system using molecular models in MD simulation. The governing equation can be described as follows:

$$E_{total} = E_{kin} + E_{pot} \tag{2.1}$$

The potential energy E_{pot} accounts for the interactions between particles in the system and is usually calculated using a force field or potential energy function that describes the interactions between atoms or molecules. This potential energy function typically includes terms for bonded interactions and non-bonded interactions.

$$E_{pot} = E_{bonded} + E_{nonbonded} \tag{2.2}$$

The bonded energy E_{bonded} is often decomposed into three main components: the bond energy (E_{bond}), the angle energy (E_{angle}), and the dihedral energy ($E_{dihedrals}$). These components represent the energetic contributions associated with different types of bonded interactions between atoms or molecules within the system.

Bond Energy (E_{bond}):

This term accounts for the energy associated with covalent bonds between atoms. It typically includes contributions from bond stretching, where the bond length deviates from its equilibrium value according to a potential energy function describing bond stretching interactions.

Angle Energy (E_{angle}):

The angle energy represents the energy associated with bond angles formed by sets of three atoms. This energy arises from deviations of bond angles from their equilibrium values, and it is described by a potential energy function that accounts for angle-bending interactions.

Dihedral Energy ($E_{dihedrals}$):

The dihedral energy captures the energetic contributions arising from torsional rotations around chemical bonds. It accounts for the energy changes associated with the relative orientations of bonded atoms or groups of atoms, often described by a potential energy function that considers dihedral angle rotations.

Hence, the total bonded energy $E_{bonded}$is the sum of these three contributions:

$$E_{bonded} = E_{bond} + E_{angle} + E_{dihedrals} \tag{2.3}$$

In molecular dynamics simulations, particularly when dealing with complex molecular systems, it's common to include another term known as improper energy ($E_{improper}$). The improper energy accounts for the energy associated with improper torsions or out-of-plane deformations, which are important for maintaining the proper geometrical arrangement of molecular structures. The improper energy term, $E_{improper}$, typically arises when dealing with molecules containing certain functional groups or ring structures, where it's necessary to ensure that specific atoms maintain a particular spatial orientation relative to each other. For example, in a ring structure, it's important to maintain the planarity of the ring, and improper torsions help to enforce this planarity. So, the total bonded energy, E_{total} , including the improper energy term, is given by:

$$E_{bonded} = E_{bond} + E_{angle} + E_{dihedrals} + E_{improper} \tag{2.4}$$

This equation encompasses all the major contributions from bonded interactions in the system and is crucial for accurately modeling the behavior of molecular systems in molecular dynamics simulations.

In molecular dynamics simulations, the non-bonded energy ($E_{non-bonded}$) typically includes two main components: the van der Waals energy (E_{vdW}) and the electrostatic energy (E_{es}). These components represent the energetic contributions associated with non-bonded interactions between atoms or molecules within the system.

Van der Waals Energy (E_{vdW}):

This term accounts for the attractive and repulsive forces between atoms or molecules due to van der Waals interactions. Van der Waals forces arise from fluctuations in electron distributions, resulting in temporary dipoles and induced dipole-induced dipole interactions. The van der Waals energy is typically described by a potential energy function that includes terms for attractive (dispersion) and repulsive (steric) interactions.

Electrostatic Energy (E_{es}):

The electrostatic energy represents the energy associated with electrostatic interactions between charged particles, such as ions or polar molecules. These interactions arise from the Coulombic attraction or repulsion between charged particles. The electrostatic energy is described by Coulomb's law and includes terms for both short-range (ionic) and long-range (dipole-dipole) interactions. The total non-bonded energy ($E_{nonbonded}$) is the sum of these two contributions:

$$E_{nonbonded} = E_{vdW} + E_{es} \tag{2.5}$$

The kinetic energy E_{kin} accounts for the motion of particles in the system and is determined by their velocities. In CMD simulations, the kinetic energy is often calculated using the velocities of particles according to their masses and speeds:

$$E_{kin} = \frac{1}{2} m_i v_i^2 \tag{2.6}$$

Where m_i is the mass of particle i and v_i is its velocity.

By analyzing the total energy E_{total} and its components during MD simulations, the valuable information about the structure, dynamics, and thermodynamic properties of electrolyte systems, such as solvation structures, diffusion coefficients, and phase behavior can be extracted.

The chemical classes employed to establish the parameters are subject to a certain force field. All-atom force fields can explain the properties of a system's atoms, whereas united-atom force fields treat groups of atoms as particles. For organic compounds, force fields parameterized using experimental data or from calculations based on ab-initio quantum mechanics contain all the details of each atom’s bond order and hybridization, listed by particular atom types. A schematic representation of the MD simulation procedure is shown in Figure 2.1.

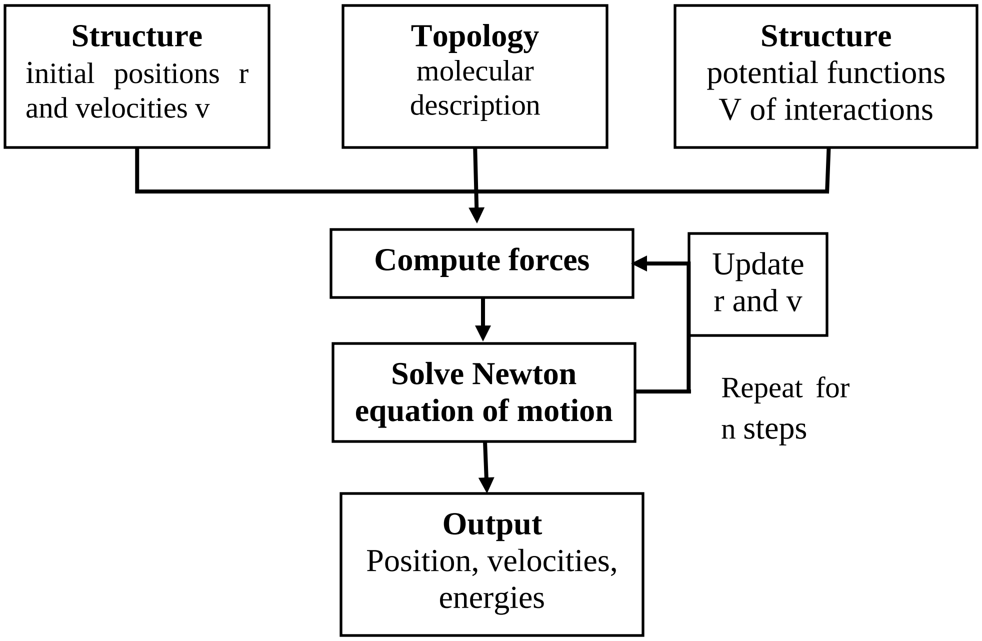

Figure 2.1: Schematic representation of MD simulation procedure.

OPLS-AA,[114] OPLS-UA,[115] COMPASS,[116] DREIDING,[117] and CHARMM[118] are a few examples of frequently utilized force fields. Additional force fields have recently been considered for modeling more intricate and sophisticated amorphous linear and branched PEO. Many simulation programmes, including CHARMM,[119] GROMOS,[120] AMBER,[121] and GROMACS,[122] can be used to perform CMD simulations for SSE systems.

2.2 PEO-based SPEs

SPEs have been extensively investigated as SSEs ever since Wright et al. discovered in 1973 that the combination of PEO and alkali metal salt resulted in an ion conductive complex. Since then, SPEs have been observed to accumulate traditional lithium salts, e.g., $LiClO_4$, $LiPF_6$, $Li[N(SO_2CF_3)_2]$. A typical lithium salt used in PEO-based SPEs is LiTFSI, which has high chemical stability. Lithium salts can be separated by the ether coordination sites present in the

PEO chain. Most LiTFSI in PEO matrices is dissociated.[123] However, the degree of anion aggregation increases with temperature and salt content. The macromolecular chain flexibility of PEO aids in Li-ion transfer. Li-ions traveling alongside PEO chains often exhibit higher diffusion than the Li-ions that hop in between two or more PEO chains, as explained by Borodin et al.[113] In PEO-based SPEs, the length of polymer chains affects their segmental motion, and as a result, decides the diffusion of ions. Longer chains have more robust mechanical stability and lower segmental motion. In comparison, shorter chains are often more adaptable and allow ions to diffuse more along PEO chains resulting in higher diffusion coefficients. However, the application of PEO/LiTFSI electrolytes is still hindered by their poor ionic conductivity at ambient temperature.[123] Researchers presented different techniques to prepare modified ASSPEs for real-life applications in LIBs. Some of them will be explained in the subsequent sections.

2.3 Methods to Improve Ionic-Conductivity of SPEs

2.3.1 Adding Two or More Salts in SPEs

An effective way to enhance the ionic conductivity of SPEs is to incorporate two or more salts into a single polymer matrix. When two or more salts are combined in proper ratios keeping the total weight the same as that of a single salt, desirable results can be attained. In a mixed salt electrolyte system, more free ions are available for conduction as compared to an electrolyte containing a single salt, and the chance of ion aggregation will be lower in the former situation. Additionally, a decrease in T_g and crystallinity of the polymer is seen in an electrolyte with more than one salt.[124] Tao and Fujinami explained the increase of ionic conductivity of up to 5×10^{-5} S cm^{-1} at 30 °C when lithium aluminate and lithium borate salts were mixed in PEO-based SPEs.[125] Zhao et al. have investigated the effects of primary, secondary, and tertiary salts in PEO/halloysite nano clay (HNC) composites. They reported a slight increase in room temperature ionic conductivity (~5.62 × 10^{-5} S cm^{-1}) when a second salt lithium bis(oxalate)borate (LiBOB) was added to PEO-LiTFSI-HNC SPEs. Figure 2.2 shows the lithium ionic conductivity regulation by utilizing more than one salt in the prepared SPE. [126]

s

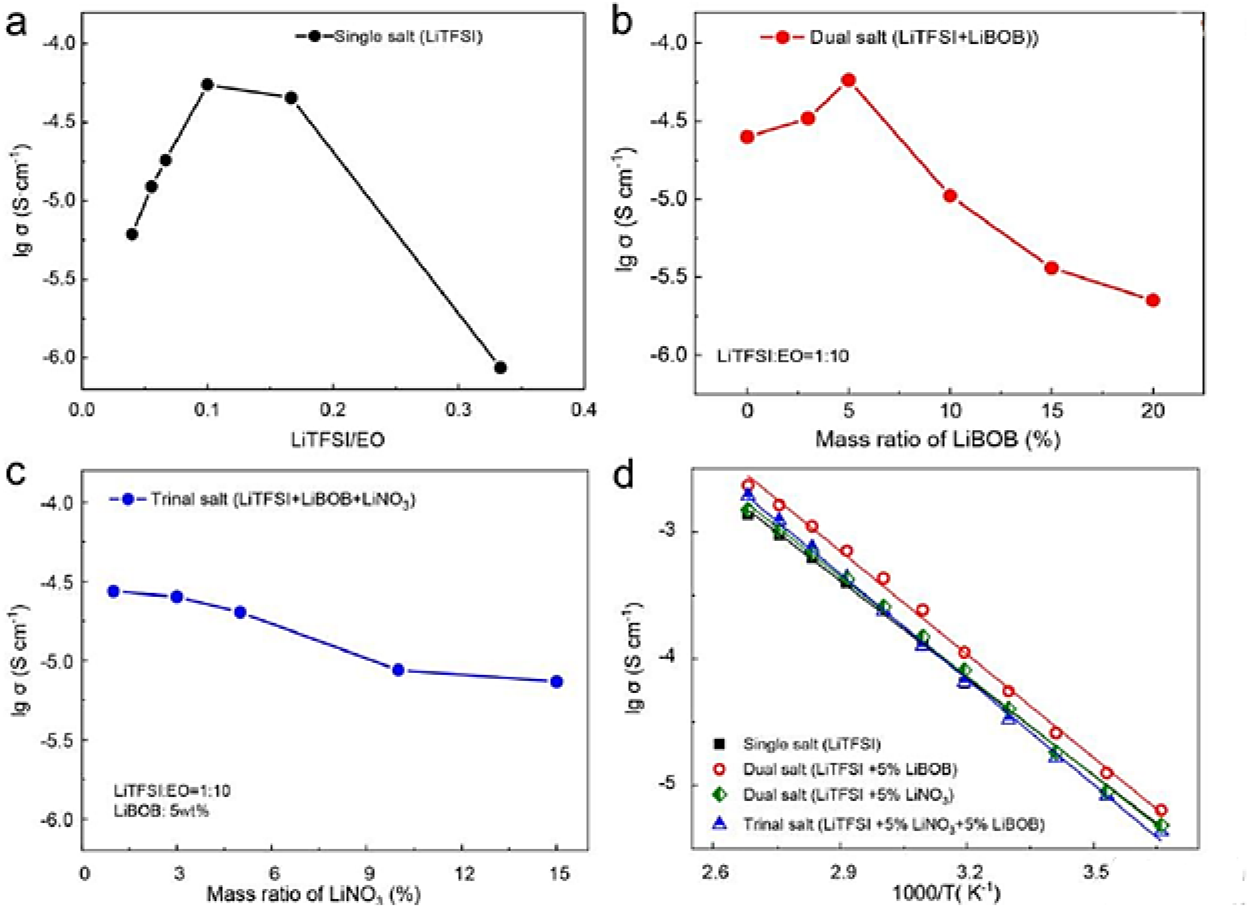

Figure 2.2: Lithium-ion conductivity regulation of PEO SPE. (a) single salt (LiTFSI) SPE with different ratios of LiTFSI, (b) dual salt (LiTFSI and LiBOB) SPE electrolyte with different ratios of LiBOB, (c) trinal salt (LiTFSI, LiBOB, and $LiNO_3$) SPE with different ratio of $LiNO_3$, (d) 78

Poulsen et al.[127] also reported that a PEO-based polymer electrolyte having a single salt has lower conductivity than one based on a combination of both PEO-$CaBr_2$-CaI_2 in a ratio of 30:1:1. Similarly, the conductivity of PEO electrolytes with zinc bromide ($ZnBr_2$) and lithium bromide (LiBr) salt combination has also been enhanced.[128] However, the ionic conductivity decreases to ~1.99×10^{-5} S cm^{-1} on adding a third salt, $LiNO_3$, with improved mechanical strength and glass transition temperature from -47.02 to -40.48 °C. Each salt (LiTFSI, LiBOB, and $LiNO_3$) plays a unique role, with LiTFSI serving the primary role in ionic diffusion. Each salt has complemented the other and improved the electrochemical stability and performance of LIBs.[126]

2.3.2 Modifying Polymer Host

The low conductivity of SPEs is often attributed to the crystalline nature of the polymer matrix. Nevertheless, the abovementioned problem can be minimized by minor modifications to the structure of the host polymer. One potential approach involves introducing various functional groups to the chemical structure of PEO to induce changes and modifications. Another way is to transform the linear chain of a PEO-based electrolyte into a hyper-branched structure. Jing et al.[129] has created hyper-branched PEO/LiTFSI SPE grafting with another PEO having linear chains to increase the ionic conductivity without reducing mechanical strength. The schematic representation of the design and synthesizing process of two types of hierarchical HB, PEO-based polymers are illustrated in Figure 2.3. Such arrangement decreases the crystallinity of linear PEO, increasing ionic conductivity. The reported value of improved ionic conductivity for HB electrolytes is ∼3.5×10^{-5} S cm^{-1}, which is ∼50% higher than that of HB-80nm-1k and 10 times higher than the corresponding PEO macromonomer electrolyte, L2k (Figure 2.4)

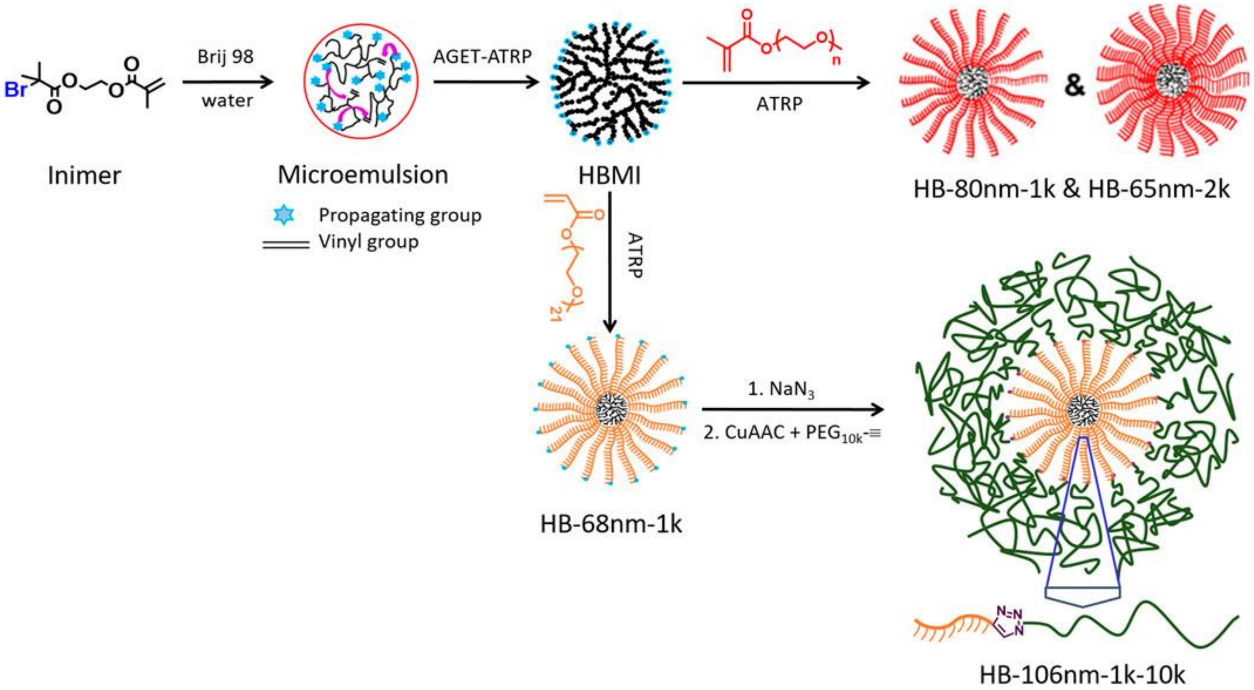

Figure 2.3: Schematic representation of the synthesis routes of HB PEO (HB-1k; HB-2k) and end-capped HB PEO (HB-1k-10k). Reprinted with permission from Ref.[129] copyright © 2021, Frontiers in Chemistry.

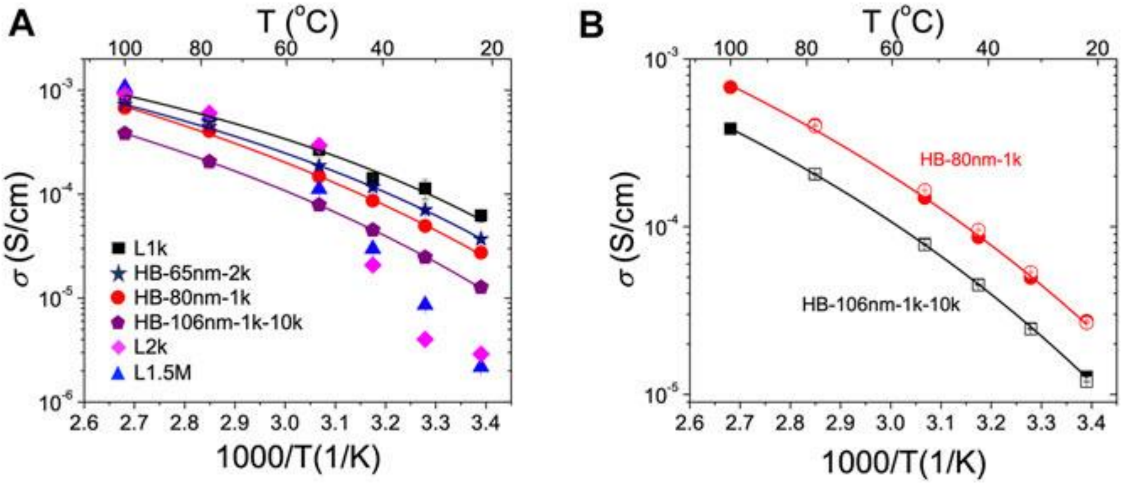

.Figure 2.4: Effect of HB PEO molecular architecture on the temperature-dependent lithium ionic conductivity. (A) HB and linear PEO electrolytes, and (B) HB-80nm-1k (circles) and HB-106nm-1k-10k (squares) upon heating (filled symbols) and cooling (open symbols). Reprinted with permission from Ref. [129] copyright © 2021, Frontiers in Chemistry.

For the HB-80nm-1k electrolyte, the equivalent linear chain electrolyte, L1k, does not crystallize and therefore has a higher room-temperature conductivity than the HB polymer. Lehmann et al.[130] synthesized an SPE (PEO/PEI/LiTFSI) by crosslinking PEO with poly(ethylene oxide) (PEI) in 2016 and reported an improved higher ionic conductivity of 3.90 × 10^{-5} S cm^{-1} at 40 °C from 1.50 × 10^{-6} S cm^{-1} which is in case of only PEI having a same molecular mass (M_w = 600 g mol^{-1}) and salt (LiTFSI). T_g also increased from -65 °C to -33 °C. The reported improved tensile strength value was 0.47 MPa, and the transference number was 0.76 at 40 °C. Calvo et al.[131] conducted a systematic study on an electrolyte prepared by crosslinking poly(ethylene glycol) diacrylate with PEO as shown in Figure 2.5.

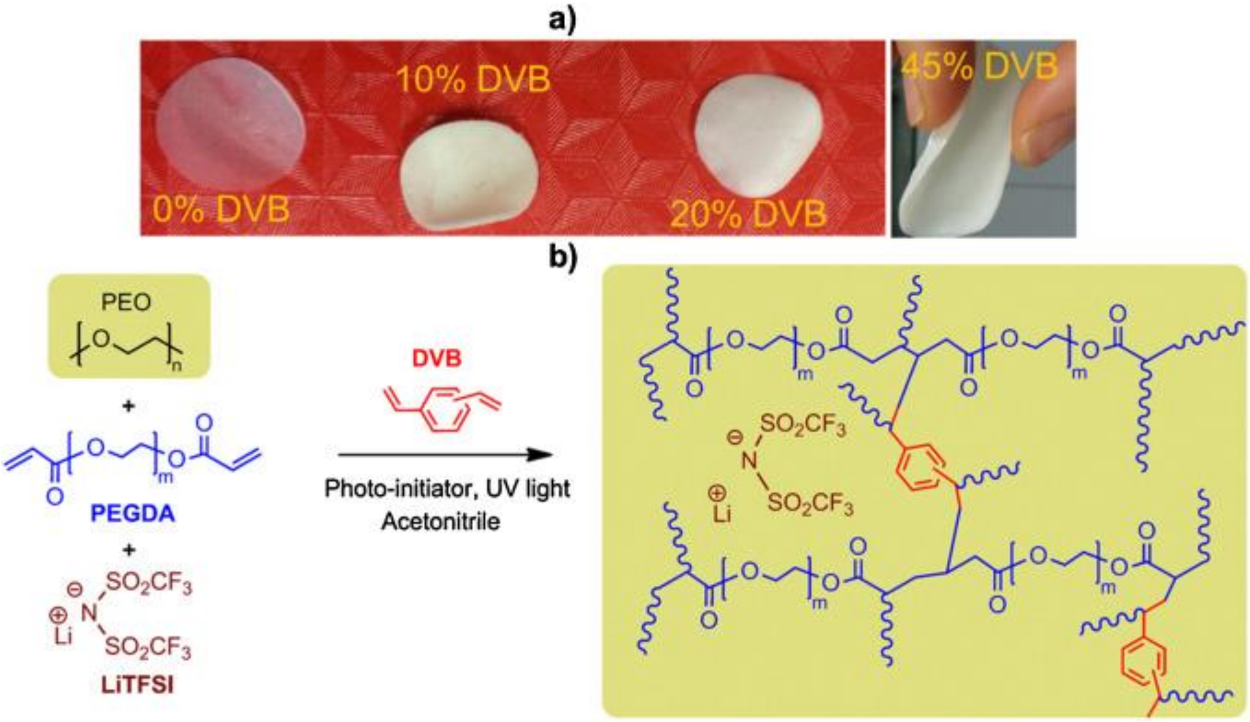

Figure 2.5: (a) Self-standing SPEs with different DVB concentrations, and b) Schematic of UV-induced preparation of semi-interpenetrated network based on PEO matrix. Reprinted with permission from Ref. [129] copyright © 2021, Frontiers in Chemistry.

The authors studied the concentration effect of divinyl benzene (DVB) in a PEO/PEGDA/ LiTFSI SPE. The reported values of Li-ion conductivity, transference number, and a higher electrochemical window were 0.14 mS cm^{-1}, 0.21, and 4.30 V, respectively, when the concentration of DVB was 10% mol (Figure 2.6).

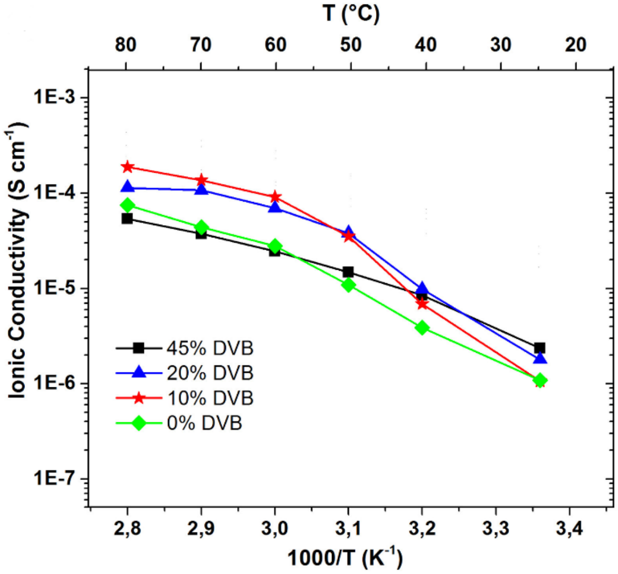

Figure 2.6: Temperature-dependent ionic conductivity of SPEs containing different DVB %. Reprinted with permission from Ref. [129] copyright © 2021, Frontiers in Chemistry.

Recent research by Tsai et al.[132] shows how solute diffusion affects the crosslinking material density. The author has shown that polymer crosslinking significantly affects the regulation of solute diffusivity and the mechanical characteristics of polymers. The compatibility of the electrolyte and the electrode connecting surfaces must be considered while improving the performance of the PEO-based SPEs through blending, copolymerization, grafting, etc. The instability of $LiCoO_2$ when coming in contact with PEO-based SPEs limits their use in high-energy-density batteries. Fu et al. created an ultrathin PEO-based SPE containing double-salt and a cross-linked network,[133] which significantly boosts the amorphous area and ionic conductivity of the SPE at RT. Also, it can effectively prevent the breakdown of PEO chain segments at the connecting surface of the electrolyte and the cathode. The resulting SPE is also chemically stable at the electrode and provides a satisfactory capacity retention rate and cycle performance of the LIB. This strategy of modifying polymer enables the use of PEO-based SSEs in high-voltage, solid-state rechargeable lithium batteries at RT.[131, 134]

2.3.3 Blended Solid Polymer Electrolyte

Blending two or more polymers is the most reasonable and practical way to create flexible, highly ion-conductive SPEs with good mechanical strength. It is more cost-effective than the other methods mentioned before because they use additional materials like initiators, linker agents, radiation sources, etc., in their production.[135] This method prepares a solution of two or more miscible polymers and a salt with a suitable solvent. The following are some benefits that the proper selection of polymers can attain to blend and use as an electrolyte in LIBs;

- low T_g,
- improved Li-ion conductivity,
- good thermal stability, and
- increased mechanical strength

The literature shows a large number of studies on the blending of PEO-based SPEs with PVDF,[135] PMMA,[136] polystyrene (PS),[137] and polyvinylpyrrolidone (PVP),[138] to enhance the conductivity of SPEs. The high dielectric constant, the strong electron-withdrawing ability of fluorine present in the functional groups, and the good electrochemical and thermal stability of PVDF make it a good choice to create membranes in SPEs.[139, 140] According to Fan et al.,[141] combining PEO and PVDF can reduce the crystallinity of PEO, enhance ionic conductivity, and increase the mechanical strength. He et al.[142] created a flexible garnet-based CSSE composed of LLZO, PEC, (P(VdF-HFP), and LiFSI. High t^+ approaching to a value of 0.82 and a good electrochemical stability window of 5.0 V vs. Li/Li+ at 55 °C have been demonstrated. Patla et al.[135] examined the mixing of PEO host polymers and PVDF membranes doped with ammonium iodide (NH_4I) salts. When mixed in the right proportions (8:2), they can enhance the amorphous portion of the polymer matrix and obtain ionic conductivity of up to 1.01×10^{-3} S cm^{-1}. Also, including PVDF improves the ion-polymer interaction, leading to an increased ion-ion dissociation. Another research work[143] used a blending approach in combination with a grafting technique to prepare SPE using PEG and sulfonated polyether ether ketone (SPEEK) as the polymer hosts and $LiClO_4$ lithium salt. (Figure 2.7)

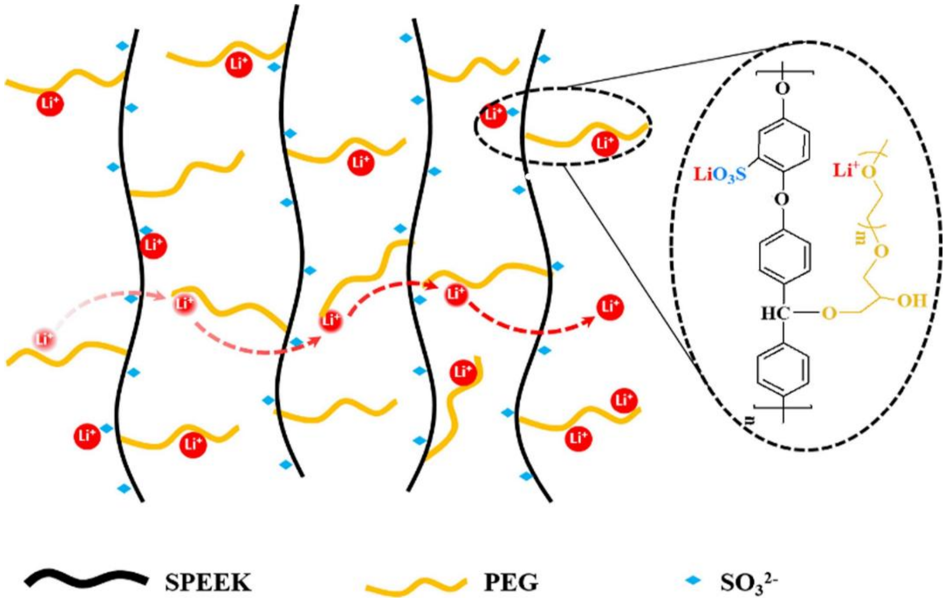

Figure 2.7: The Schematic representations of the Li-ion transport in SPEEK-g-PEG. Reprinted with permission from Ref. [143] copyright © 2017, Electrochimica Acta.

The reported ionic conductivity in the case of combining blending of polymers with grafting is higher (~10^{-5} S cm^{-1}) as compared to ionic conductivity (~10^{-6} S cm^{-1} at 30 °C) attained by SPE prepared by straightforward blending of two polymers (Figure 2.8). Thus, grafting of polymers can reduce the crystallinity of PEG more effectively than blending.

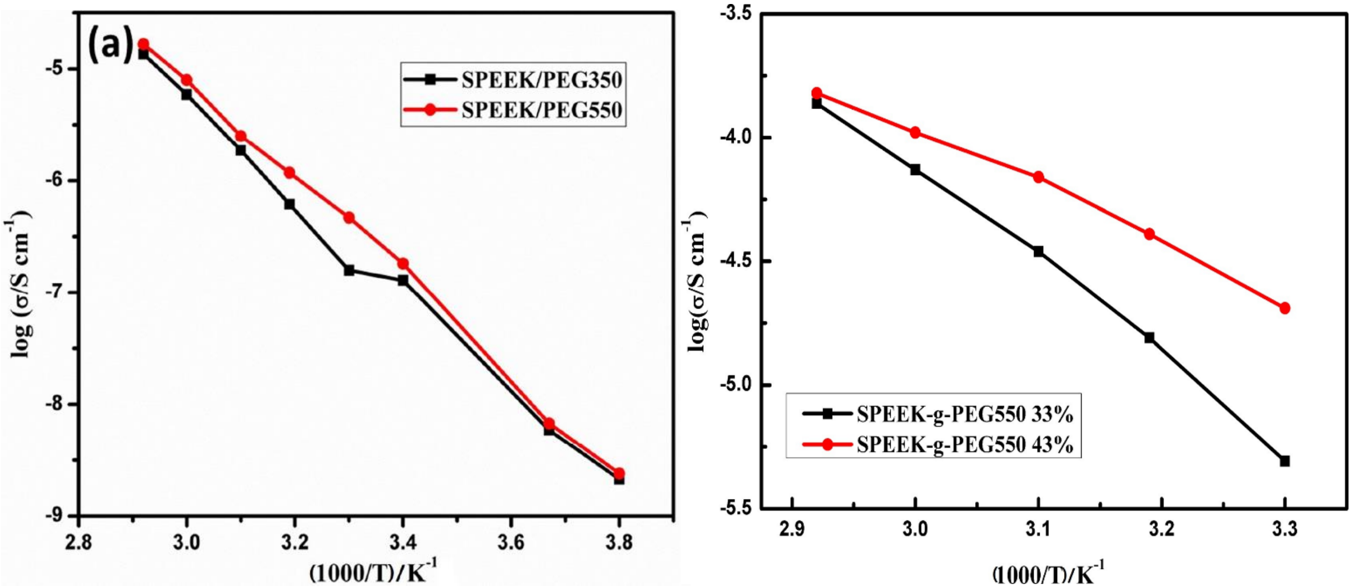

Figure 2.8: Temperature dependence of ionic conductivity for SPEEK/PEG blends (a) with different PEG molecular weights, and (b) with various the grafting ratio of PEG. Reprinted with permission from Ref. [143] copyright © 2017, Electrochimica Acta.

Sengwa et al.[144] discussed the impacts of the preparation procedure of blended SPE on ionic conductivity. They prepared an SPE by mixing PMMA and PEO polymers in a 1:1 ratio and LiTFSI as salt using four different techniques. They concluded that ionic conduction is different in each preparation procedure. The highest ionic conductivity is 1.99×10^{-6} S cm^{-1} attained by PMMA/PEO polymer blends prepared by microwave irradiation, and the lowest is 0.11×10^{-6} S cm^{-1} in the case of ultrasonication. Similarly, Liu et al.[145] separately cross-linked the polyether amine and polyetherdiamine with (3-glycidyloxypropyl)trimethoxysilane (GLYMO) and poly(ethylene glycol) diglycidyl ether (PEGDGE) and reported improved results of ionic conductivity of 0.120 mS cm^{-1} at 30°C and 0.830 mS cm^{-1} at 80°C using blending and crosslinking routes together. The T_g is also increased to -43.6 °C in a $LiFePO_4$/Li battery. According to the literature,[146, 147] solid electrolytes made by copolymerizing or combining several polymer electrolytes can improve the performance of SPEs.

2.3.4 Adding a Plasticizer in SPEs

The addition of plasticizer is another possibility to increase the ionic conductivity of SPE.[104, 148, 149] Different plasticizers affect the ionic conductivity of SPEs differently depending on their characteristics. For example, EC has a high dielectric constant, which helps in salt dissociation and improves ionic conductivity by reducing the ion-ion interactions and formation of ion clusters. Low viscosity is another characteristic of a plasticizer that governs ion mobility. Additionally, adding a plasticizer to an electrolyte allows for more space for ion transit.[148, 149]

Adding a low molecular weight PEG in the PEO-KI electrolyte can achieve higher ionic conductivity. PEG served as a plasticizer rather than a secondary polymer in such cases. Ions can also migrate through PEG alongside PEO segmental motion. Thus, increased ion transport channels are responsible for the enhancement of ion conductivity. The ionic conductivity of pure PEO is about 10^{-10} S cm^{-1} at room temperature which increases sharply to 10^{-7} S cm^{-1} in PEO with 5 wt.% KI salt and to 10^{-6} S cm^{-1} in PEG blend PEO with 5 wt.% KI salt. For all compositions of the PEO blend PEG with KI salt shown in Figure 2.9, the ion conductivity increases with the increase in temperature. This increase has occurred in all the blend electrolyte films.[150] However, due to their volatility and flammability, liquid plasticizers pose safety concerns in practical applications, limiting their suitability for real-world usage.[151]

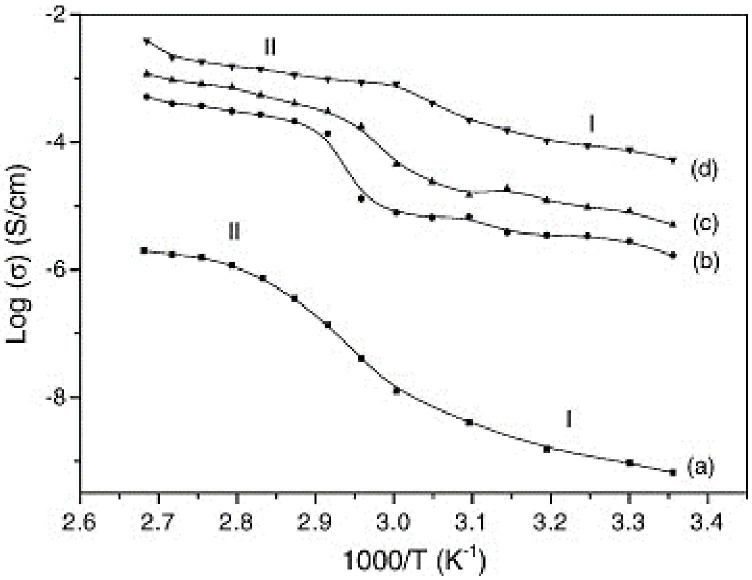

Figure 2.9: Temperature dependence ionic conductivity of (a) Pure PEO, (b) 5%, (c) 10%, and (d) 20% KI salt in PEO blend PEG. Reprinted with permission from Ref. [150] copyright © 2006, Solid State Ionics.

A different strategy is to use a solid plasticizer in polymer electrolytes to reduce the crystallinity of PEO and increase ion-ion dissociation. SN is a typical molecular plastic crystal material that can serve as a flexible and plastic medium for dissolving different lithium salts (including LiTFSI, $LiBF_4$, and LiSCN) and facilitating lithium ion movement.[152]The melting point of SN is 58.1 °C, and it also has good electrochemical stability. Below 40 °C, the monoclinic crystal structure of SN has a predominately gauche conformation, but beyond that temperature, a conformational change from monoclinic to a body-centered cubic (bcc) plastic crystal has occurred. The high degree of polarity and plasticity of SN provides an opportunity to make a plasticized solid polymer electrolyte (PSPE) system in which SN plastic crystal serves as a solid plasticizer.[153] In the literature, it has been shown that adding the SN to a polymer and lithium salt mixture significantly improved the ion conductivity and worked well to separate the Li-ions.[154, 155] Above all, safety concerns associated with using liquid plasticizers might be avoided by using SN.

Because of the high dielectric constant (55 at 25 °C), SN strongly tends to dissolve lithium salts, increasing the concentration of free charge carriers (Li^+) and interaction between Li-ion and nitrile groups which is required to improve lithium-ion conductivity.[156] Recently, many authors reported using succinonitrile as a flexible addition to polymer electrolytes.[157, 158] Figure 2.10a depicts the temperature dependence of ionic conductivities for the (x) PEO-(y) SN-5% LiTFSI electrolyte films. The conductivity of the 25% SN samples was about 1×10^{-3} S cm^{-1} at 30 °C, approximately 10 times the magnitude of 95% PEO-5% LiTFSI film at the same temperature. It is also observed for the lower temperatures (Figure. 2.10b) that the ionic conductivity first increases with increasing content of SN, reaching a maximum value at 25% of SN followed by a decrease in ionic conductivity with further increase in SN content. [157, 158]

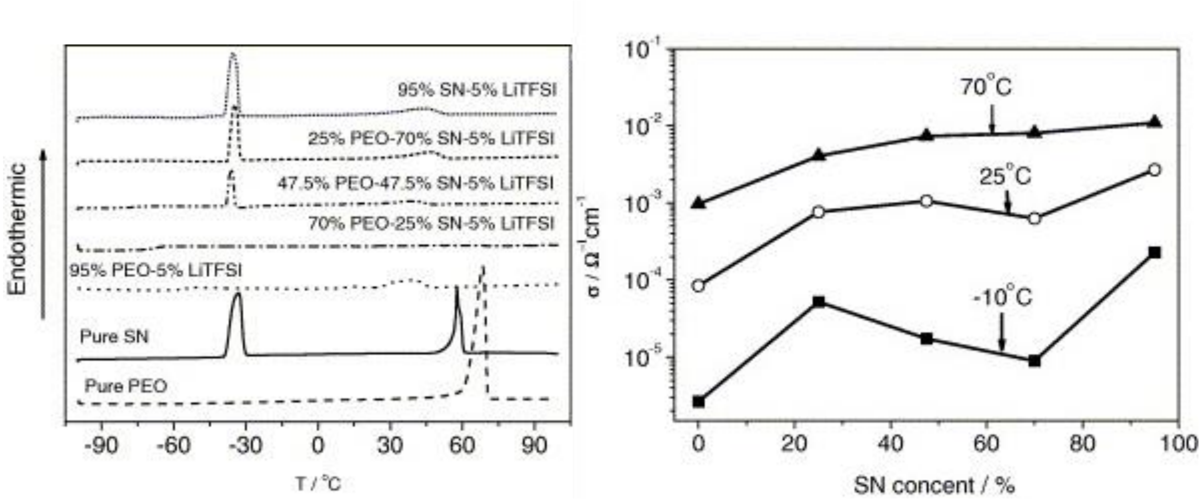

Figure 2.10: (a) DSC curves for pure PEO, SN, and (x) PEO-(y) SN-5% LiTFSI electrolyte films. x + y = 95%. (b) The ionic conductivities of the (x) PEO-(y) SN-5% LiTFSI as a function of SN content at different temperatures. Reprinted with permission from Ref. [157, 158] copyright © 2006, Electrochemistry Communications.

As evidenced by DSC (Figure 2.10a), there exists after the maximum (beyond 25%) some amount of unreacted SN. As SN is a non-ionic plastic crystal, the unreacted amounts of SN could act as an insulator blocking ion motion similar to that observed for the case with oxide filler resulting in a decrease of ionic conductivity. R. Yang et al.[155] made a PEO-LiTFSI-SN SPE by using the solution casting technique. The ionic conductivity of SPE improves to a value of 7.0×10^{-4} S cm^{-1} at RT, which is significantly greater than the value without the addition of SN. Zha et al.[159] reported that ionic conductivity increases from 1.9×10^{-5} S cm^{-1} to 1.22×10^{-4} S cm^{-1} at 30 °C when SN, a solid plasticizer was added into the LLZTO/PEO CSSE, and high Li-ion transference number to 0.410. The discharge capacity of Li/$LiFePO_4$ (LFP) cell using LLZTO/PEO/SN plasticized CSSE was 151.1 mAh g^{-1} when operated at 0.5 C and 60 °C. Because of the high dielectric constant of SN, it maintains its single plastic phase in a temperature range varying from 35 to 62 °C.[160]

Another study shows an ultrathin (15 nm) CSSE membrane made of LLZTO/PVDF-HFP/LiTFSI/SN with a small amount of liquid electrolyte, giving a high ionic conductivity of 6.53×10^{-4} S cm^{-1} and Li-ion transference number 0.55 at 30 °C.[161] Similarly, the author reported 9.10×10^{-5} S cm^{-1} ionic conductivity at 25 °C for a PEO-based CSSE comprising PEO/LiTFSI-1%LGPS-10%SN.[162] While PEO-LiTFSI shows a 15-fold increase in ionic conductivity, its main characteristics are a wide electrochemical range (0-5.5V) and excellent metallic lithium compatibility. Although the ionic conductivity of SPEs can be increased by adding SN, the mechanical property has been severely compromised, because the addition of SN decreases the crystallinity of the polymer and increases molecular bond mobility.[156] Different methods can be applied to make the electrolyte membrane to avoid the loss of mechanical properties of SPEs. Wang et al.[156] proposed a PEO/PVDF blended SPE system with SN as a plasticizer and $LiClO_4$

salt. Microporous PVDF film in PEO acts as the support layer and increases the mechanical strength of the PEO/PVDF/$LiClO_4$/SN blend. The improved Li-ion conductivity and transference number, in addition to SN, are approximately 1.7×10^{-3} S cm^{-1} at 80 °C and 0.367, respectively, and the maximum stress that PEO/PVDF/$LiClO_4$/SN SPE can bear is 3.37 MPa, which is 10 times higher than the SPE without PVDF film (Figure 2.11).

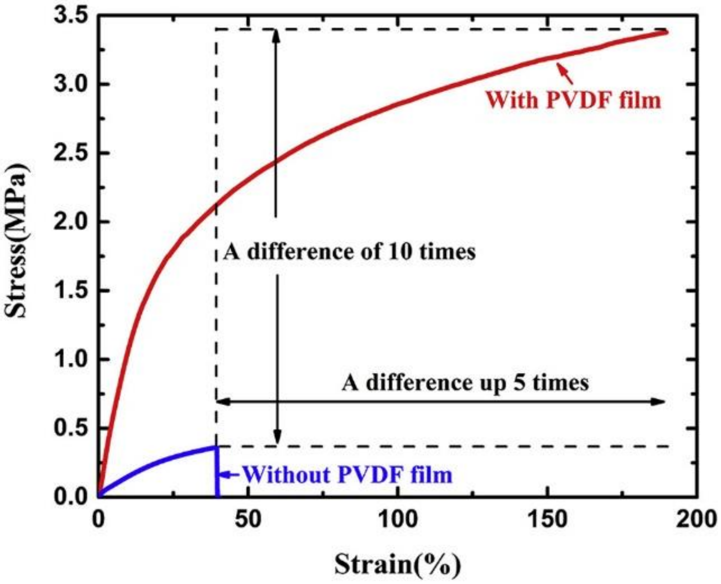

Figure 2.11: The stress-strain curves of conventional ASPE without PVDF supporting layer (blue) and with PVDF supporting layer (red). Reprinted with permission from Ref.[156] copyright © 2020, Journal of Electroanalytical Chemistry.

He et al. [163] used a photopolymerization technique with the photo-initiator bis(2,4,6-trimethyl benzoyl)-phenyl phosphine oxide but without a solvent to create a film comprising a polymer PEGDA (of large $M_w = 6000$ g mol^{-1}) and LiTFSI. They added SN in the PEGDA/LiTFSI electrolyte as a plasticizer. A crosslinking network in PEGDA, LiTFSI, and SN increases the amorphous region of the polymer, which increases the room temperature ionic conductivity to a value of 1.10×10^{-3} S cm^{-1}, along with a 4.80 V electrochemical stability window. The mechanical strength of the electrolyte prepared by the above-mentioned technique has also been improved to a high tensile strength (0.24 MPa) with 84% elongation at break. Chen et al.[162] created PEO/LiGePS/SN SSE using a solution casting method. They discovered an increase in ionic conductivity of up to 9.10×10^{-5} S cm^{-1} at 25 °C, which is 15 times more than the reported ionic conductivity without SN addition. By suitably optimizing the content of SN, researchers have discovered two polymer electrolytes ((PVDF-HFP)/LiTFSI/SN and P(VDF-HFP)/LiBETI/SN) with high ionic conductivity (0.35 mS cm^{-1} at 30°C) and excellent mechanical stability. Here, SN is utilized as a dispersant, and the PVDF helps build the network with outstanding mechanical properties. Additionally, SN particles can frequently create a channel for the movement of ions in the interphase, which improves ionic conductivity.[85, 164]

Although numerous experimental research has been conducted to comprehend how SN affects ionic conductivity in SSEs, the mechanics at the molecular level still need to be further investigated.[154, 158, 164, 165] There is a particular need to understand the variables affecting ion dynamics and transport in SN-loaded composite systems. CMD is a method for gaining an insight physical understanding of the ion-transport pathways at the atomistic level. Hence, it would be helpful to conduct atomistic molecular dynamics simulations for the explanation of the dynamic properties of Li-ion in SN-based SPEs.

2.4 Summary

Selecting the optimal electrolyte for practical LIBs can present a formidable challenge, owing to the unique advantages and disadvantages inherent in each available option when applied to real-world scenarios. PEO with continuous oxygen vinyl group (CH_2CH_2O) emerges as the best candidate in the preparation of SPEs because of its ion transport capabilities and direct connections to the alkaline salt. However, low room temperature ionic conductivity (~10^{-6} to 10^{-8} S cm^{-1}) of PEO-based solid polymer electrolytes is a critical issue that needs to be resolved. By thoroughly reviewing the literature, different methods are available to improve the RT Li-ion conductivity of the polymer electrolytes.

The study's objective is to create a novel solid polymer electrolyte (SPE) using a combination of polymer blending and plasticizer addition, employing CMD simulation techniques. PEO and PVDF polymers were blended by adjusting PVDF weight percentages within the PEO matrix. Subsequently, an SN plasticizer was introduced into the prepared PEO/PVDF/LiTFSI blended solid polymer electrolyte. GROMACS, an established molecular dynamics simulation package, was used to design and analysis of ion dynamics and transport properties within the prepared PBSPE system.

Chapter 3. Simulation Section

3.1 Preparation of Computational Models of Electrolyte Materials

3.1.1 Molecular Structure of PEO

In the present study, PEO is the host polymer with a methyl terminal group having the chemical structure CH_3-[CH_2-CH_2-O]-CH_3. According to the available literature, PEO chains featuring methyl end groups exhibit superior lithium ionic conductivity compared to hydroxyl groups.[166] The molecular structure of the PEO repeating unit (ethylene oxide) and methyl as a terminal group (differentiated by colors) is shown in Figure 3.1.

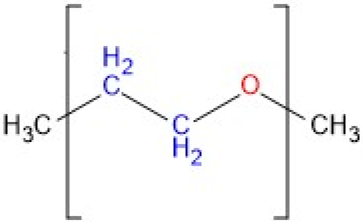

Figure 3.1: Molecular structure of PEO (EO as a repeating unit and CH3 as an end terminal) used in this research work

Initially, two SPEs with varying chain lengths in this work. Short-chain PEO (S-PEO) molecular system consists of 18 ethylene oxide monomer (CH_3-[C_2H_4O]$_{18}$-CH_3) with a molecular mass of 792.9 g mol^{-1} and a long-chain PEO (L-PEO) molecular system consisting of 90 ethylene oxide monomer (CH_3-[C_2H_4O]$_{90}$-CH_3) having molecular mass 3964.5 g mol^{-1} is used. Such models were built to account for the effect of the molecular mass of polymer chains on the dynamic properties of the ions (Li^+ and $TFSI^-$). Because the properties of PEO-based structures depend strongly on the molecular weight of each chain. Lower molecular weight structures tend to be more flexible and enable larger ionic diffusion coefficients, albeit with reduced mechanical stability.[166, 167]

Further LPEO having a molecular mass of 3964.5 g mol^{-1} is used to study the impact of polymer blending and plasticizer addition on ion dynamics. Because with adequately large molecular weights, both the diffusion coefficient and mechanism become independent of chain length and the specific nature of polymer end groups.[168] To construct a simulation cell consisting of a polymer/salt mixture, the initial molecular structure of PEO was built by repeating the EO monomer shown in Figure 3.1. The end groups are set as CH_3 groups to avoid end-group interaction with each other, plasticizer, and nanoparticles.

3.1.2 Molecular Structure of PVDF

PVDF polymer is used for blending in host polymer (PEO) because of its good compatibility with PEO.[169] As a non-coordinating polymer, PVDF has no known atomic groups that can interact with Li cations directly. As a non-coordinating polymer, PVDF has no known atomic groups that can interact with Li-ions directly. Whereas, PEO has oxygen atoms in its monomer which can directly interact with the Li-ions and cause the lithium ions to hop.[102] The high dielectric constant ($\varepsilon \approx 8.4$) and strong electron-withdrawing ability of fluorine in the functional groups of PVDF efficiently dissociates lithium salts to produce charge carriers for ionic conduction. This will improve the Li-ion conductivity.[156] The molecular structure for PVDF (F-[$C_2F_2H_2$]-H) with the naming convention is shown in Figure 3.3. The molecular mass for a single PVDF chain is 2323.85 g mol^{-1}. Initially, PVDF polymer (M_w = 2323.85 g mol^{-1}) is mixed in PEO with a fixed ratio of 1:2.5 and varying lithium salt concentration in the PEO/PVDF blend to select the Li: EO ratio, giving maximum ionic conductivity and lithium transference number.

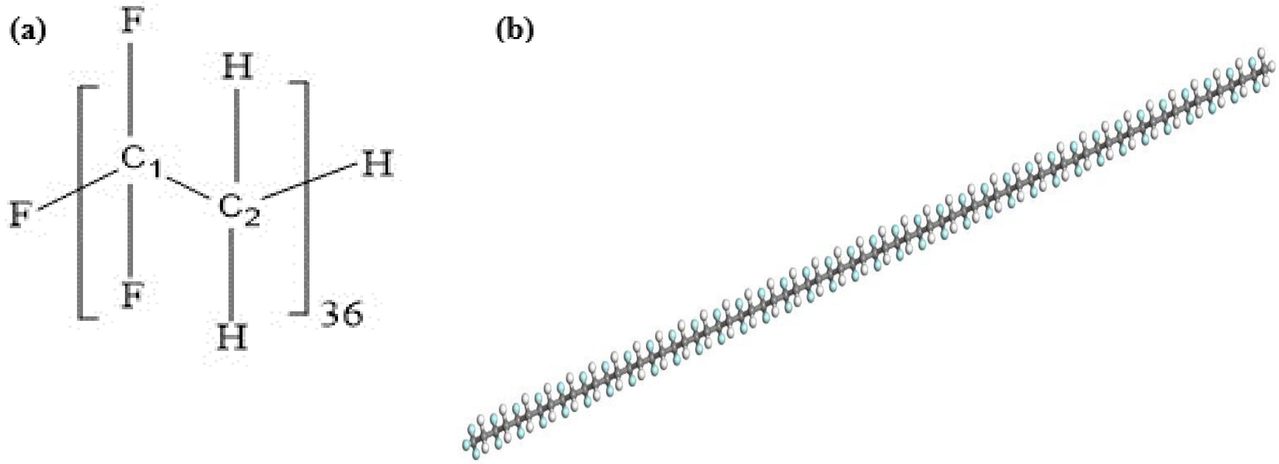

Figure 3.2: Molecular structure of (a) PVDF CF_3CH_3, and (b) PVDF chain with CF_2-CH_2 as repeating unit having F as left terminal atom and H as right terminal atoms.

3.1.3 Molecular Structure of LiTFSI

LiTFSI has been successfully used as a lithium-ion-containing salt for commercial lithium metal batteries based on SPEs. It has significantly superior chemical and thermal stability than other salts (such as $LiClO_4$/PEO).[170] The molecular structure of LiTFSI salt with the naming convention drawn and used in this simulation work is shown in Figure 3.4. Its molecular mass is 287.09 g mol^{-1}. The effect of salt concentration will also be studied by mixing the LiTFSI salt with varying concentration ratios in PEO polymers of different molecular mass and PEO/PVDF polymer blends.

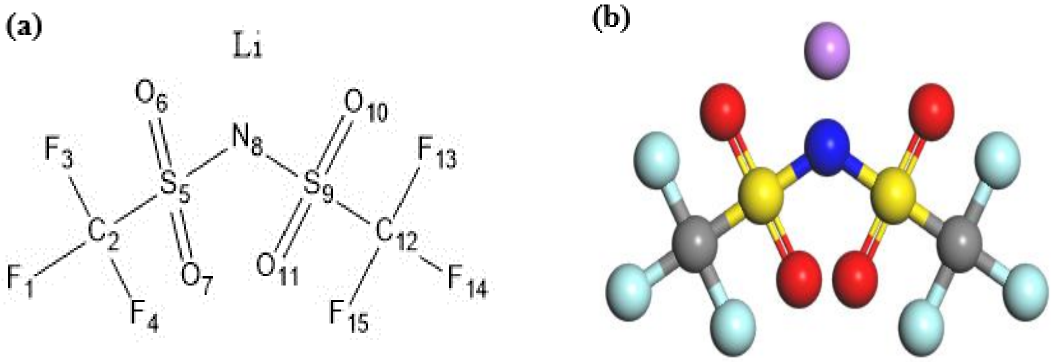

Figure 3.3: The initial molecular structure of (a) LiTFSI with the naming convention, and (b) LiTFSI molecule.

3.1.4 Molecular Structure of SN

SN is a solid plasticizer used as a promising electrolyte additive. Because of its strong polarity, SN can dissolve a variety of salts to boost ionic conductivity, and the solid nature of SN can match the requirement of SPEs. It has a plastic crystalline structure that is stable between 233 K and 331 K and is considered as a highly adjustable solid plasticizer.[164] SN plasticizer has a chemical structure [$CN-CH_2-CH_2-CN$] and a molecular mass of 80.09 g mol^{-1}. The molecular structure is shown in Figure 3.5, which is built by the MS and optimized at the DFT level using Gaussian-19[171] software. This optimized structure was further utilized in PEO/PVDF polymer blends.

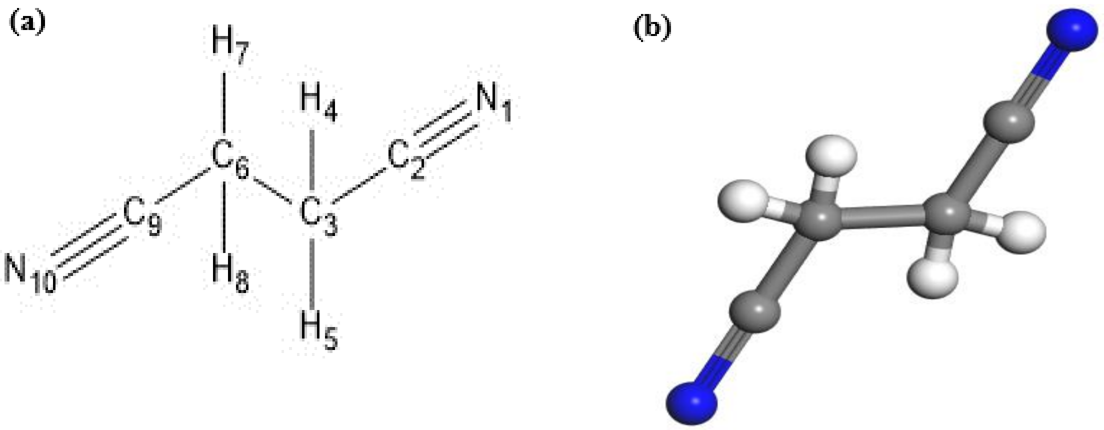

Figure 3.4: Molecular structure of (a) SN with the naming convention and, and (b) SN molecule.

The color code for each molecule used in this work is given in the following Table. 1.

Table 1: Color code for each molecule used in this work.

Atom name	**Color code**
C	grey
H	white
O	red
S	yellow
F	Light blue
N	Dark blue
Li	purple

3.2 Computational System Details

CMD simulations will be performed by using GROMACS (Groningen Machine for Chemical Simulations) software. GROMACS is a free, full-featured, easy-to-use molecular dynamics simulation package. It is available under the GNU Lesser General Public License

(LGPL). The ‘MSI-ANTEC computer system, having an Intel(R) Core (TM) i7-12700KF*20 processor with 64 GB RAM and a 64-bit Operating System will be used for CMD simulation.

3.3 Force Fields

CMD simulations will be conducted to investigate the dynamics and transport properties of Li-ion in PEO/PVDF/SN/LiTFSI, a PBSPE system. In this research work, the interaction potential between atoms of PEO, PVDF, LiTFSI, and SN is given by the OPLS-AA force field.[114] The OPLS-AA force field was chosen as it is optimized for a variety of biomolecules and organic solvents.[172-174] The general form of interaction potential employed in the OPLS-AA force field is:

$$(\mathrm{r}) = \mathrm{U}^{\mathrm{bonded}}(\mathrm{r}) + \mathrm{U}^{\mathrm{non-bonded}}(\mathrm{r}) \qquad (3.1)$$

$$\mathrm{U}^{\mathrm{bonded}}(\mathrm{r}) = \sum\nolimits_{\mathrm{bonds}} \frac{1}{2} \mathrm{k_r} (\mathrm{r} - \mathrm{r_0})^2, + \sum\nolimits_{\mathrm{angles}} \frac{1}{2} \mathrm{k}_\theta (\theta - \theta_0)^2 + \sum\nolimits_{\mathrm{torsions}} \frac{1}{2} \sum\nolimits_{\mathrm{n=1}}^{4} \mathrm{Cn} \, [1 + (-1)^{\mathrm{n+1}} \cos(\mathrm{n}\phi)] \qquad (3.2)$$

$$\mathrm{U}^{\mathrm{non-bonded}}(\mathrm{r}) = \sum 4\epsilon_0 \left[\left(\frac{\sigma}{\mathrm{r_{ij}}} \right)^{12} - \left(\frac{\sigma}{\mathrm{r_{ij}}} \right)^{6} \right] + \sum \frac{\mathrm{q_1 q_2}}{4\pi\epsilon_0 \mathrm{r_{ij}}} \qquad (3.3)$$

where Eq (3.2) gives the interactions arising from bond stretching, angle bending, and torsions respectively, and Eq (3.3) gives the non-bonded interactions. The 1st half of Eq (3.3) is the van der Waals interactions and is modeled with the Lennard-Jones (LJ) potential, whereas the 2nd half is the electrostatic interactions and quantified by the Coulombic electrostatic potential. The values for nonbonded LJ parameters σ and ϵ are given by Lorentz–Berthelot’s geometric mixing rules and the general form of the equation is;

$$\varepsilon_{\mathrm{ij}} = \sqrt{\varepsilon_{\mathrm{i}} \epsilon_{\mathrm{j}}} \qquad \sigma_{\mathrm{ij}} = \sqrt{\sigma_{\mathrm{i}} \sigma_{\mathrm{j}}} \qquad (3.4)$$

The LJ parameters for PEO, PVDF, LiTFSI, and SN are also taken from the OPLS-AA force fields. The nonbonded intramolecular interactions related to atomic pairs spaced by three bonds will be calculated using a scaling factor of 0.5, and no scaling factor will be employed for nonbonded intramolecular interactions for pairs of atoms placed beyond three bonds. The charges assigned to the atoms of the polymers PEO, and PVDF are the default ones within the OPLS-AA force field given in Table 2.

Table 2. LJ parameters and partial atomic charges for PEO using OPLS-AA force field

Sr #	**Atom type**	q(e)	σ(Ȧ)	ε **(KJ/mol)**
PEO				
1	C	0.140	3.500	0.276
2	H	0.030	2.500	0.126
3	O	-0.400	2.900	0.586
4	C	-0.180	3.500	0.276
5	H	0.060	2.500	0.126
PVDF				
6	C1 (t)	0.36	3.550	0.293
7	C1 (r)	0.24	3.550	0.293
8	C2 (t)	-0.18	3.550	0.293
9	C2 (r)	-0.12	3.550	0.293
10	F	-0.12	2.950	0.222
11	H	0.06	2.500	0.125

Here, (t) stands for terminal, and (r) stands for repeating.

In the case of SN, the structure has been optimized at the DFT level using Gaussian-19[171] software. The partial atomic charges are recalculated using the electrostatic potential (ESP) method as given in Table 3.

Table 3. LJ parameters from the OPLS-AA force field and partial atomic charges for SN were calculated by DFT using the ESP method.

Sr #	**Atom type**	q(e)	σ(Ȧ)	**ε (KJ/mol)**
1	N	-0.445	3.250	0.711
2	C	0.317	3.550	0.293
3	C	-0.071	3.550	0.293
4	H	0.100	2.500	0.125
5	H	0.100	2.500	0.125
6	C	-0.081	3.550	0.293
7	H	0.102	2.500	0.125
8	H	0.102	2.500	0.125
79	C	0.321	3.550	0.293
10	N	-0.445	3.250	0.711

3.3.1 Charge Rescaling

In atomistic MD simulations, the charge rescaling approach is frequently used to reproduce the structural and transport properties of alkaline salts in organic electrolyte systems.[175-178] It is an alternative method to the use of the more complex polarizable force fields which are computationally expensive. The charge rescaling will be employed because of the limitation of LJ models, which produce inconsistent results compared to experimental ones when fully charged ionic species are used.[179, 180] In simulations of polymer electrolytes, a scaling factor between 0.5

and 0.85 has been commonly used for salt ions in recent years,[175, 181-183] which has been shown to better reproduce the experimental diffusivities.[184] It is worth highlighting that a smaller charge rescaling is expected to shift the g(r) peak closer to the value obtained with polarizable forcefields. However, it can further underestimate the conductivity and, therefore, worsen the comparison between the computed and experimental conductivity. Based on the success of the previous studies,[168, 175, 180, 185-191] the Li-ion charge is reduced to +0.7 to imitate the effects of induced polarization indirectly, and to neutralize the LiTFSI system. The scaling factor will be also applied to $TFSI^-$. A charge rescaling of 0.7, as adopted in this work, is deemed a reasonable compromise to reproduce the experimental structural and transport properties of the system. The DFT-optimized structure of $TFSI^-$ using B3LYP exchange-correlation functional with the “tier2” standard basis set in the literature will be used. The partial atomic charges of LiTFSI are given in Table 4.[192]

Table 4. LJ parameters from the OPLS-AA force field and the partial charges for LiTFSI

Sr #	**Atom type**	q(e)	σ(Å)	ε **(KJ/mol)**
1	Li	0.70	2.130	0.076
2	F1	-0.0445	2.950	0.222
3	C2	0.0312	3.500	0.276
4	F3	-0.0506	2.950	0.222
5	F4	-0.0496	2.950	0.222
6	S5	0.5046	3.550	1.046
7	O6	-0.2940	2.960	0.879
8	O7	-0.3030	2.960	0.879
9	N8	-0.2987	3.150	0.711
10	S9	0.5475	3.550	1.046

11	O10	-0.2930	2.960	0.879
12	O11	-0.3165	2.960	0.879
13	C12	-0.0380	3.500	0.276
14	F13	-0.0165	2.950	0.222
15	F14	-0.0359	2.950	0.222
16	F15	-0.0430	2.950	0.222

3.3.2 Parameters Settings for Simulation

Different parameters need to be defined to run each simulation. Leap-frog integrators will be used to integrate Newton’s equation of motion with a time step of 0.5 and 1 fs, depending upon the size of the molecular system.[120, 122, 193] The h-bond lengths are constrained using the LINCS algorithm with some tolerance up to which bond lengths and angles between two bonds for each molecule can rotate. The algorithm is inherently stable, as the constraints themselves are reset instead of derivatives of the constraints, thereby eliminating drift. Because of its stability, LINCS is especially useful for Brownian dynamics.[193, 194] The pressure in each simulation will be kept close to atmospheric (103216 Pa) by weekly coupling with a coupling constant of 0.5 ps and 2.5 ps using Berendsen (in the equilibration run) and Parrinello-Rahman barostat (in the production run), respectively.[185] The particle coordinates and the box dimensions are changed in this case. As this is an equilibrium molecular dynamics simulation, the isothermal compressibility will be kept the same (4.5×10^{-5} KJ mol^{-1} nm^{-1}) in all directions. V-Rescale ensemble with a coupling constant of 0.2 ps will be used to maintain the reference temperature.[195] The center of mass (COM) motion is automatically removed by GROMACS. The long-range VdW interaction potential is truncated at 1.1 nm.[196] To avoid the effects of truncating potential energy after a certain radius, a VdW modifier will be employed to shift the truncation radius to another specified value (1.095 nm in this work) and smoothly decrease the interaction potential to zero after that specified value. Dispersion correction for long-range interactions will be adopted. The PME [197] method is applied to calculate the electrostatic interactions with a truncating radius of 1.2 nm. The values of trajectories of coordinates and velocities will be stored after each 0.5 ps.

3.4 Simulation Procedures

3.4.1 Topology Generation

First, the topology files for all molecules (PEO, PVDF, LiTFSI, and SN) are generated using GROMACS. This needs the protein data bank (PDB) format file as an input which contains the information on the initial coordinates of all the atoms in the molecule. This will result in three output files with extensions gro, rtp, and posre. The rtp file contains the information for the OPLS-AA force-field data, whereas the posre file contains the atoms whose positions need to be restrained. The information in the rtp file is then rearranged to form a new file with the extension topol named the topology file. This individual topology contains information for force field parameters of all types of atoms.

3.4.2 Coordinate Generation

After topology file generation, the number of molecules needed to add to a simulation box must be specified in the topology file. A new gro file containing information on the physical location of each atom in all molecules is generated.

3.4.2.1 PEO/LiTFSI System

For the initial PEO/LiTFSI SPE system, PEO chains and lithium salt LiTFSI configuration are randomly added to prepare a less dense simulation box system by Packmol software.[198] In the case of the S-PEO electrolyte system, pure 75 chains of S-PEO will be mixed with different numbers of Li and TFSI ions to generate five PEO/LiTFSI systems (SPE1-SPE5) corresponding to the different salt concentrations of [Li: EO] = 0.02-0.20 by adding ions randomly into the simulation box. Similarly, 15 chains of L-PEO are solvated with LiTFSI in concentrations varying from [Li: EO] = 0.02-0.20, making another SPE system (SPE6-SPE10). For both S-PEO and L-PEO electrolyte systems, the details of the total number of atoms, the operating temperature, and the concentration ratio corresponding to each SPE system are given in Table 5.

Table 5**.** Total atoms for SPEO and LPEO loaded electrolyte system.

Model No.	**No. of PEO chains**	**Simulation Temperature (K)**	**No. of Li**	**No. of TFSI molecules**	**[Li: EO]**	**Total number of atoms**
S-PEO						
SPE1	75	363	27	27	0.02	9888
SPE2			54	54	0.04	10320
SPE3			108	108	0.08	11184
SPE4			162	162	0.12	12048
SPE5			270	270	0.20	13776
L-PEO						
SPE6	15	363	27	27	0.02	9888
SPE7			54	54	0.04	10320
SPE8			108	108	0.08	11184
SPE9			162	162	0.12	12048
SPE10			270	270	0.20	13776

The initial density will be kept low to easily dissolve LiTFSI molecules in the PEO matrixes and to avoid the potential energy trap caused by contact of ions with other atoms.

3.4.3 Workflow Diagram for MD Simulation on GROMACS

The general procedure required for MD simulation in this work is shown in Figure 3.6. Each procedure is explained in detail in the following subsections. The screen captures are taken at the end of each procedure using the OVITO software.

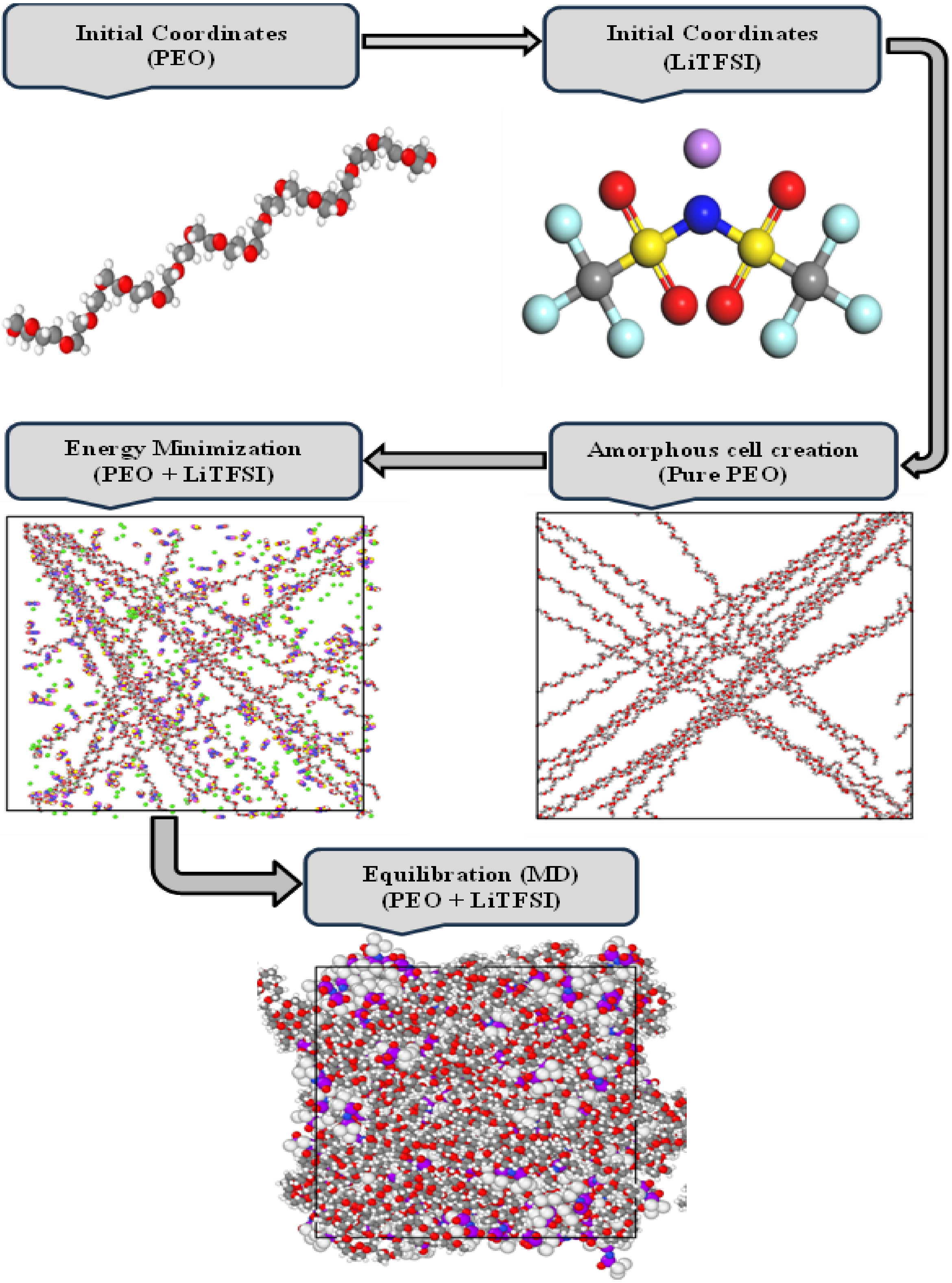

Figure 3.5: Workflow diagram for MD simulation in this work.

3.4.3.1 Energy Minimization (EM)

Energy minimization is an iterative procedure in which the coordinates of the atoms and possibly the cell parameters are adjusted so that the total energy of the structure is reduced to a minimum (on the potential energy surface). Minimization results in a structural model which closely resembles the experimentally observed structure.[199] Two commonly used EM methods, the steepest descent (sd) and conjugate gradient (cg) methods, are employed to minimize forces and PE of initial randomly constructed systems with a step size of 0.005 nm. The force and energy tolerance must also be specified to stop EM at some level. When the greatest force between two atoms is less than 10 kJ mol^{-1} nm^{-1} or there is no change in energy between two successive minimization steps, the EM is considered to be converged (Figure 3.7).

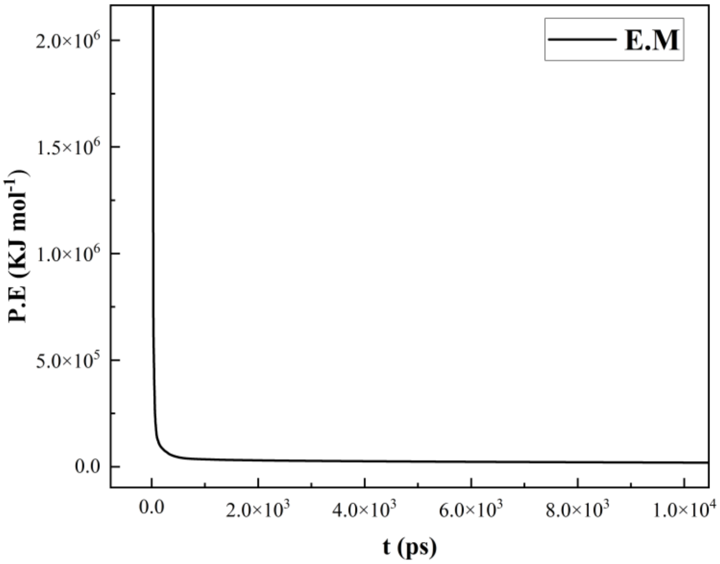

Figure 3.6: Energy minimization curve for PEO-LiTFSI system.

The sd method is not the most effective, but it is a reliable and simple one for reaching minimized energy levels.[193] During EM, the position of the solute (PEO) has been initially restrained by the positioned restrained theorem. In contrast, the ions are set free and allowed to solvate around the polymer equally. Then, the position restrictions on PEO chains are removed, and all atoms are allowed to relax.

3.4.3.2 Equilibration of the molecular system (NVT)

After the EM, the temperature and pressure of the simulation system are defined under two equilibration procedures: constant volume equilibration under NVT (isothermal-isochoric) and constant pressure equilibration under the NPT ensemble. The reference temperature is specified in the input file for NVT, and the minimized structures are used for a short NVT employing a Berendsen thermostat with a coupling constant of 0.2 ps for 50 to 55 ps, depending upon the size of the molecular simulation system. In this stage, the system is slowly heated to the initial simulation temperature of 363k. The high temperature 363 K is selected to observe the dynamics of Li-ion in PEO-LiTFSI SPE. This rather high temperature is chosen to make the dynamics of ions in the simulated system clear. Substantial changes occurred in the diffusivity of the electrolyte components around temperatures close to the melting temperature (T_m) of neat PEO (ca. 360 K). Moreover, at 363 K and lower, a direct comparison between the trends for the simulated and experimental conductivity can be presented since data exist for this temperature range.[200-203] According to the theorem of the thermostat, such small oscillations are acceptable if the average value obtained at the end of NVT is close to the target value. Figure 3.8 shows the convergence of the equilibration procedure toward the desired temperature. Equilibration of the SPE system under NVT essemble is achieved by using position restraints of polymer, and the salt is free to move about it. In such a case, the polymer can move but is energetically constrained.

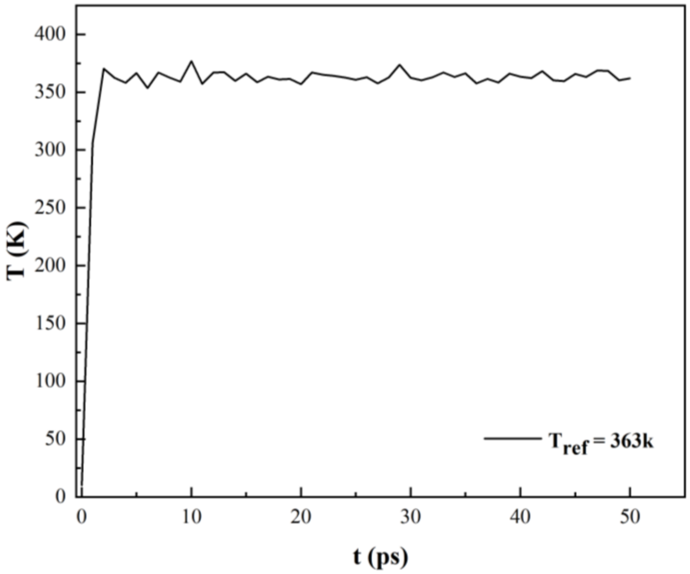

Figure 3.7: Temperature curve for PEO-LiTFSI system in NVT (MD) run.

3.4.4 Molecular Dynamics Equilibration Run (NPT)

The second phase of equilibration of the SPE system is to bring the initial less dense system of polymer chains close to experimental density. This is done under the NPT (isothermal-isobaric) ensemble in which pressure is maintained to a reference value along with the number of particles and temperature of the system. This is a continuation process of the 1st phase of equilibration under NVT. NPT simulation will be carried out using a Berendsen thermostat and barostat for 15 to 30 ns depending on the size of the simulation system. Equilibration of the SPE system in two different phases ensures the systems' useability for long production runs of more than 150 ns to analyze the transport properties of ions. The system smoothly tried to reach the actual value in the first 5ns of simulation time for the S-PEO electrolyte system, where L-PEO takes a longer time to reach the equilibrium value (~10 ns to 12 ns) and then oscillates with a small amplitude for the rest of the simulation period (Figure 3.9). In the equilibration system, the final values of all the parameters are important to consider for further use. The simulation-derived densities and experimental densities exhibit good agreement.[204]

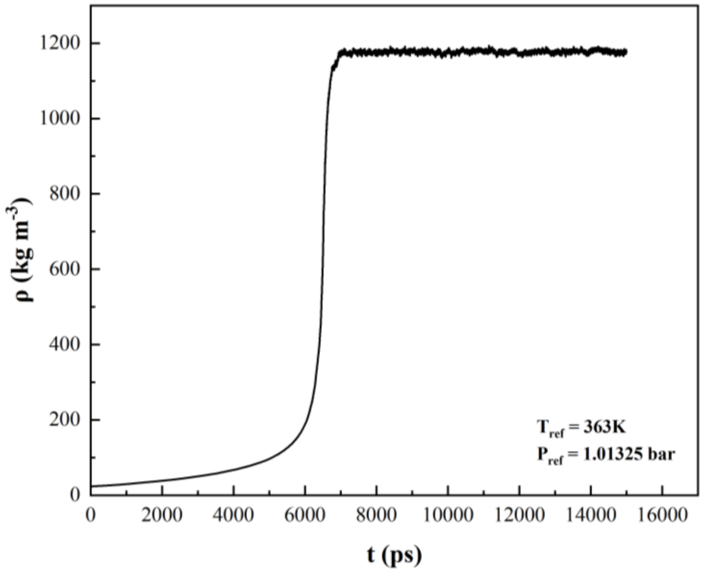

Figure 3.8: Density variation of PEO-LiTFSI system in NPT (MD) run.

3.4.5 Molecular Dynamics Production Run (MD)

In the long production run, a 150 to 250 ns long simulation is carried out under an NPT essemble to reach diffusive regimes because the analysis of ionic conductivity and transport properties of ions could only be valid if the SPE systems reach diffusive regimes and Li-ion needs a lengthy timescale to reach such diffusive regimes in the case of long polymer chain electrolyte systems. The final trajectories saved after the production run are used for further dynamic analysis. An equilibrated PEO/LiTFSI SPE is shown in Figure 3.10. A summary of all procedures (NVT, NPT, and MD) and the equilibration densities after the long MD production run is listed in Table 6 for all SPE systems (SPE1-SPE10) with varying salt concentration ratios.

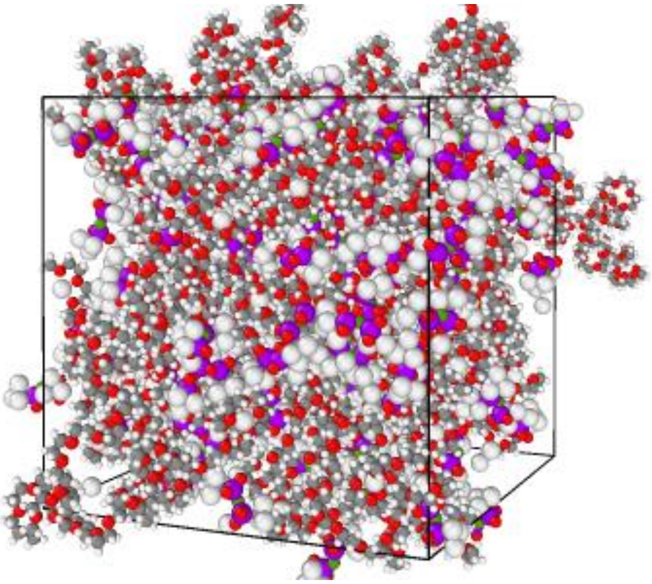

Figure 3.2: Snapshot of an equilibrated PEO-LiTFSI SPE system at 363 K with a concentration ratio of Li: EO = 0.12.

Table 6**.** Summary of the simulation setup and the average densities in each SPE system.

Model No.	**NVT run time (ps)**	**NPT run time (ns)**	**MD run time (ns)**	**Equilibrated Density (Kg/m^3)**
SPE1	50	15	150	1086.19
SPE2				1137.75
SPE3				1223.47
SPE4				1293.42
SPE5				1402.57
SPE6		20	200	1123.11
SPE7				1175.73
SPE8				1262.27
SPE9				1331.66
SPE10				1438.68

3.4.6 PEO/PVDF/LiTFSI System

The PVDF polymer chains are randomly dispersed in bulk PEO/LiTFSI matrix to prepare a BSPE system. The variation effect of salt concentration on ionic diffusion is also analyzed in the BSPE (PEO/PVDF/LiTFSI) system. The salt concentration ratios [Li: EO] = 0.02, 0.04, 0.08, 0.12, and 0.20 in BSPE are the same as in SPE. The number of particles in each PVDF-loaded system is shown in Table 6. To study the effect of changing the weight percentage of PVDF on the ionic conductivity of the BSPE system, a simulation setup is prepared by changing the weight percentage of PVDF in PEO/LiTFSI from 10, 20, 30, and 40 wt%. The initial density of the BSPE system is kept low to easily dissolve PVDF chains in the PEO/LiTFSI SPE and to avoid the potential energy trap caused by contact with PVDF chains and ions. The simulation setup and the equilibrated densities obtained after long MD runs in each PVDF-loaded BSPE system are shown in Table 7. The same simulation procedure (EM, NVT, NPT, and MD run) will also be repeated for the PEO/PVDF/LiTFSI electrolyte system at RT (298.15K).

Table 7. The total number of atoms for the PVDF-loaded BSPE system in this work.

No. of PEO chains	**No. of PVDF chains**	**Temperature (K)**	**[Li: EO]**	**Total No. of Molecules**	**Equilibrated Density (Kg/m^3)**
15	10	363	0.02	12182	1188.43
			0.04	12614	1227.29
			0.08	13478	1294.58
			0.12	14342	1349.15
			0.20	16070	1438.33

Table 8. Simulation setup for PVDF loaded BSPE system in this work.

No of PEO chains	[Li: EO]	Temperature (K)	PVDF Loading (wt%)	Total No. of Molecules	Equilibrated Density (Kg/m^3)
15	0.12	298.15	0	12162	1378.62
			10	13252	1405.46
			20	14778	1420.41
			30	16522	1435.23
			40	18920	1446.38

The trajectories after the final MD run are used to further calculate the mean square displacements (MSDs) of Li and TFSI ions in a diffusive regime. The calculated MSDs are used to find the ionic conductivity and Li-ions transference number. After studying the dynamic properties of PEO/LiTFSI and PEO/PVDF/LiTFSI electrolyte systems, a blended polymer/salt electrolyte system giving high RT ionic conductivity and transference number is selected for further research work.

3.4.7 PEO/PVDF/SN Plasticized Blended SPE System

To study the effect of adding plasticizer on the ionic conductivity and transport properties, the SN plasticizers are then dispersed randomly in bulk PEO/PVDF/LiTFSI SPE systems at different loadings of 5, 7.5, 10, 15, 20, and 25 wt% at RT (298.15K). The number of particles in each SN-loaded SPE system and simulated densities for each system are shown in Table 9.

Table 9. Simulation setup for each SN-loaded PBSPE system in this work.

No. of PEO chains	**No. of PVDF chains**	**[Li: EO]**	**Simulation Temperature (K)**	**SN loading wt%**	**Total number of atoms**	**Equilibrated Density (Kg/m^3)**
15	12	0.12	298.15	0	14778	1420.41
				5	15668	1390.53
				7.5	16138	1375.54
				10	16658	1361.57
				15	17738	1331.75
				20	18978	1302.34
				25	20378	1237.78

The initial density of the PBSPE system is kept low to easily dissolve SN molecules in the PEO/PVDF/LiTFSI SPE system and to avoid the potential energy trap caused by contact with SN molecules and other atoms. The same simulation procedure will also be repeated for PEO/PVDF/LiTFSI/SN electrolyte system at room temperature to see the effect of SN loading on the diffusion coefficients of Li and TFSI ions. The details of the simulation setup and equilibrated densities are given in Table 10. The trajectories after the final MD run are used to further calculate the MSDs of Li/TFSI ions in a diffusive regime. The calculated MSDs were used to find the ionic conductivity and Li-ion transference number. The effect of temperature on the density and dynamic properties of polymers and ions in the PBSPEs was also studied by repeating the simulation procedure for different temperatures.

Table 10. Simulation setup for SN-loaded PBSPE system at different temperatures.

No. of PEO chains	No. of PVDF chains	[Li: EO]	SN loading (wt%)	Temperature (K)	Equilibrated Density (Kg/m^3)
15	10	0.08	30	298.15	1302.34
				303.15	1297.31
				333.15	1263.62
				343.15	1252.48
				353.15	1241.8
				363.15	1231.08

3.5 Structural and Dynamic Properties of SPEs

3.5.1 Radial Distribution Function (RDF) and Coordination Number (CN)

Lithium coordination with other atoms of the molecules has been studied using the radial distribution function to better understand the local solvation environment of Li-ions in PEO polymer structures. RDF was also represented as g(r) and defined as the possibility of the presence of one particle at a radius r from another. The RDF is a crucial tool for describing the changes in structures that occurs because of microscopic interaction between different types of particles in the electrolyte systems. It can be computed using the following equation:

$$g(r) = \frac{dN}{\rho 4\pi r^2 dr} \tag{3.5}$$

In this Eq. (3.5), ρ is the density of the simulation system, and N is the number of particles present within r, the radial distance from one specified atom or molecule to another.

The CN is another method to study Li-ion interactions with other particles in the electrolyte systems. It can be calculated from the integration of their g(r) to the first minimum (r_{min}). Hence, only the first coordination shell has to be included. The general expression for CN can be represented as follows:

$$CN = 4\pi\rho\int_{r_o}^{r} g_r r^2 dr \tag{3.6}$$

3.5.2 Mean Square Displacement (MSD)

MSD is a specific tool that is used to track the particle (Li and TFSI ions) motion in the SPE systems and calculated by the following expression:

$$\mathrm{MSD} = \frac{1}{N}\sum_{i}^{N} d[r_i(t) - r_i(0)]^2 \tag{3.7}$$

where $r_i(t)$ shows the vector position of the particle *i* at time *t* and N is a total number of atoms.

3.5.3 Diffusion coefficient (D)

The D is also used to investigate the diffusion behavior of the ions and polymer chains in SPE. It can be calculated by using Einstein's relation using MSDs.

$$D = \frac{1}{6t}\left\{\frac{1}{N}\sum_{i}^{N} d[r_i(t) - r_i(0)]^2\right\} = \frac{MSD}{6t} \tag{3.8}$$

The MSDs for calculating diffusion coefficients are obtained from long trajectories ensuring that the particles have reached their diffusive regimes because Einstein's equation can be valid only in the diffusive regimes achieved at longer timescales (ideally $t \rightarrow \infty$).

3.5.4 Ionic conductivity (σ)

Ionic conductivity is another critical parameter to determine the performance and efficiency of an electrolyte to be used in the real-time application of a battery system. It can be calculated from the Nernst-Einstein equation, ensuring that the ionic motion is diffusive. The ionic conductivity (σ) is directly proportional to the diffusion coefficient of ions. Its general expression is represented as follows:

$$\sigma = \frac{nq^2D}{k_bT} \tag{3.9}$$

Where n is the number density of ions in m^{-3}, q is a charge on ion in C, D is the diffusion coefficient of ions in $m^2 s^{-1}$, k_b is the Boltzmann constant given as 1.38×10^{-23} J K^{-1}, and T is the temperature of the electrolyte system in K. Because of the dissociation of lithium salt into Li^+ and $TFSI^-$ ion, the above equation can be expressed as:

$$\sigma = \sigma^+ + \sigma^- \tag{3.10}$$

$$\sigma = \frac{q^2}{k_bT}(n^+D^+ + n^-D^-) \tag{3.11}$$

Where σ^+, n^+ and D^+ are the cationic conductivity, number density, and diffusion coefficient, and σ^-, n^- and D^- are the anionic conductivity, number density, and diffusion coefficient respectively.

3.5.5 Transference number (t^+)

The transference number defines the fraction of cation participation in the total ionic conductivity. Based on the self-diffusion coefficients of ions, the general expression for the lithium transference number is:

$$t^+ = \frac{D^+}{D^+ + D^-} \tag{3.12}$$

Where, D^+, and $D^-$are the cationic and anionic diffusion coefficients, respectively.

3.6 Summary

This chapter delves into the intricate molecular structures of materials and the techniques employed in creating a PBSPE for LIBs. Furthermore, a comprehensive explanation of the fundamental concepts and physical conditions requisite for conducting MD simulations of PBSPE, utilizing GROMACS software, is provided. Finally, an overview of the parameters essential for analyzing the structural and dynamic properties of an electrolyte system is presented.

Chapter 4. Results and Discussion

4.1 Computational Model Validation

4.1.1 Time Trajectory Analysis

MD calculation is performed on PEO/LiTFSI electrolytes to investigate how the molecular mass of polymers and lithium salt concentration variation affect the dynamic properties of the ions and polymers. Figure 4.1 shows the snapshots of simulation trajectories of the PEO/LiTFSI electrolyte cells taken during the equilibration procedure. These snapshots depict the interaction between PEO chains and LiTFSI salt in the simulation cells.

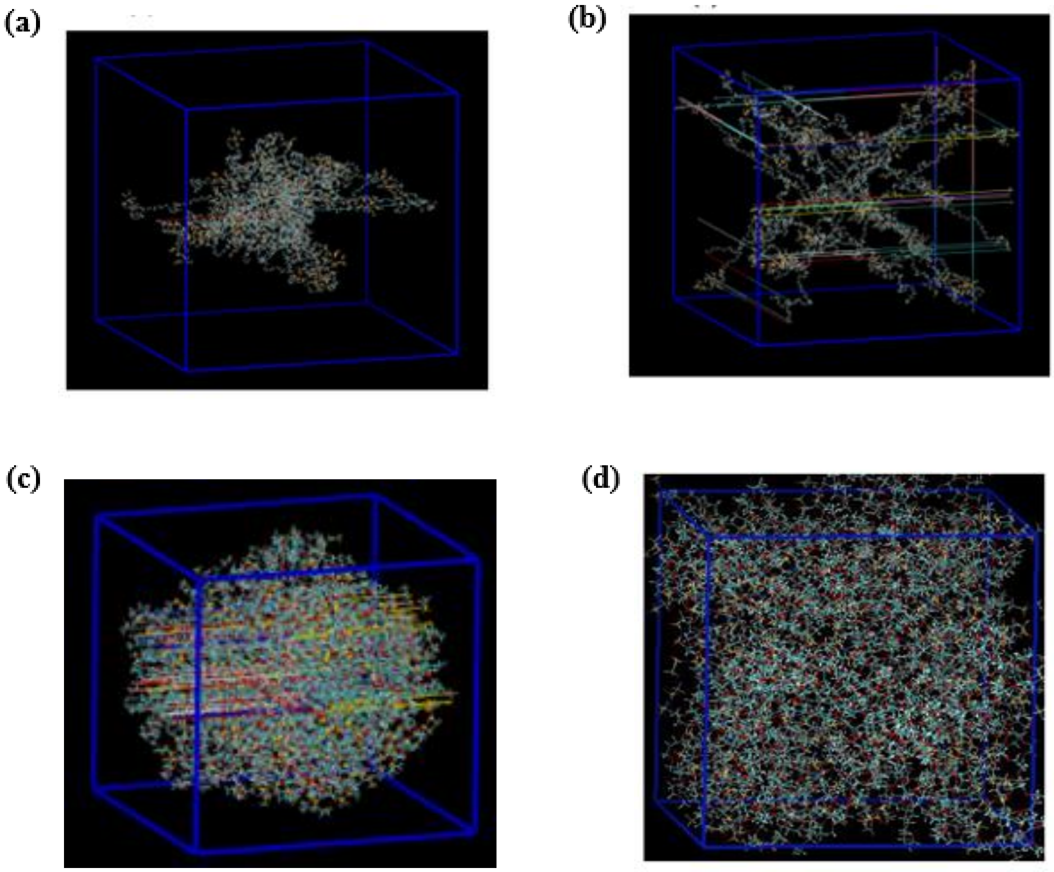

Figure 4.1: Conformations of the PEO-LiTFSI system in equilibration at different simulation times.

According to the data presented in Figure 4.1, it is apparent that during the process of NPT equilibration, the free volume of the simulation box decreases while the density increases. This results in a higher density of the polymer, which is in close agreement with experimental values.[205] Also, no breakage of the polymer chains has been observed from the visuals of the trajectories.

4.1.2 Density

To validate the force field and charge parameters, the comparisons with experimental values are presented for density over various salt concentration ranges. The validation procedure is completed in the following order to support the hypothesis. The density of pure PEO is calculated and compared with the values reported in the literature.[205, 206] Since no charge rescaling is applied for pure PEO, it can be utilized to study the dependence of densities on lithium salt concentration. After validation of the simulation setup, the densities of PEO-LiTFSI SPE are calculated and compared with experimental data in the literature. With a predicted density of 1075.75 kg m^{-3}, pure PEO with M_w~3965.4 g mol^{-1} agrees with the literature.[85, 166] The calculated densities of PEO-LiTFSI SPE at 363 K are shown in Figure 4.2a. A monotonic relationship between the densities and the salt concentrations can be observed, similar to the variation pattern described in the literature.[185] It shows how to calculate the charge scaling factor and validates the force field parameters for both polymer and lithium. There may be a marginal discrepancy in the density values obtained in this study compared to the reference simulation work. Such variation can be attributed to differences in the molecular mass of the polymer and the duration for which pressure ensembles are applied during the NPT run in the molecular dynamics simulation. The densities of PEO/PVDF are also computed for varying salt concentrations and compared with pure PEO/LiTFSI SPE, and the same conclusion can be obtained (shown in Figure 4.2b).

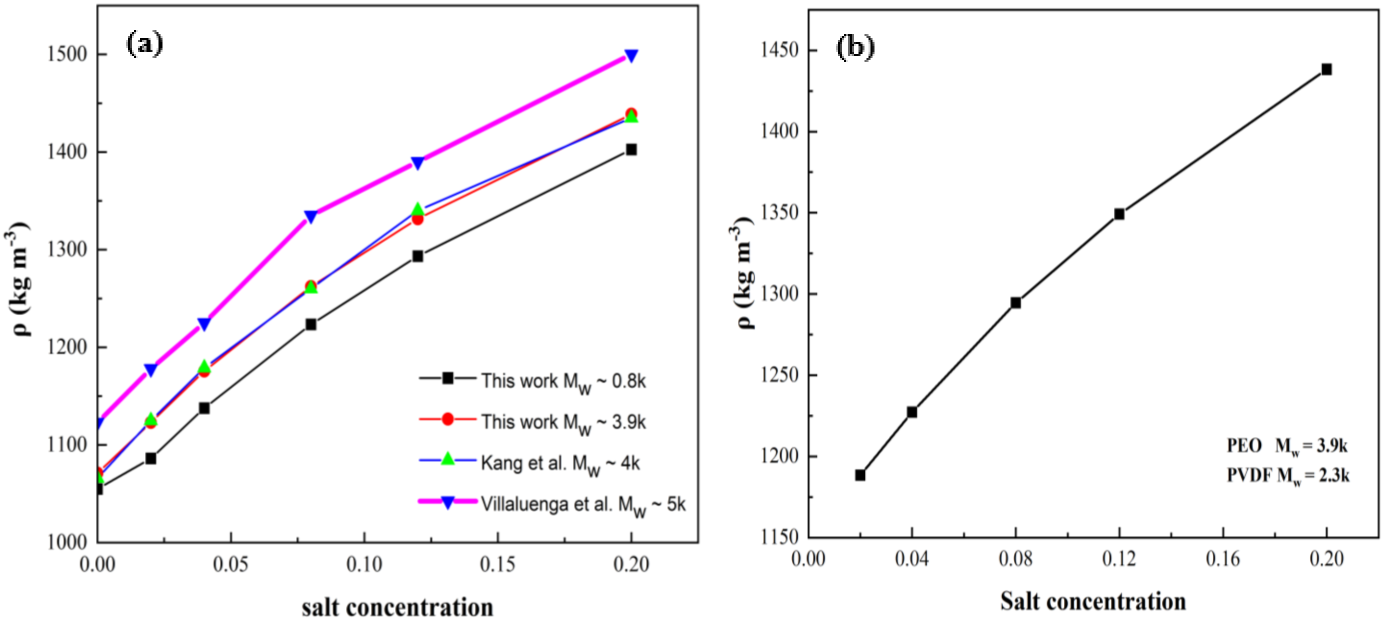

Figure 4.2: The density variation of (a) PEO-LiTFSI and, (b) PEVDF/LiTFSI electrolyte at 363 K

Similarly, the density variation of changing wt.% of SN and temperature of PBSPE are calculated with results shown in Figure 4.3. With the increase in mass percentage of SN and temperature of PBSPE, the density of the simulation box decreases. With the increase in the number of molecules and temperature, the energy of the atoms increases, and they vibrate with a large amplitude, applying large forces on each other. Also, with increasing SN particles, more molecules need a larger space to adjust in the simulation box. Hence, more volume will be required to accommodate all atoms with deficient potential energy, which decreases the density of the system.

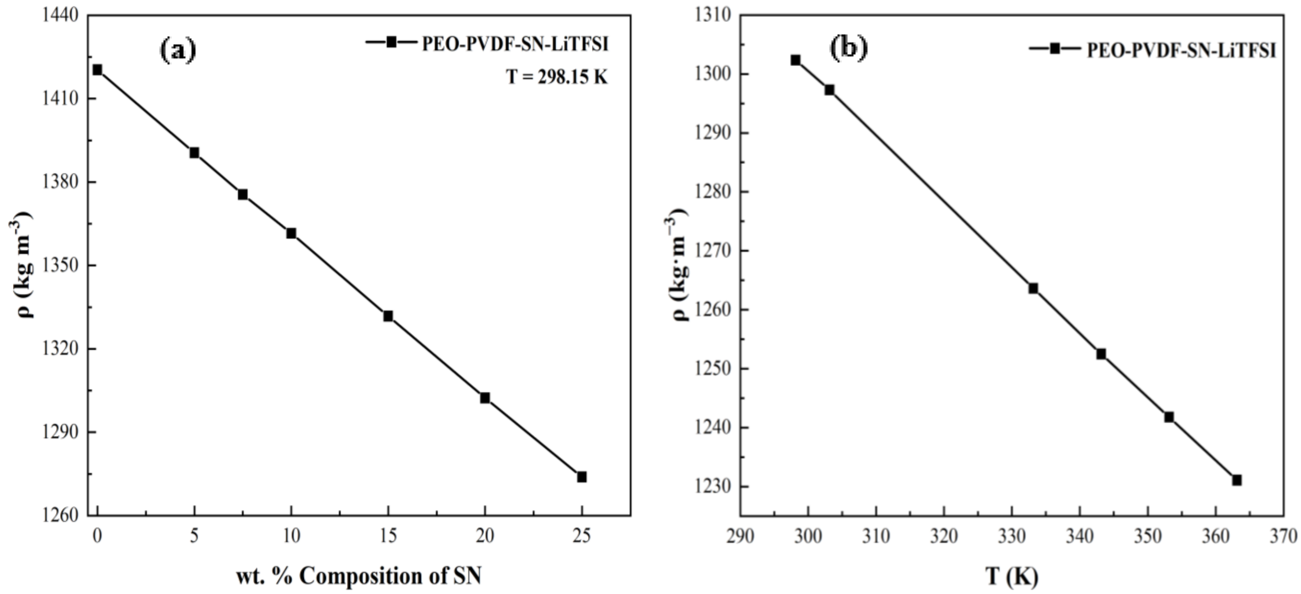

Figure 4.3: Density variation of PEO/PVDF/SN/LiTFSI electrolyte system (a) with varying wt% of SN, (b) increasing temperature.

4.1.3 Diffusion Coefficient and Ionic Conductivity

With varied salt concentrations, D^+ and D^- and ionic conductivity of SPE are calculated at 363 K (Figure 4.4), which agrees well with the reported IS experimental and simulation results in the literature.[101, 115, 207] The high values of D^+ and D^- and ionic conductivity for short-chain PEO (~M_w = 0.8 kg mol^{-1}) than for long-chain PEO (~M_w = 4 kg mol^{-1}) agree well with the description provided in the literature. The longer chains have lower segmental motion, while shorter chains are often more adaptable and allow ions to diffuse more along PEO chains resulting in higher diffusion coefficients.[208] The coordination of lithium ions with ether oxygen (O_{PEO}), which slows the mobility of the Li-ion carrying segments and, therefore, D^+, is the cause of the decreased Li-ion diffusion coefficient as compared to TFSI-ion. Meanwhile, the coordination of TFSI-ion with O_{PEO} is absent, allowing it to move freely.

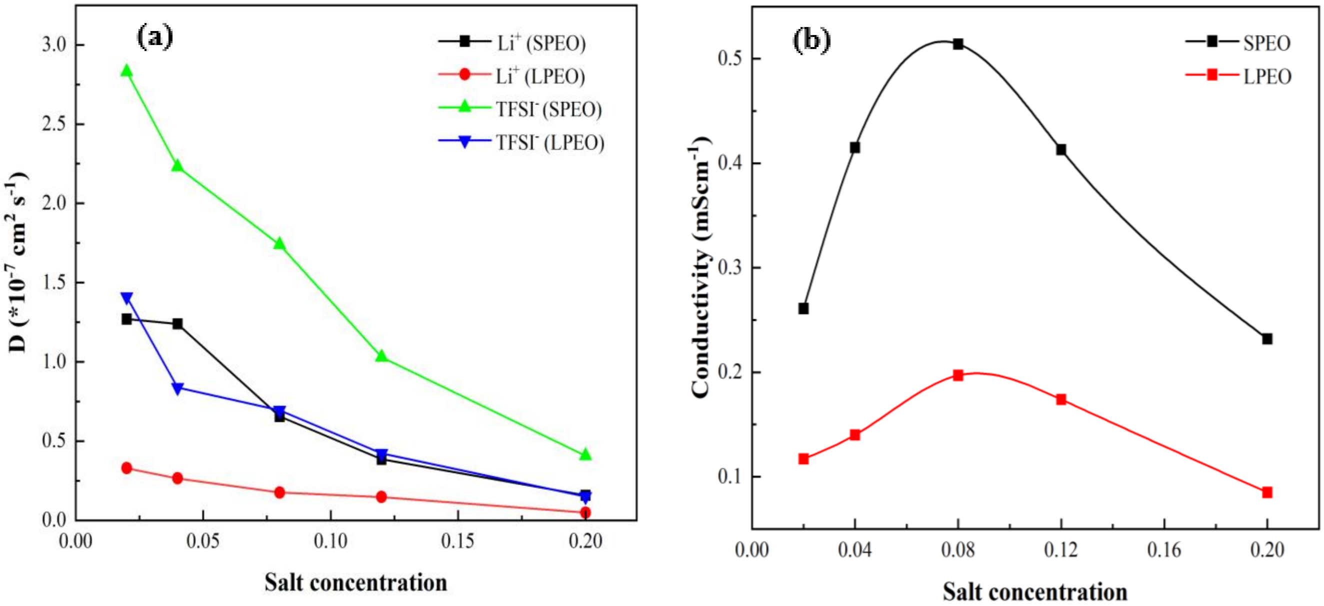

Figure 4.4: Variation of (a) Diffusion coefficients of Li^+ and $TFSI^-$, and (b) ionic conductivity of PEO/LiTFSI SPE with different M_w of PEO and salt concentration at 363K

Despite the lack of coordination for anion with PEO, D_{TFSI} decreases with increasing salt concentration after 0.08. This behavior of the anion is connected to the long-distance coupling between the anion and cation, forming Li^+-$TFSI^-$ aggregates. Having validated the MD simulation process and force field parameters through comparison with the simulated and experimental densities, diffusion coefficients, and ionic conductivity of ions in PEO/LiTFSI SPE systems with varying M_w of PEO and salt concentration, the structural and dynamics analysis of the Li-ion in PEO/PVDF/LiTFSI (BSPE) system and PEO/PVDF/SN/LiTFSI (PBSPE) system can now proceed.

4.2 Structural Properties

The visualization of the PEO/LiTFSI system shows that PEO's helical structure is still in an amorphous state even after long MD runs (Figure 4.5a). The increase in temperature and salt concentrations in PEO/LiTFSI SPEs do not decrease the contact between Li-ion and O_{PEO} atoms.

Initially, the RDF and CN for pure PEO/LiTFSI SPE are computed. In the PEO/LiTFSI electrolyte, the radial distribution function and coordination number at salt concentration ratio [Li: EO] = 0.12 are shown in Figure 4.5b. The Li-ion local coordination environment and Li- O_{PEO} RDF observed for PEO-LiTFSI in this work are well-aligned with that obtained through experiments[209] and calculated by simulation available in the literature.[203] The 0.212 nm peak of the initial coordination agrees with the 0.21 nm peak seen in a neutron scattering analysis.[210, 211]

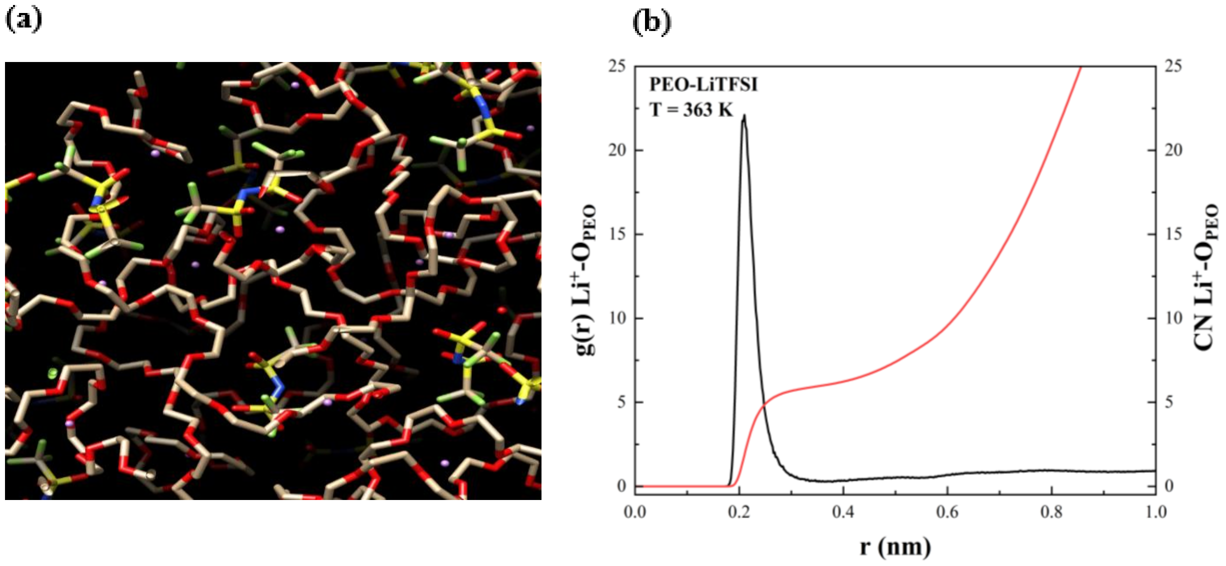

Figure 4.5: (a) Helical structure of PEO after long MD runs, and (b) RDF and CN at [Li: EO] = 0.12.

It shows the bonding between Li-O_{PEO}. Depending on the integral distance cutoff setting, the CN ranges from 4.9 to 6, as per the expected results of experiments.[209, 212] Figure 4.6 illustrates a Li-site in a long chain PEO (N = 90) with a salt concentration of [Li: EO] = 0.12. One O_{PEO} atom coordinated with Li-ion at a distance of 1.901 Å. The other two polymer O_{PEO} atoms lie at Li-O interatomic lengths ~of 2.1 Å and a fifth O_{PEO} atom at ~2.391 Å. The Li location reflects an intra-atomic segmental motion if the O_{PEO} atoms are part of a single polymer chain.

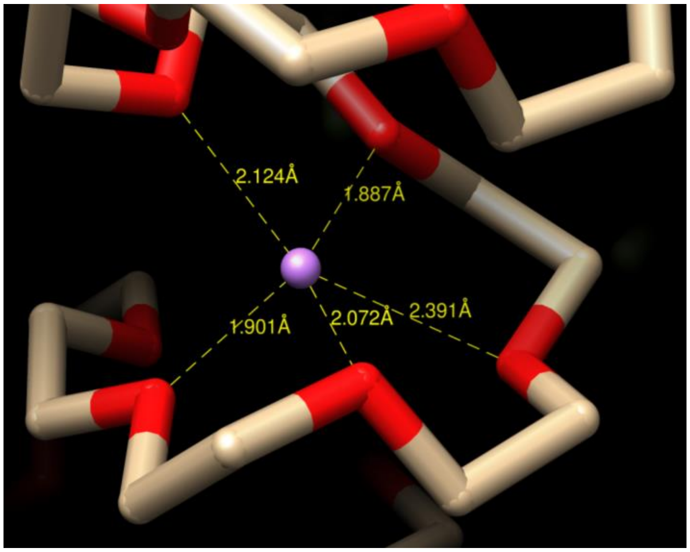

Figure 4.6: Li-ion coordination with O_{PEO} in the PEO/LiTFSI system

The essential interaction between Li^+ and oxygen atoms within the ionic solvation sheath structure was examined using the Radial Distribution Function (RDF). For all concentration ratios, the first peak of RDF at ~2.1 Å explains the strong association between Li-O_{PEO} and verifies the simulation procedure developed in this work. The peak height at ~2.1 Å shows the density of Li^+ in the first solvation shell from the ether oxygen (Figure 4.7a). The small changes in the first peak height for different salt concentrations correspond to the small changes in the number of coordinated oxygens around Li^+. A second small peak at r ~6 Å was also observed, which corresponds to the small coordination of Li^+ and oxygen molecules from the $TFSI^-$ anion to form static ion clusters.[204] Figure 4.7b) depicts the RDF between the Li^+ and $TFSI^-$ ions in PEO/LiTFSI SPE. For lower salt concentrations, the initial minimum was discovered to be at ~10 Å; this value served as the cutoff point for detecting if LiTFSI is dissociated. The minor peaks detected below 6 Å are similar to that observed in the structure of P(EO)-LiTFSI indicating the fewer interactions between Li^+ and $TFSI^-$ ions in the low salt concentration SPE system.[212] This implies that both Li^+ and $TFSI^-$ ions are well dissociated and free to migrate.

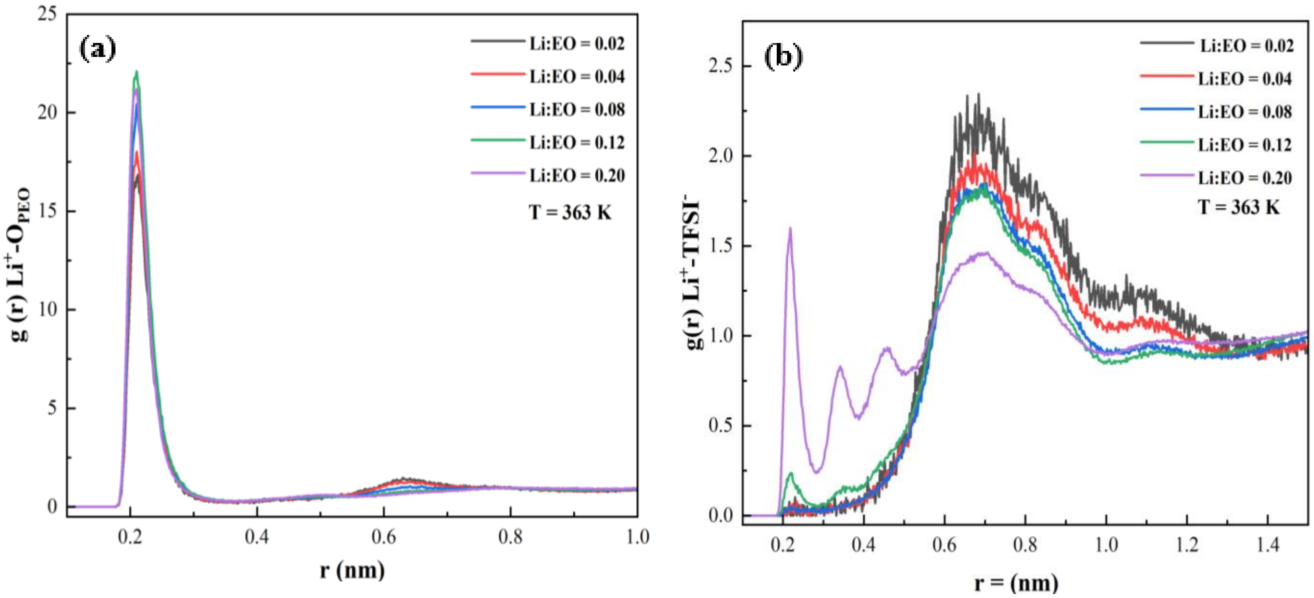

Figure 4.7: (a) Li-O_{PEO} coordination and (b) Li-TFSI coordination for PEO/LiTFSI with different salt concentrations.

This is consistent with the observation in the MD simulation by Zheng et al.[213] At higher salt concentrations (0.20 in this work), the tetra-modal Li-O_{TFSI} peaks (at ~2.3 Å, ~3.5 Å, ~4.5 Å and ~7 Å) appeared, which corresponded to the change in the structure of ion clusters and the presence of Li^+ interactions with different atoms of $TFSI^-$. The g(r) peak at ~2.3 Å explains that there direct coordination of Li^+ with oxygen atoms in the $TFSI^–$ anion. Whereas the appearance of two peaks at ~4.5 Å and ~3.5 Å in the g(r) of Li^+-$TFSI^-$ explains the possible Li^+ interaction with nitrogen atoms in $TFSI^–$ in both a bidentate and a monodentate manner or slightly more extended Li^+-O coordination environments. Because, TFSI-anion has extensive charge delocalization (i.e., multiple resonance structures). The anion is flexible and can adopt a configuration in which its nitrogen atom faces away from the lithium center or towards the lithium center.[214] A bidentate arrangement is one in which the nitrogen atom is consequently located nearer to a different lithium center. The above g(r) peaks show the possibility of finding the nitrogen atom pointing away from one lithium center, verifying the bidentate arrangement. The g(r) peak at ~0.7 is likely an indicative of the second coordination shell or more distant solvation environment around the Li^+ ions. It reflects interactions involving Li^+ ions and $TFSI^-$ anions that are not directly coordinated but are part of the structured ionic network in the polymer. It can also represent the spatial arrangement of multiple $TFSI^-$ anions and Li^+ ions within the polymer matrix, showing the organization of the ions beyond the immediate coordination sphere. The Li-ion solvation shell deduced from MD simulation in this work also agrees well with DFT computations in the literature.[204]

The distribution of CNs for Li-ion with the O_{PEO} is shown in Figure 4.8. CN is the number of nearest atoms that a central atom holds and can be calculated as a function of distance by integrating the g(r) up to its first minimum. The CN will be 0 at a lower distance (r < 2 Å) because no molecules can come closer to the diameter or VdW radii of the reference molecule, i.e., g(r) = 0 when $r<\sigma$ (σ is molecular diameter). The interaction between particles is repulsive for small distances.

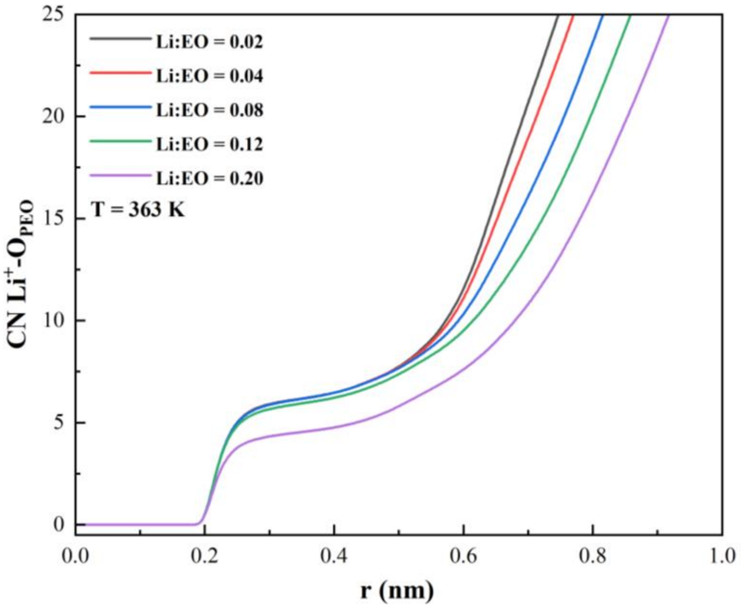

Figure 4.8: Oxygen coordination rate of Li ions.

If particles strongly repel each other at very short distances, they cannot get too close, and the CN will be zero. At this distance, there will be no interaction between Li^+ and the oxygen atom of PEO. At r = 2 - 3 Å, the Li^+ atom directly coordinates with the oxygen (sum of radii of Li^+ and an oxygen atom) in the first solvation shell and shows the sharp peak at this distance. At a distance (3 Å < r < 5.5 Å), the Li^+ atom weakly coordinated with the oxygen atom because the average no. of Li^+ in the second and third solvation shells is fewer because of the weakening of electrostatic interaction. Therefore, the peak did not show any remarkable increase. Further, with an increase in distance (r > 5.5 Å), the oxygen present in the bulk will be counted as coordinated with Li^+, and the coordination number increases rapidly. These results also relate to the one explained by RDFs. The decrease in CN at high salt concentrations resulted from static clustering. As a result of the preceding discussion, all systems may be divided into two distinct regions with a limit of [Li: EO] = 0.12, which has different ionic interactions. The quantity and size of Li^+ and $TFSI^-$ ion clusters substantially impact the transport properties of Li ions.[215] LiTFSI is defined as a cluster with a distance of 5 Å or less between Li and TFSI ions.[185] The size of LiTFSI clusters is defined by the number of Li^+ or $TFSI^-$ within the defined distance. The quantity of Li^+ or $TFSI^-$ ions contained within the specified distance determines the size of LiTFSI clusters. Two oxygen atoms of the same TFSI-ion are seen to coordinate with the Li-ion to form a cluster of size one (Figure 4.9a). In Figure 4.9b, nine oxygen atoms of three different TFSI-ion coordinate with Li-ion to form a cluster of size three. Six oxygen atoms from three different TFSI-ions coordinated with Li-ions with a distance of ~2.1, one oxygen at ~3 Å, and two oxygen atoms show coordination at ~4.2 Å distance. This is also clear from a small g(r) peak of Li-TFSI at a distance of ~2.2 Å following a rise of the coordination line at around ~3 Å and ~4 Å after the first minimum (Figure 4.7b).

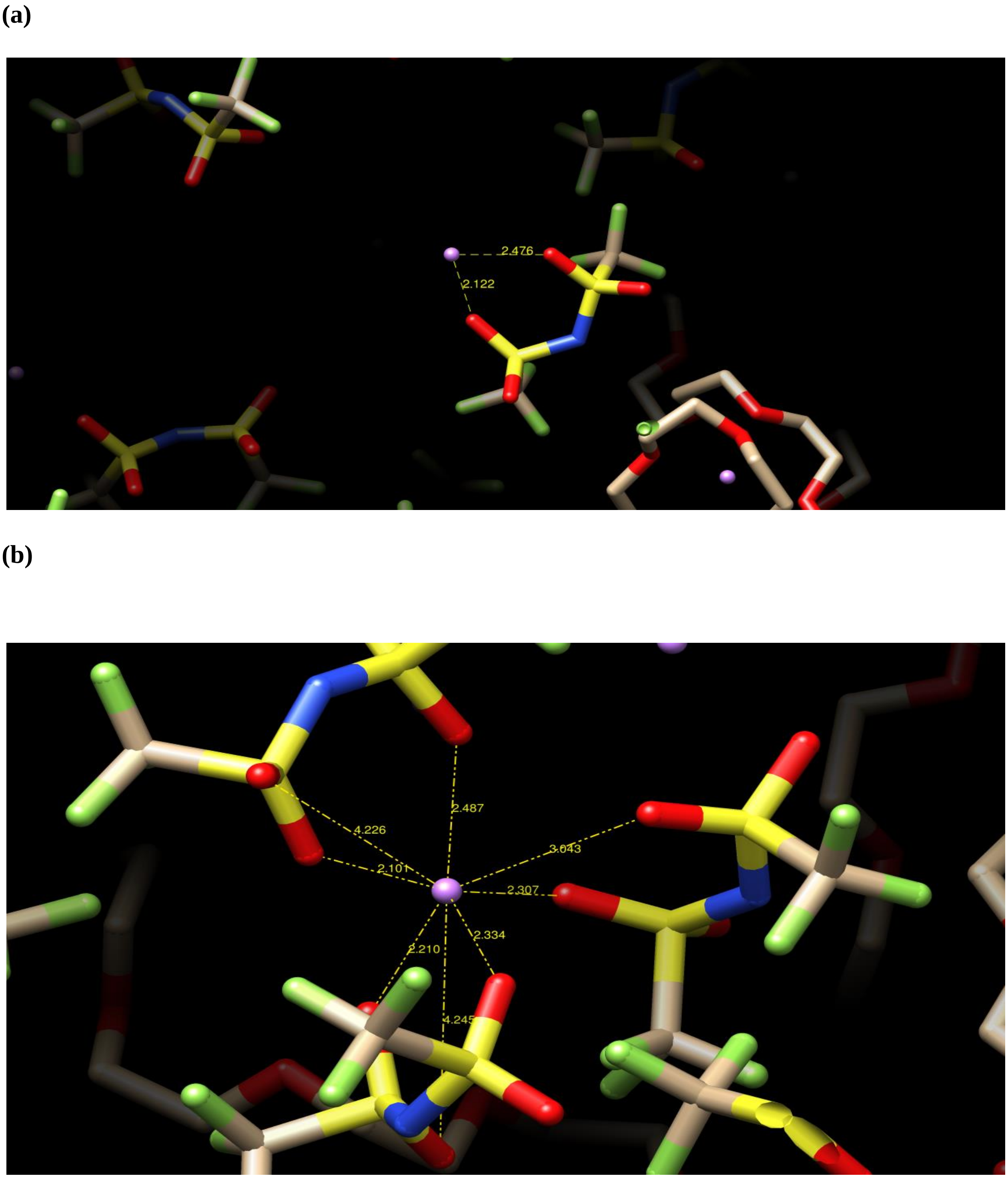

Figure 4.9: Clusters of Li and TFSI ions in PEO/LiTFSI at a concentration ratio [Li: EO] = 0.20.

The ion-ion contact and subsequent ion association are directly impacted by the change in salt content. To attain a better comprehension of interactions, different properties of SPE are examined at varying concentrations of salt. The Li-O_{all} RDFs are first calculated with lithium ions as the reference particles and all of the oxygen atoms as the observed particles. All representatives Li-O_{all}, Li-$O_{PEO,}$ and Li-O_{TFSI} RDFs at [Li: EO] = 0.02, 0.04, 0.08, 0.12, and 0.20 are shown in Figure 4.10. Li-O_{PEO} RDF is similar to that of the Li-O_{all}, which indicates that Li-ions are primarily attached to the O_{PEO}. The flat curve for Li-O_{TFSI} at around r ~2.3 Å for salt concentrations 0.02-0.08 shows no ion-ion interactions. This means LiTFSI salts are well dissociated.

Moreover, a difference in the peak height for Li-O_{all} and Li-O_{PEO} and an increase in Li-O_{TFSI} has been observed as salt concentration (> 0.08) increases because of more interactions in Li-TFSI in concentrated SSEs. This behavior of Li-O_{all} also supports the concept of cluster formation at higher salt concentrations.[175] Regarding ASSPEs, ion transport is primarily a function of the amorphous area above the T_g, whereas the ionic conductivity in the crystal region is minimal. The ion conduction mechanism for polymers like PEO and PAN has been fairly well understood. In which lithium ions travel by coordinating with ether oxygens of polymer chains.

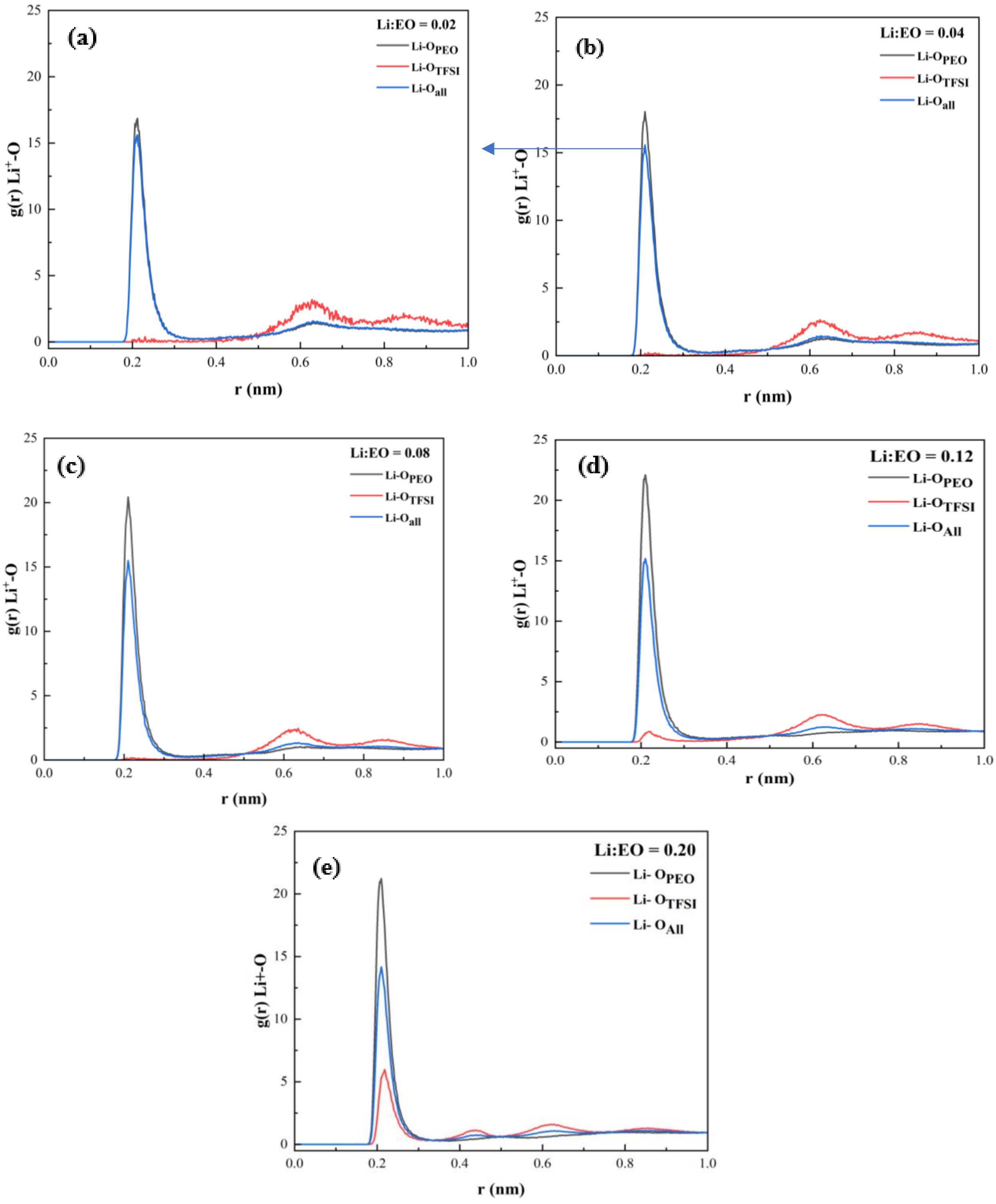

Figure 4.10: Representative RDF for Li-O coordination with O$_{PEO}$, O$_{TFSI}$, and O$_{all}$ at different salt concentrations

However, PVDF does not have any coordinating group along its chain that interacts with the lithium ions and helps lithium ions move from one place to the next. In this case, the lithium ions could hop from one TFSI-stabilized site to the next as the salt clusters create a percolating network (Figure 4.11).[216] The green dashed arrows point toward Li-ions, while the blue dotted arrows suggest a TFSI-ions potential mobility when local relaxation is present.

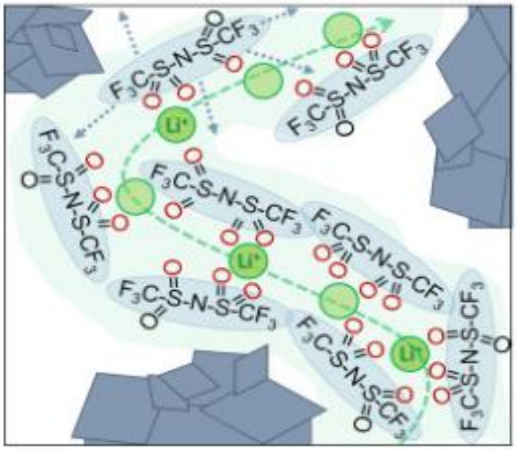

Figure 4.11: Mechanism of the Li and TFSI ions transport path, Reproduced with permission from Ref. [216] copyright © 2022, Journal of Energy Chemistry

The RDFs between Li-ion, O_{PEO}, and TFSI-ion are calculated to study the effect of PVDF addition in SPE shown in (Figure 4.12). Figure 4.12a shows that the strong Li^+-O_{PEO} coordination causes a sudden rise in the peak of g(r) for 20 wt.% as compared to 10 wt.%. Further addition of PVDF leads to g(r) increases smoothly with the highest peak observed at 40 wt.% of PVDF. Moreover, the highest peak of g(r) for Li^+-$TFSI^-$ was also observed when 40 wt.% PVDF were added (Figure 4.12b). This shows that there is a strong connection present between Li^+- $O_{PEO,}$ and Li^+-$TFSI^-$ at this concentration of PVDF in BSPE, creating more transport channels for lithium-ions to diffuse into BSPE.

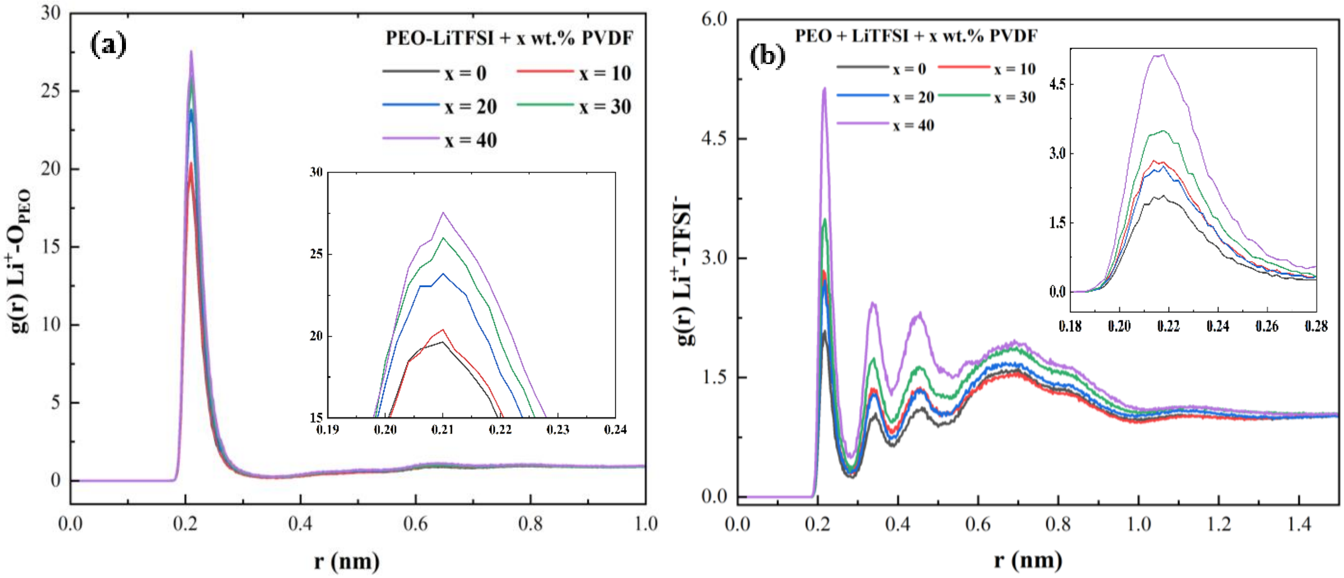

Figure 4.12: Representative RDFs between (a) Li^+ and O atoms in PEO and (b) Li^+ and $TFSI^-$ in BSPE systems.

A similar trend to the g(r) (tetra-modal $\text{Li-O}_{\text{TFSI}}$ peaks at ~2.3 Å, ~3.5 Å, ~4.5 Å and ~7 Å) of lithium-ion ($\text{Li-O}_{\text{TFSI}}$) were seen in Figure 4.12b as in higher salt concentrations. Which corresponded to the change in the structure of ion clusters and the presence of Li^+ interactions with different atoms of $TFSI^-$. The increasing height of g(r) as wt.% of PVDF in PEO-LiTFSI increases explains the strong ion-ion interaction in the form of moving clusters. Figure 4.13a shows the MSD behavior of Li^+ and $TFSI^-$ in BSPE. MSD can undergo different regimes (ballistic, sub-diffusion, Einstein diffusion). The equation of diffusion coefficient could only be applied to the linear diffusive regime of the MSD curve. The diffusion behavior may deviate from a simple MSD = 6Dt expression in nonlinear regions. Specifically, the exponent of t can change, causing small errors in the values of D. Figure 4.13a shows that the MSD of Li-ion batteries rises in all systems as simulation time goes on. The rate of increase in MSD and diffusion coefficient of Li^+ is less when

30 wt.% PVDF is added in comparison to 20 wt.% and 40 wt.%, which shows that lithium-ion diffuses at a slower rate at 30 wt.% of PVDF.

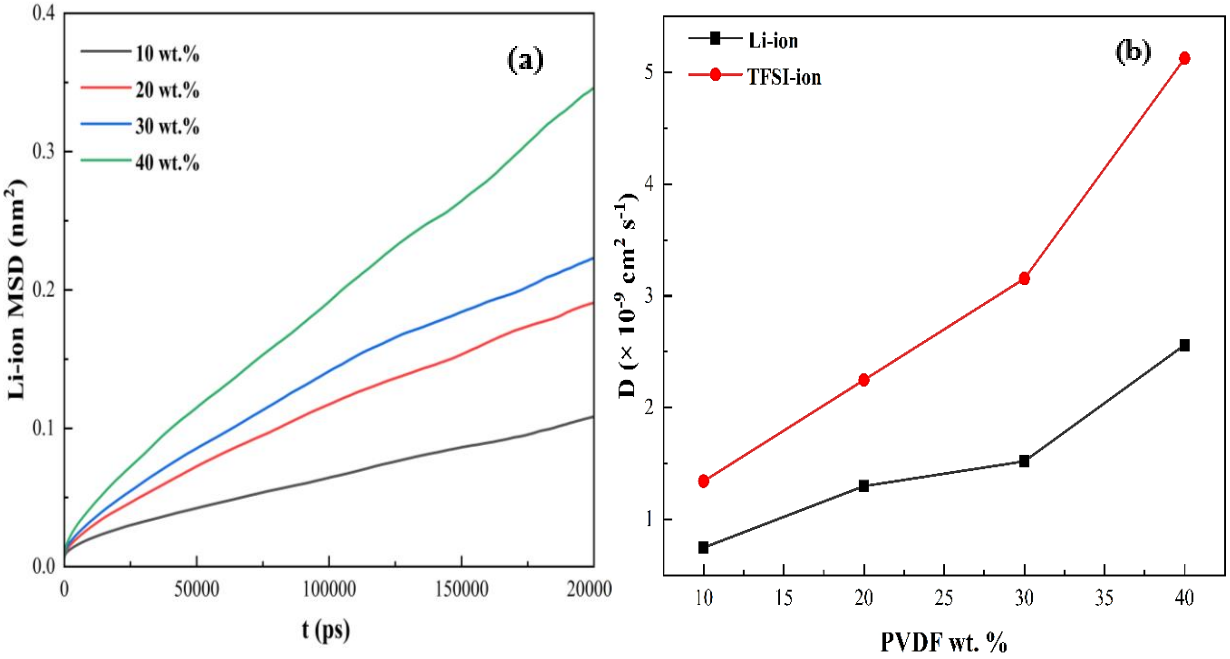

Figure 4.13: (a) MSD of Li-ion, and (b) Diffusion coefficients of Li and TFSI$^-$ in BSPE systems.

This behavior of lithium-ion is also clear from Figure 4.13b, from which we can see a low increase in D of lithium-ion in comparison with the D at other weight percentages. The movement of lithium ions can slow down due to changes in the polymer matrix's structure and characteristics. At specific weight percentages, the interface between PEO and PVDF could change, influencing the interactions between the polymers and the lithium ions. The change in lithium ion-conducting pathways might initially hinder ion diffusion but, upon reaching an optimized concentration, could facilitate better ion transport.[169, 217] The effect of wt.% of PVDF on Li-ion conductivity is studied for lithium salt concentration ratio [Li: EO] = 0.12 (Figure 4.14) in BSPE.

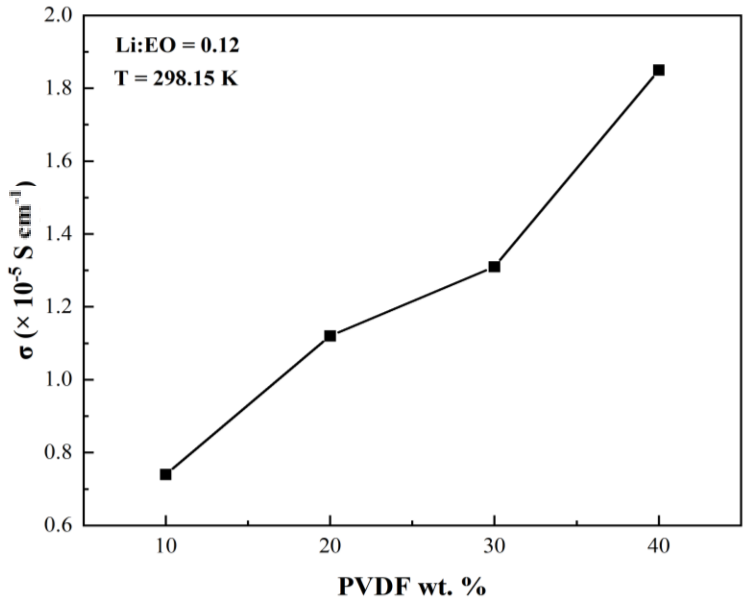

Figure 4.14: Ionic conductivity with varying wt.% of PVDF in PEO/LiTFSI SPE.

The linear increasing trend was observed for lithium ionic conductivity with the addition of PVDF in BSPE, with a small discrepancy observed when 30 wt.%. The decrease in ionic conductivity at 30 wt.% of PVDF is related to a decrease in diffusion of lithium-ion at this weight percentage. Because ionic conductivity is directly related to the diffusion of ions through the Nernst-Einstein relation. The Nernst-Einstein relation suggests that if the ions in SPE are completely uncorrelated, the ionic conductivity of polymer electrolyte increases correspondingly with diffusion coefficients of anion and cation and vice versa. Thus, a decrease in lithium-ion diffusion caused a deviation from the expected linear trend in the increase of ionic conductivity at 30 wt.% of PVDF in BSPE.

Figure 4.15a shows the RDFs of Li^+-O_{PEO} in PBSPE with varying wt.% of SN in BSPE. Li^+-O_{PEO} exhibits a strong peak at a wavelength of about r ~2.3 Å, consistent with the literature.[135, 156] The highest peak of Li^+-O_{PEO} can be obtained when the mass fraction of SN is at 25 wt%, whereas the Li$^+$-O$_{TFSI}$ peak is at its lowest. This shows that increasing SN wt.% helps in LiTFSI salt dissociation increases, causing the ions to move freely.

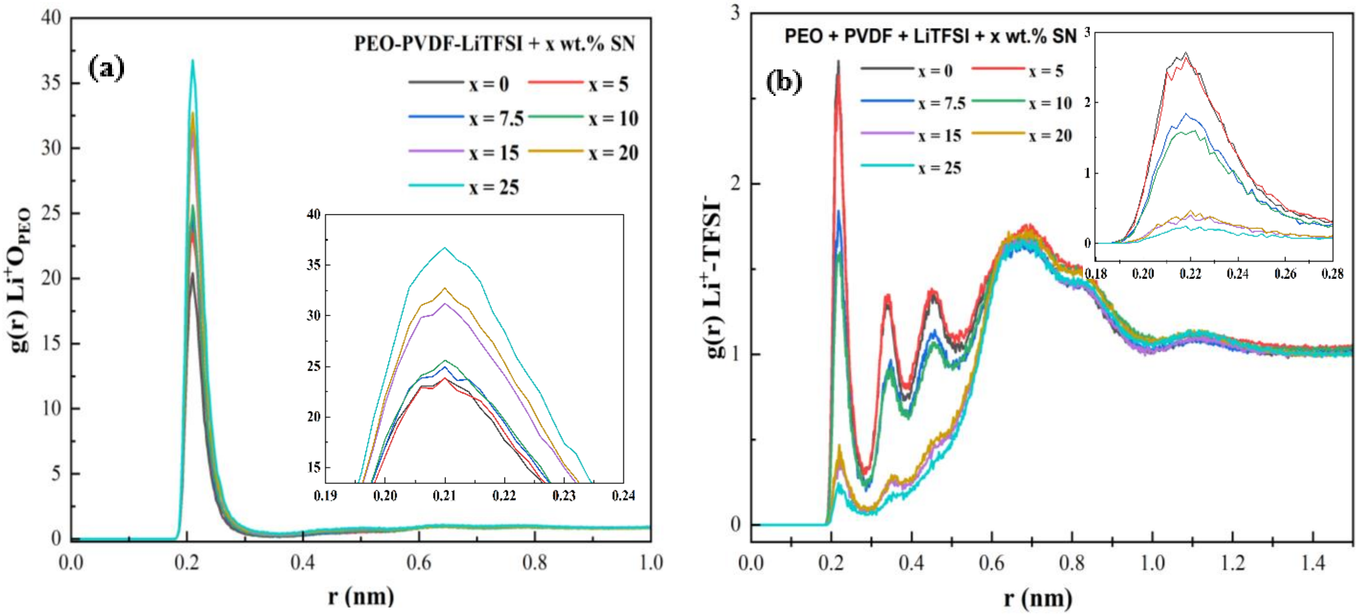

Figure 4.15: Representative RDFs between (a) Li$^+$ and O atoms in PEO and (b) Li$^+$ and TFSI$^-$ in PBSPE systems.

The trend for g(r) of Li$^+$-TFSI$^-$ is shown in Figure 4.15b which is similar to the variation trend of Li$^+$-TFSI$^-$ in higher salt concentrations of the SPE system. Four peaks were observed at lower SN weight percentages at a distance of ~2 Å, ~3.5 Å, ~4.5 Å and ~7 Å corresponding to lithium ion coordination with O$_{PEO}$, N$_{TFSI}$, and O$_{TFSI}$. As wt.% of SN increases the peaks at a distance of ~3.5 Å, ~4.5 Å, and ~7 Å starts to disappear showing that increasing SN wt.% helps to dissociate LiTFSI salt. The small peak at ~2 A shows that lithium ions are still coordinated with ether oxygen causing the lithium ions to hop along the PEO chain.

Figure 4.16a shows the RDF of Li$^+$-SN in PBSPE. As the wt.% of SN increases, the excess SN molecules are coordinated to the Li-ion. The SN molecules fluctuated between the trans and gauche conformations, giving three different peaks at r ~2.2 Å and ~3 Å with the following broad peak at ~5 Å. The large peak at ~2.2 Å likely corresponds to the direct coordination of Li^+ ions with the nitrogen atoms in the cyano groups (-C≡N) of succinonitrile. Succinonitrile has two nitrile groups, and the lone pairs of electrons on the nitrogen atoms are highly electronegative and can strongly coordinate with Li^+ ions. The distance of 0.2 nm is typical for strong ionic or coordinative interactions between Li^+ and nitrogen atoms. A small peak at 0.3 Å could represent either a slightly more extended interaction within the first coordination shell or a second coordination interaction involving the polymer chains (PEO/PVDF) or the oxygen atoms of the PEO matrix.

The small broad peaks of g(r) for $TFSI^-$ -SN in Figure 4.16b show that the SN molecule does not directly coordinate with the $TFSI^-$ anion. Because of the presence of highly negative nitrogen atoms, SN is anticipated to interact strongly with Li-ions.[182] The large peak of g(r) at a distance ~2.2 Å shows that the strong interaction of Li-ions with O_{PEO} outweighs the SN-Li^+ coordination, letting SN effect more strongly towards the TFSI-ions, thus helping to separate the ions from their counterions.

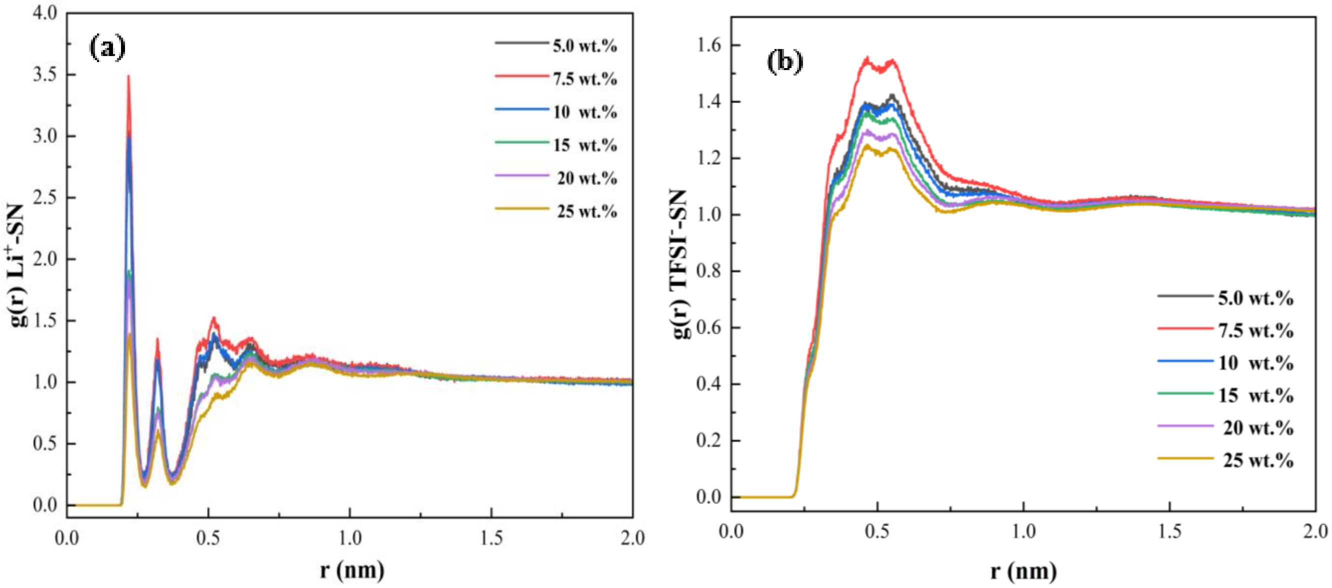

Figure 4.16: Representative RDFs between (a) Li^+ and SN and (b) $TFSI^-$ and SN in PBSPE systems.

The CNs of Li around SN (Li^+-SN), SN around Li (SN-Li^+), TFSI around SN ($TFSI^-$-SN), and SN around TFSI (SN-$TFSI^-$) are given in Figure. 4.17. Two peaks at around r ~2.5 Å and r ~3.5 Å for corresponding coordination numbers for Li^+-SN shown in Figures 4.17(a and b) reflect the coordination of Li^+ with SN in the first and second coordination shells. The rapid increase in CN of TFSI around SN is because the SN present in the bulk will be counted as coordinated with $TFSI^-$ in PBSPE systems. It can be seen in Figure 4.17(c and d) that increasing the wt.% of SN, the coordination of SN around TFSI anion increases but not around Li-ions. This indicates that SN affects more to the TFSI$^-$ helping in separating the ion pair. As a result, ionic mobility and conductivity increase.

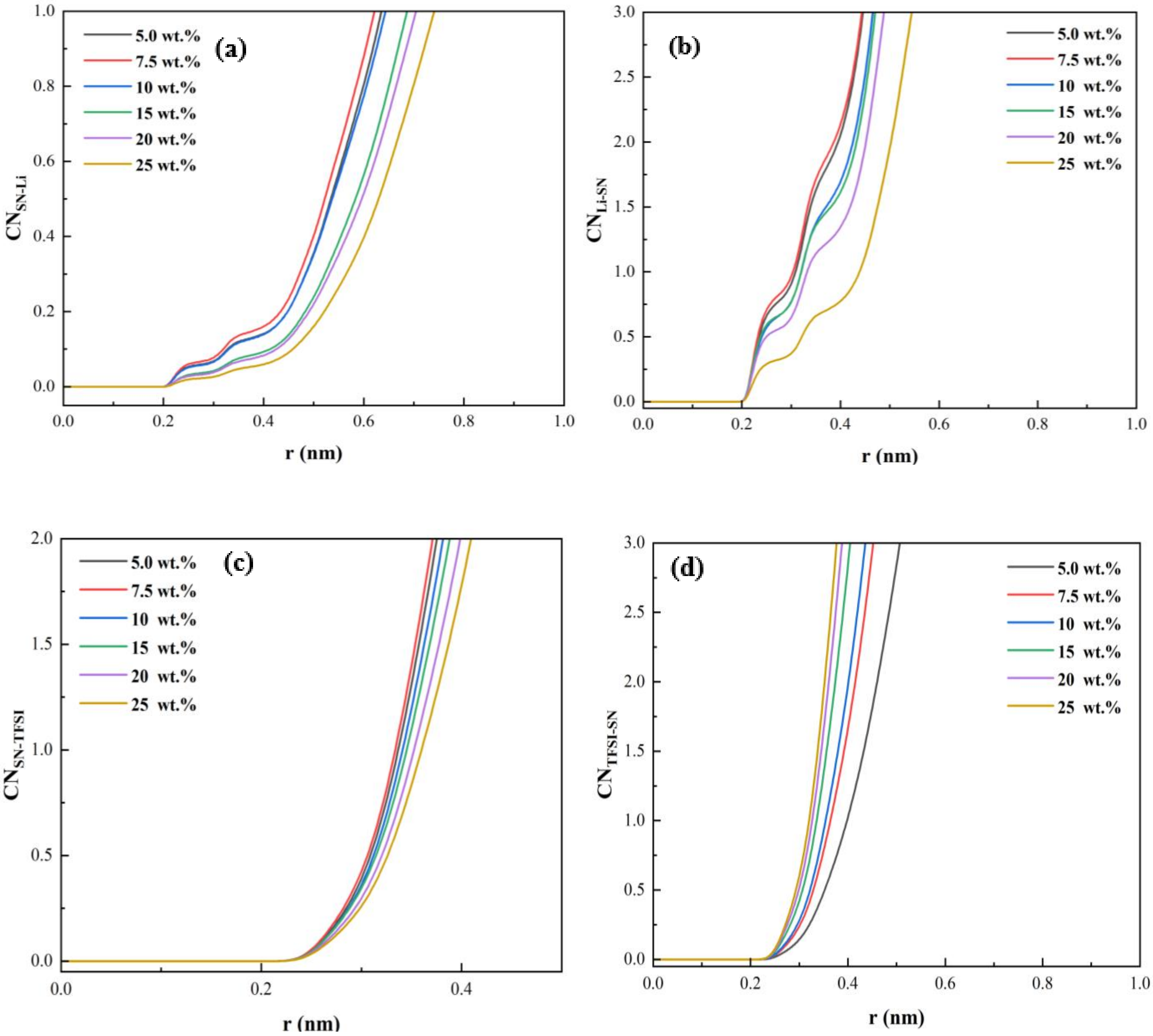

Figure 4.17: CNs of (a) Li around SN (Li$^+$-SN), (b) SN around Li (SN-Li$^+$), (c) TFSI around SN (TFSI$^-$-SN), and (d) SN around TFSI (SN-TFSI$^-$) in PBSPE systems

4.3 Dynamics Properties

Figure 4.18 shows the MSD-t relationship of Li-ion and TFSI-ion over a range of [Li: EO]= 0.02 to 0.20 at 363 K in PEO/LiTFSI SPE. The increasing MSD of both ions with the simulation time shows that they diffuse more in the SPE system, which agrees well with the results reported in the literature.[204, 218, 219] However, with increasing salt concentrations, the rate of MSDs decreases. Because more salt has been mixed with the polymer matrix, there are fewer available sites for ions to move freely. The shape of the MSD plot depends on the diffusion regime in which the particle is at that moment. Lithium-ion can be in sub-diffusive (given by the cure) or diffusive (linear) regions throughout its journey.

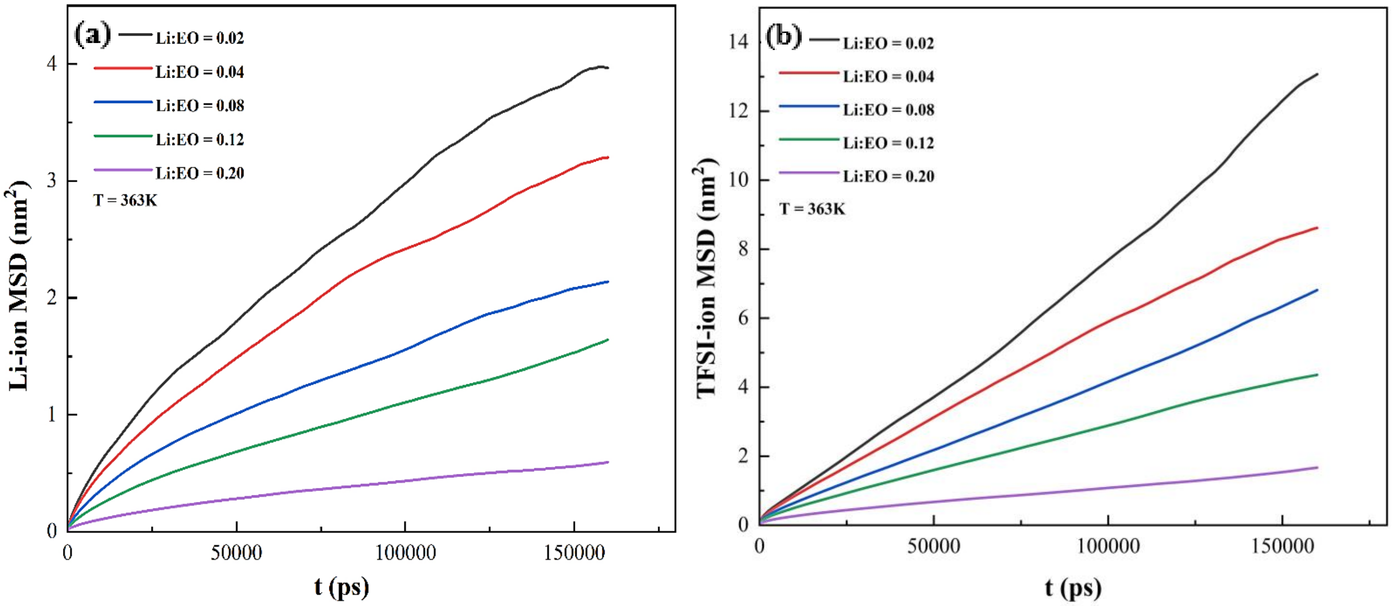

Figure 4.18: MSD-t relation of a) Li-ion and b) TFSI-ion with varying salt concentration at T = 363k.

The GROMACS code computes the MSD of atoms from a set of initial positions. The non-linear regions of the MSD curve at the beginning and end are the result of how the calculation is done by the GROMACS code. MSD accuracy decreases as a function of the lag-time t because for large t there are fewer pairs of time slices of interval t to average over, thus giving an irregular behavior of MSD at the start and end of the simulation (at around 150000-200000 ps). Similar curves can also be seen in the literature.[220] According to the MSD results shown in Figure 4.18, the motion of the TFSI-ions transforms from the subdiffusive to the diffusive zone at the beginning of the simulation time (0-50 ps). However, the Li-ion maintains a subdiffusive state for a substantially longer timescale (0-50 ns).

This explains that the anion ($TFSI^-$) diffuses more quickly than the cation (Li^+). The outcome is adequately explained by the substantially stronger connection of Li-ions with the oxygen atoms of the PEO polymer as compared to the TFSI anions interaction. The literature also noted the same pattern for both Li and TFSI ions.[203, 221-225] Fickian diffusion refers to the diffusion process characterized by a linear relationship between the square root of time and the distance traveled by the diffusing species. In this regime, the movement of particles is governed by Brownian motion, where particles move randomly due to thermal energy, resulting in a gradual spreading of the diffusing species. To find the Fickian diffusive regime,[203] the ln-ln slope for the MSD-t graph is plotted. It is a region where this slope is nearly unity. The Fickian's diffusion regime for Li-ion MSD-t is shown in Figure 4.18.

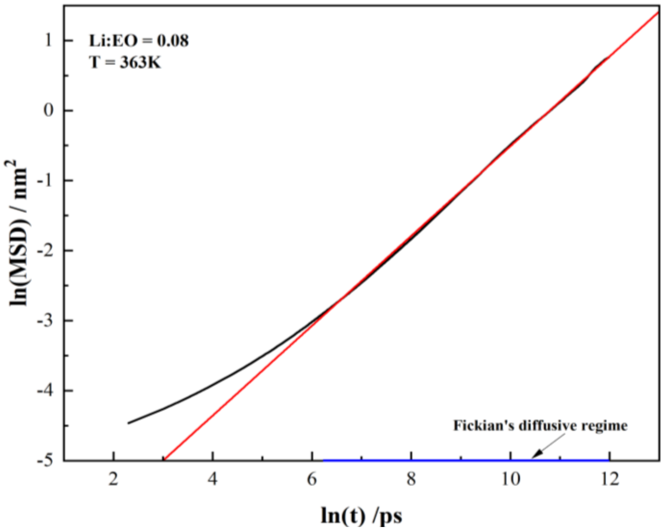

Figure 4.19: MSD-t (ln-ln) graph for Fickian's diffusive region at [Li: EO] = 0.08 and T = 363 K.

The MSD-t relationship of Li^+ at various temperatures is depicted in Figure 4.20a. In all systems, the MSD of Li-ion batteries rises as simulation time elapses. The rate of increase varies depending on the temperature. Furthermore, at higher temperatures, the beginning of diffusive regimes occurs over a significantly shorter duration. The MSD-t relationship of $TFSI^-$ is given in Figure 4.20b It can be seen that TFSI ions quickly travel toward the diffusive zone when the temperature rises. The non-linear regions of the MSD curve at the beginning and end of the curves are because of the calculation method done by the GROMACS code.[220]

The MSD-t relationship of Li^+ at various SN wt.% in PEO/PVDF/LiTFSI SPE is depicted in Figure 4.21a. The increasing trend was observed for all wt.% of SN in PBSPE. The rate of increase in MSD is higher for Li^+ when 20 wt.% of SN were added in PBSPE than the lower wt.% of SN showing that lithium ions move faster at this SN concentration. Whereas Figure 4.22b shows the MSD-t relation of $TFSI^-$ with increasing wt.% of SN. The addition of SN causes the subdiffusive region to convert more quickly into the long-lasting linear diffusive region.

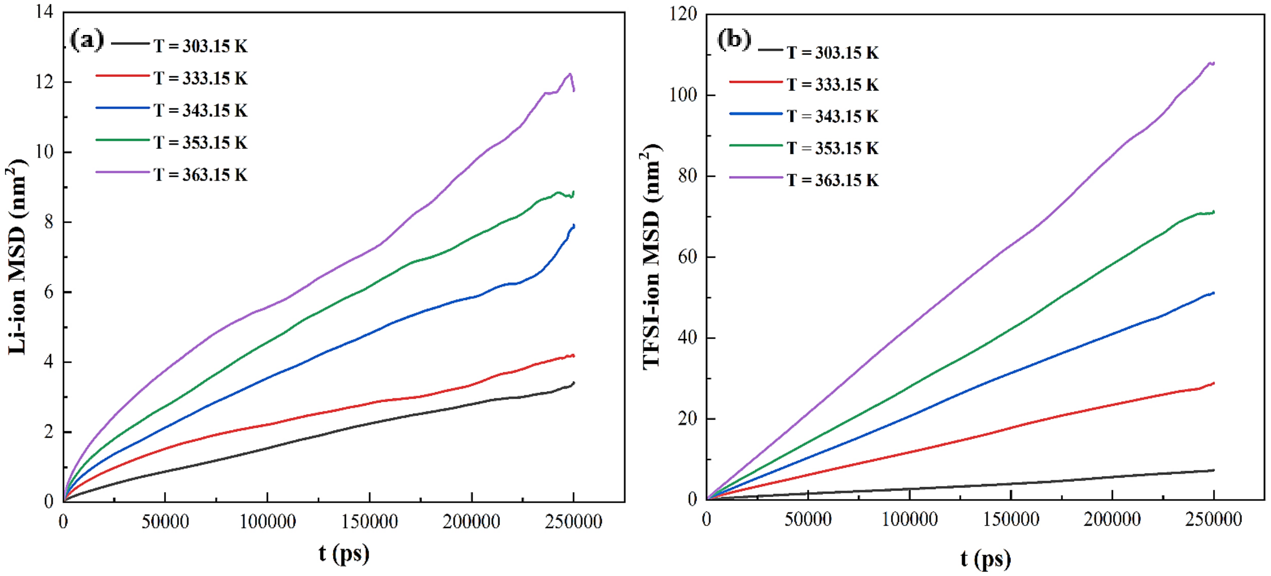

Figure 4.20: MSD-t relation of a) Li-ion and b) TFSI-ion in PBSPE system with varying temperature at [Li: EO] = 0.12.

.

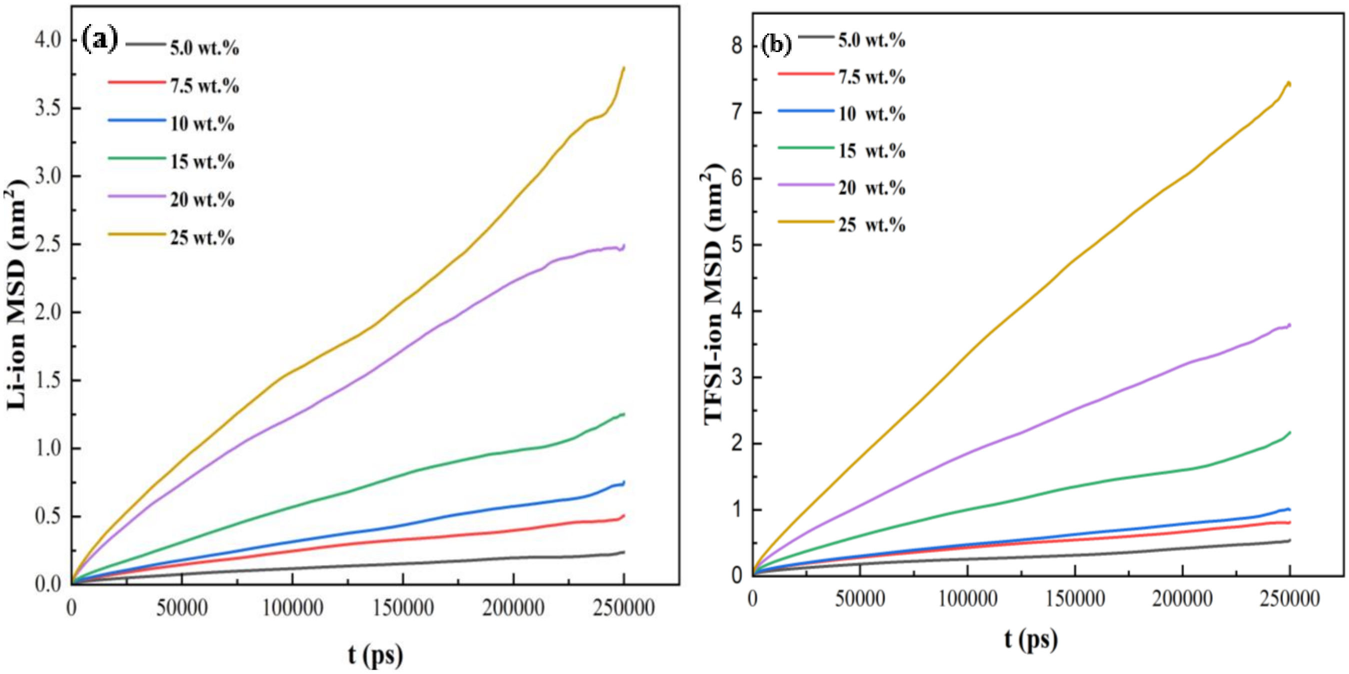

Figure 4.21: MSD-t relation of a) Li-ion, and b) TFSI-ion in PEO/PVDF/SN/LiTFSI BSPE system with varying temperature at [Li: EO] = 0.12.

The variation trend for both D^+ and D^- is the same as in PEO/LiTFSI SPEs, decreasing with increasing salt concentration ([Li: EO] = 0.02 to 0.2), regardless of the polymer species (Figure 4.22a). According to research conducted by Bruce et al.,[123] the movement of anions involves hopping from an occupied site to an available space that can accommodate the anion. Conversely, the movement of cations is characterized by the formation and breaking of coordinate bonds while transitioning between coordinating sites.[123] Thus, having more than one mode of transport may affect the diffusion coefficients of Li and TFSI ions, giving a nonlinear behavior for diffusion coefficients. The results indicate that BSPEs exhibit higher D^+ and D^- values than their non-blended counterparts, thereby enhancing ionic diffusion and conductivity for BSPEs (Figure 4.22b). There is a good qualitative agreement with the trend of previously published experimental and simulation results for SPEs.[156] This pattern has been observed in numerous SPEs with salt-rich compositions and can be interpreted in various ionic motion modes.[101, 124]

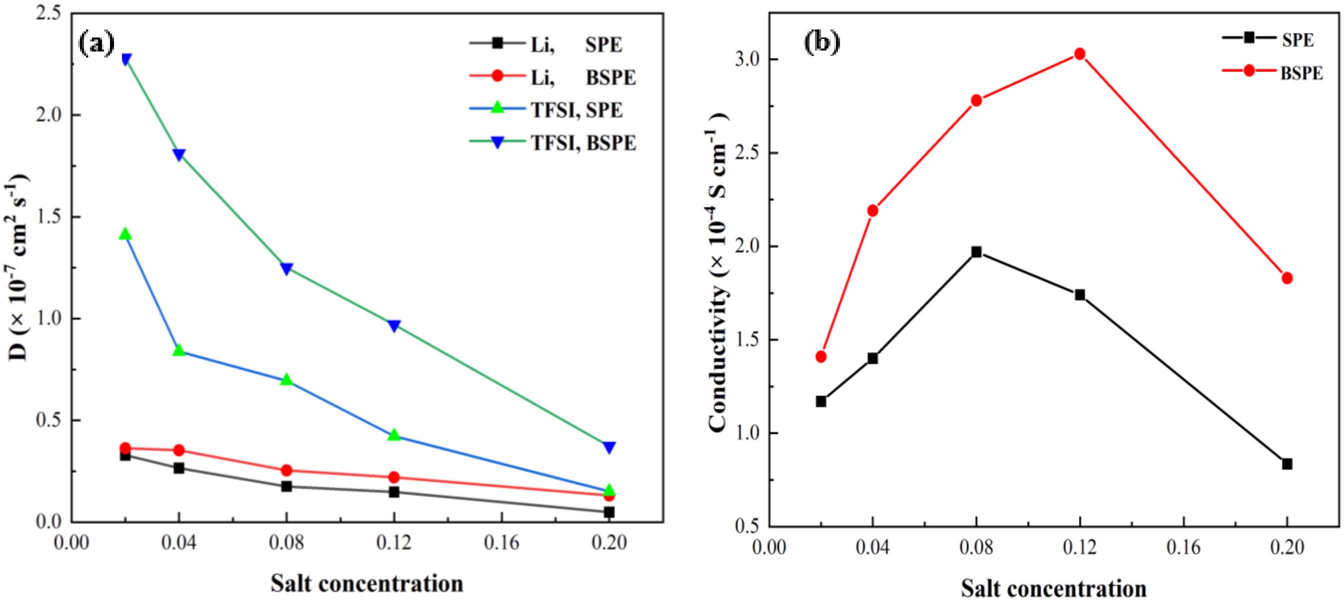

Figure 4.22: (a) Computed D^+ and D^-, and (b) ionic conductivity as a function of salt concentration at 363 K.

Initially, the ionic conductivity increases with increased salt concentrations due to more Li-ions available for coordinating with the polymer chain, which increases polymer segmental motion. The maximum ionic conductivity reaches salt concentrations of 0.08 and 0.12 for SPE and BSPE, respectively. Further, an increase in the salt concentration decreases the ionic conductivity. The smoothness of ionic conductivity can be attained by getting the data for more salt concentration ratios in SPE and BSPE systems.

The diffusivities of Li and TFSI ions are significantly impacted by the addition of SN, as shown in Figure 4.23(a). With an increase in SN weight percent, the diffusivities of Li-ion and TFSI-ion also rise. However, a significant rise was seen in the diffusivity of TFSI-ion as compared to Li-ion with an increasing amount of SN in PBSPE, with the highest value at 25 wt.%, which supports the concept that the addition of SN greatly influences the motion of TFSI-ions. The diffusion coefficient of Li and TFSI ions increases from 0.13×10^{-8} and 2.25×10^{-8} cm^2 s^{-1} with 0 wt% of SN to 2.11×10^{-8} and 4.73×10^{-8} cm^2 s^{-1} respectively, when loaded with 25 wt% of SN. Additionally, ions move more quickly at high temperatures, and the diffusivities of both the Li and TFSI ions increase exponentially with temperature (Figure 4.23b), in line with the trends shown in MSD curves (Figure 4.20). As temperature increases, the thermal motion of PEO segments becomes more erratic, and the transmission of Li-ions is inversely proportional to this segment motion. As a result, the temperature directly impacts the D of ions. The diffusion coefficient for TFSI-ion is larger than that for Li-ions because of size differences. Given that TFSI-ions are larger than Li-ions, they have unevenly dispersed charges compared to Li-ions. As a result, the TFSI-ions engage with counterions less frequently.

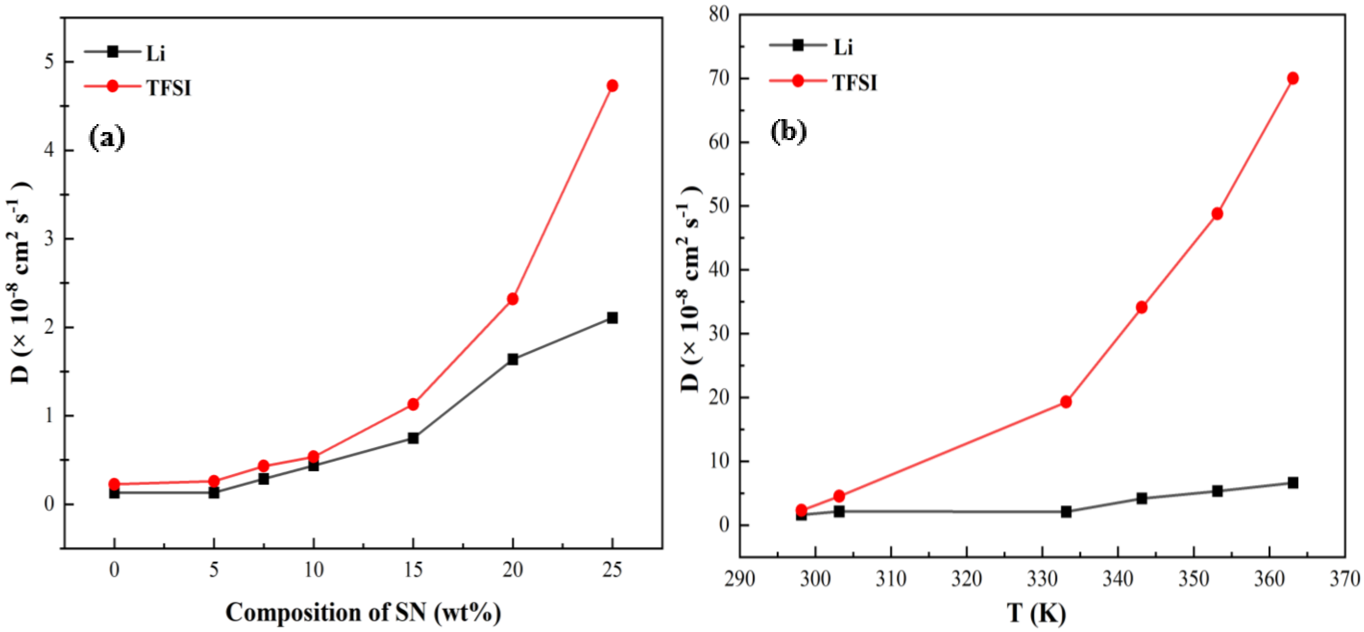

Figure 4.23: D^+ and D^- at different (a) wt% of SN, and (b) Temperature at [Li: EO] = 0.12 in PEO/PVDF/SN/LiTFSI.

As a result, TFSI-ions naturally have a more significant and smoother trend for diffusivity than Li-ions. Whereas, lithium ions have PEO, $TFSI^-$ and SN to interact with. Each species of lithium-ion has a different mode of transport affecting more on the diffusion of lithium ions. Also, with increasing temperature, the energy barrier between gauche and trans isomerism is lowered, which results in a greater number of SN molecules transforming from the gauche to the trans phase. The trans phase induces a higher degree of disorder, leading to faster dynamics giving an exponential increase in diffusion of $TFSI^-$ (Figure 4.23b).[165] Figure 4.24(a-d) shows diffusivity per mole of Li and TFSI ion at 10, 15, 20, and 25 wt.% of SN in the PBSPE system respectively. In a complex system like PEO/PVDF/SN/LiTFSI, diffusivity per mole of Li and TFSI ions refers to the rate of movement of these ions within the polymer matrix. Figure 4.24a shows that lithium-ions move faster than the TFSI$^-$ with the highest diffusivity of 5 × 10^{-8} cm^2 s^{-1} for the 18th Li$^+$ when 10 wt.% of SN were added. The diffusivity of TFSI$^-$ has the highest value up to 2 × 10^{-8} cm^2 s^{-1}. In the case of 15 wt.% of SN, TFSI$^-$ diffuses more than Li$^+$ reaching a value of as high as 20 × 10^{-8} cm^2 s^{-1} by 150th TFSI molecule (Figure 4.24b).

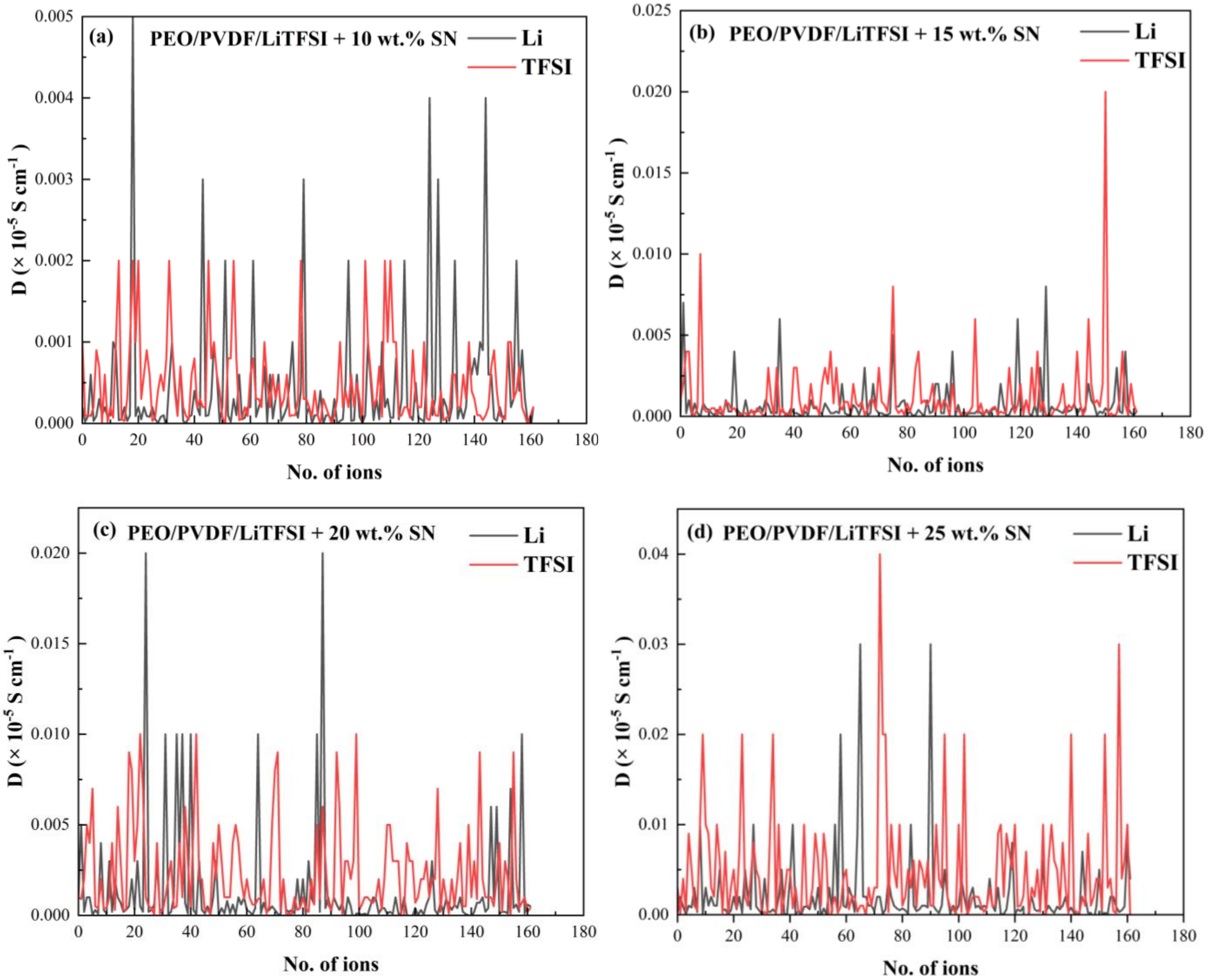

Figure 4.24: (a-d) Diffusivity per mole of Li-ion, and TFSI-ion in PBSPE system.

Further increasing the SN wt.% in BSPE increased the diffusivity of both Li^+ and $TFSI^-$ with the highest values of diffusivity 20×10^{-8} cm^2 s^{-1} and 10×10^{-8} cm^2 s^{-1} respectively (Figure 4.24c). In the case of 25 wt% of SN, an exceptional rise in diffusivity of 72nd $TFSI^-$ was observed (Figure 4.24d). These ions with the highest diffusivities per mole were the determining factors of change in lithium-ion transference number in the PBSPE system. Thus characterizing the diffusivity per mole of Li and TFSI ions aids in understanding the material's transport properties. This facilitates the optimization of the right concentration of plasticizer in SPEs for a better understanding of ionic conductivity and transference number. Figure 4.25 shows that the conductivity increases with increasing SN mass fraction, with the highest values of 0.145 mS cm^{-1} at room temperature when 25 wt.% SN was added to the PBSPE system.

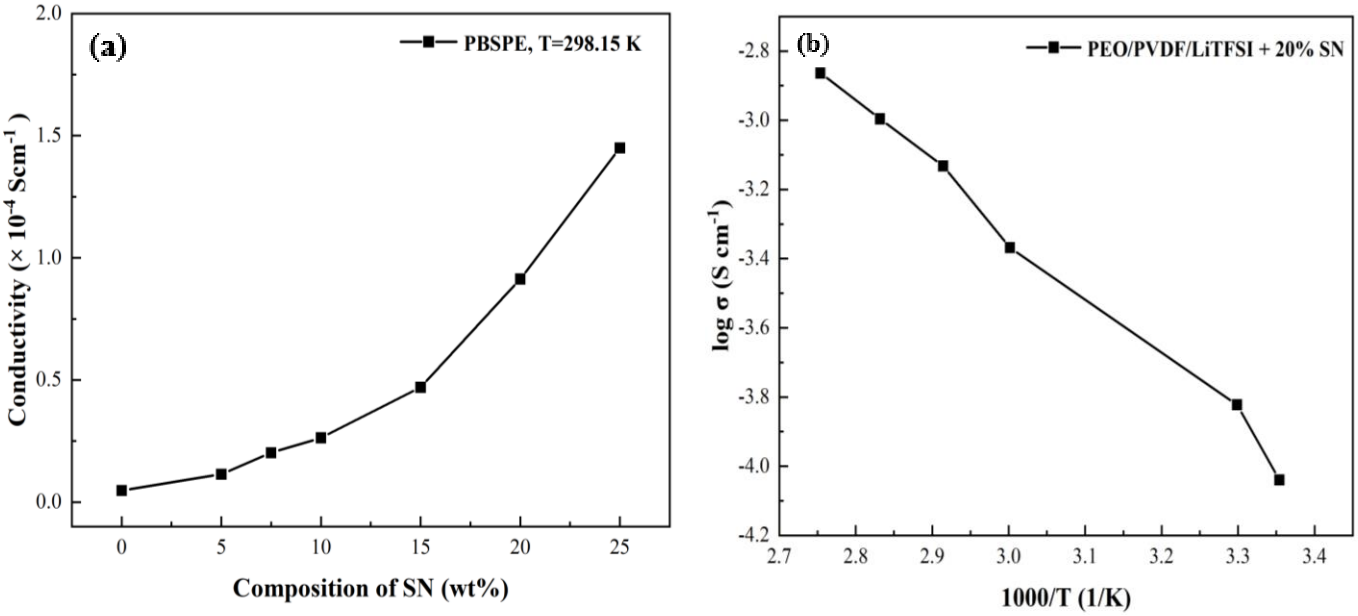

Figure 4.25: Simulated ionic conductivity at different (a) wt% of SN, and (b) Temperatures in PBSPE system.

Moreover, with the increase in temperature, the ionic conductivity increases to a value of 1.37×10^{-3} S cm^{-1} compared to that without SN (1.74×10^{-4} S cm^{-1}) at 363.15 K. Because the polymer electrolyte is prone to expansion in response to temperature changes, leading to an augmentation in the available space, consequently resulting in an elevation in its conductivity. The motion of the polymer backbone is strongly governed by the T_g of the system, and the free volume available, which can be influenced by different salt concentrations, fillers, and plasticizers will affect the free volume of the polymer. Systems following this type of mechanism often follow the Vogel-Tamann-Fulcher (VTF) behavior with temperature, which is characterized by a curved line in the Arrhenius plot and is typically found in polymer electrolytes based on PEO. Whereas traditional Arrhenius behavior is often seen in systems where the conductivity is believed to be due to hopping mechanisms of the ions between adjacent vacant sites. This behavior is represented by a straight line in the Arrhenius plot.

A nearly linear relationship between log and T^{-1} in Figure 4.25b shows that the conductivity follows the Vogel-Tamman-Fulcher (VTF) equation and Arrhenius theory. Such trends were also observed in the literature.[149, 154, 164] Moreover small deviations of ionic conductivity are seen at around T = 333.15 K. Because c In this stage, the system is suddenly heated to the reference temperature at the start and then tried to oscillate around the reference value. The final average simulated temperature of the system is underestimated (up to 2 or 3 points) than the reference value causing small errors in the final calculations of ionic conductivity. Similar curves can also be seen while simulating PEO in literature.[208]

Another important parameter that is directly affected by salt concentration and diffusion coefficients of ions is the lithium-ion transference number (t^+). Figure 4.26 shows that the lithium transference number calculated in this work ranges from 0.18 to 0.26 at 363 K as salt concentration increases from 0.02 to 0.20 in a pure SPE system. Nerneset-Einstein (NE) equation is used to calculate the Li^+ transference number from the diffusion coefficients of ions. The diffusion coefficients of ions were strongly affected by the addition of salt which further affected the t^+. In the NE equation diffusion coefficient of $TFSI^-$ (D^-) lies in the denominator, and thus has an opposite changing effect on t^+. The true transference number in PEO/LiTFSI mixtures may vary from those obtained using approximate methods such Bruce-Vincent method[123] and given vibrational spectroscopic results.[226]

From Figure 4.26a, it is clear that t^+ increases up to a value of 0.24 as salt concentration increases to 0.04, owing to an increase in the number of lithium-ion charge carriers in PEO/LiTFSI SPE. On further addition of salt, t^+ decreases to a value of 0.20 because the addition of salt may slow down the segmental motion of polymer chains. This can reduce the mobility of the ions, particularly the cations, which are coordinated with the ether oxygens in PEO. Further increase of t^+ after salt concentration 0.08 corresponds to a decrease in anion mobility (D^-) because of a reduction in free volume with increasing ion density. Mutual diffusion coefficients and transference numbers are also affected by the state of dissociation of the salt. A small decrease in t^+ from the highest value 0.26 to 0.245 was also observed. This decrease in t^+ can be attributed to Li-TFSI cluster formation at a high salt concentration of 0.20. The Li-TFSI cluster formation can also be seen in Figure 4.9b at a salt concentration ratio of 0.20 in PEO/LiTFSI SPE. The non-monotonic dependence of the mutual diffusion coefficient and transference number on salt concentration can be attributed to the fact that it is affected by more than one factor. These findings are also in line with the literature.[227, 228]

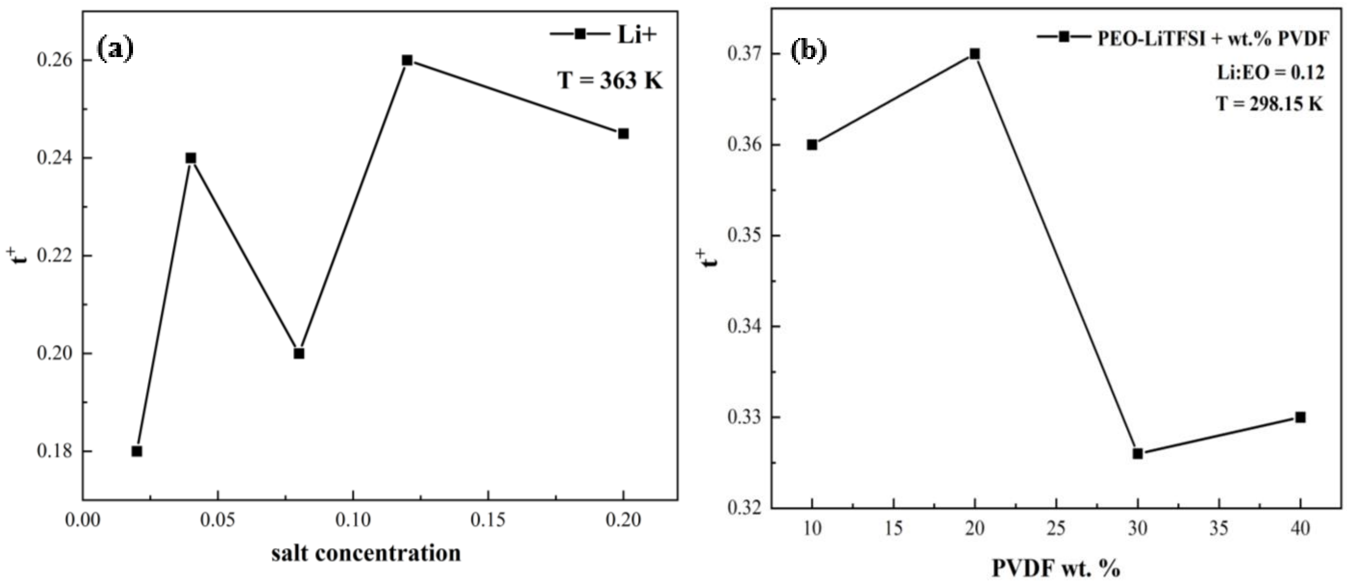

Figure 4.26: Lithium-ion transport number, t^+ with (a) varying salt concentration in SPE system, and (b) varying PVDF wt. % in the SPE system.

In the PEO/PVDF/LiTFSI BSPE, the transference number increases from 0.36-0.33 at RT while adding PVDF in the PEO/LiTFSI system (Figure 4.26b). It is noted that blending with PVDF has a positive effect on cation transference numbers for a certain composition range. At lower concentrations of PVDF, the addition of PVDF may initially improve the structural integrity and provide additional pathways for ion migration.[216] This could initially enhance lithium ion mobility, leading to an increase in the transference number. As the weight percentage of PVDF continues to increase beyond the optimal range (20 wt.% in this work), excessive PVDF might start hindering the mobility of lithium ions. The decrease of t^+ for PVDF fraction at 30 wt.% in the PEO/PVDF blended SPE indicates a notable alteration in the transport properties of the solid polymer electrolyte. This could be because of the interaction between PVDF and other components within the blend, leading to the disruption of lithium ion-conducting pathways. [229] This is clear from the slow increase in the diffusion coefficient of lithium-ion as compared to TFSI ion in Figure 4.13, which causes a decline in the lithium transference number at 30 wt.% of PVDF in PEO/LiTFSI.

Further small increase in t^+ at 40 wt.% of PVDF can be explained, because of the formation of new conductive pathways, reconfiguration of the polymer network, or altered ion-polymer dynamics. This is also supported by strong peaks of g(r) for Li^+-O_{PEO} and Li^+-$TFSI^-$ at 40 wt. % of PVDF in Figure 4.12 for lithium-ion in PEO/PVDF/LiTFSI BSPE.

Figure 4.26 shows the lithium-ion transference number dependence on SN mass fraction variation in PBSPE systems at RT (298.15 K). The highest t^+ achieved is 0.45 at RT when 10 wt.% of SN is added to the PBSPE system. SN helps in LiTFSI salt dissociation, which means that in PBSPE systems, Li-TFSI salt clusters may not be the dominant source of lithium-ion transfer. This is clear from the exponential rise in diffusion coefficients of $TFSI^-$ as compared to Li^+ (Figure 4.23a).

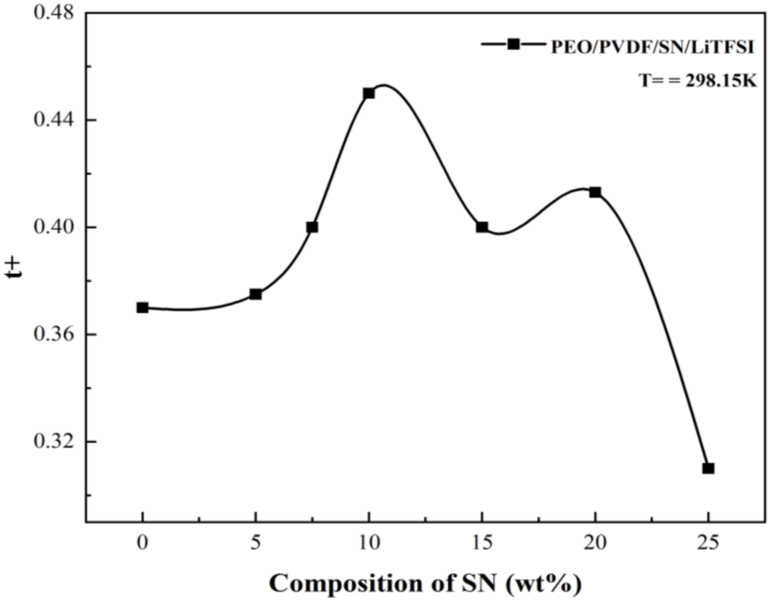

Figure 4.27: Li-ion transference number (t^+) with varying SN wt.% at room temperature in PBSPE system.

As the transference number is directly linked with the diffusion coefficients of ions, the increase in cationic motion has a positive effect on the transference number whereas an increase in anions motion impacts negatively on the transference number thus decreasing its value. Therefore, the large diffusion coefficient of TFSI-ion at 15 wt.% of SN is responsible for the decrease in t^+, because D^- is involved in the denominator of the equation for calculating the lithium-ion transference number. The slight increase in t^+ at 20 wt.% of SN can be attributed to the sudden increase in lithium-ion diffusion because more lithium ions move with high values of D as compared to lithium ions when 20 wt.% of SN is added to the PBSPE system (Figure 4.24). There are 10 wt.% and 20 wt.% of SN in the PBSPE system with the highest value of lithium-ion transference numbers of 0.41 and 0.45 and ionic conductivity values of 2.63×10^{-5} S cm^{-1} and 9.13×10^{-5} S cm^{-1} at T = 298.15 K, respectively. Overall, the results indicate that SN molecules have a significant impact on improving the mobility of Li^+ in PEO-based electrolytes which leads to a greater selection of PEO-based solid polymer electrolytes with high lithium ion conductivity and transference number for use in commercial applications.

Chapter 5. Conclusion

5.1 Contributions to Knowledge

This study explores the structural and dynamic properties of PEO/PVDF/SN/LiTFSI PBSPEs for lithium-ion batteries by CMD simulations. First, the concentration effect of PVDF on lithium ionic conductivity in pure SPE was studied. The highest Li^+ conductivity of up to 1.85×10^{-5} S cm^{-1} can be achieved at 40 wt.% of PVDF. The concept of lithium ions hopping from one TFSI-stabilized site to the next as the salt clusters create a percolating network, is clear from the sharp peak of RDF between Li^+ and $TFSI^-$ at 40 wt.% of PVDF. A solid plasticizer, SN was added to the PEO/PVDF/LiTFSI system to increase the ionic conductivity and lithium transference number. High lithium transference numbers of 0.45 and 0.41 were obtained at 10 wt.% and 20 wt.% of SN in the PEO/PVDF/LiTFSI system with RT ionic conductivities of 2.63×10^{-4}S cm^{-1} and 9.34×10^{-4} S cm^{-1}, respectively. The ionic conductivity can increase up to 1.37×10^{-3} S cm^{-1} at T = 363.15 K. The CN-Li^+ and CN-$TFSI^-$ interactions between SN and lithium salt were also studied through the MD simulation, proving the existence of a solvate-like structure of SN-LiTFSI. From the above results, it is clear that SN plays an important role in dissociating LiTFSI salt, thus increasing RT ionic conductivities and lithium transference number of solid polymer electrolyte systems. Furthermore, this study explores the non-monotonic dependence of lithium transference number on wt.% of PVDF and SN in SPE, which shows that not only the ionic conductivity but the lithium transference numbers must also be considered when selecting an SSE for LIBs.

5.2 Suggestions for Future Study

In this work, a facile blended polymerization technique was used to prepare polymer blends in which SN plasticizers were added to enhance the ion dynamics in blended SPE. Other techniques of modifying the host polymer through copolymerization, grafting, or crosslinking can be used in the future to change the lithium-ion hoping channels which may result in the improvement of lithium-ion dynamics. Furthermore, the increase in LiTFSI salt dissociation by adding SN in PEO/PVDF/LiTSI SPE in this work paves the way for future research to increase the lithium-ion transference number by regulating the PEO: PVDF ratio in PBSPE system.

References

1. S. Sorrell, Reducing energy demand: A review of issues, challenges, and approaches. Renewable and Sustainable Energy Reviews, 2015. 47: p. 74-82.
2. M. Santamouris, and K. Vasilakopoulou, Present and future energy consumption of buildings: Challenges and opportunities towards decarbonisation. e-Prime-Advances in Electrical Engineering, Electronics and Energy, 2021. 1: p. 100002.
3. C. D. M. Jr., D.A. Dowling, and J. Zhou, The power of an idea: the international impacts of the grand challenges for engineering. Engineering, 2016. 2(1): p. 4-7.
4. A. Q. Al-Shetwi, Sustainable development of renewable energy integrated power sector: Trends, environmental impacts, and recent challenges. Science of the Total Environment, 2022: p. 153645.
5. G. B. Kumar, and K. Palanisamy, Review of energy storage system for microgrid. Microgrid Technologies, 2021: p. 57-90.
6. B. Bhardwaj, and N. Bhardwaj. Hydrokinetic-Solar Hybrid Floating Renewable Energy Generation System to Explore Hydro and Solar Power Potential Worldwide. in Proceedings of the 2nd International Conference on Large-Scale Grid Integration of Renewable Energy in India, New Delhi, India. 2019.
7. F. A. Farret, and M.G. Simoes, Integration of alternative sources of energy. Vol. 504. 2006: Wiley Online Library.
8. W. Kempton, and J. Tomic, Vehicle-to-grid power implementation: From stabilizing the grid to supporting large-scale renewable energy. Journal of Power Sources, 2005. 144(1): p. 280-294.

9. H. Lund, Renewable energy strategies for sustainable development. Energy, 2007. 32(6): p. 912-919.

10. S. O. Amrouche, D. Rekioua, T. Rekioua, S. Bacha, Overview of energy storage in renewable energy systems. International Journal of Hydrogen Energy, 2016. 41(45): p. 20914-20927.

11. P. Wang, X. Yang, and Q. Zhang, Physical Energy Storage Technologies: Basic Principles, Parameters, and Applications. Highlights in Science, Engineering and Technology, 2022. 3: p. 73-84.

12. X. Wang, X. Lu, B. Liu, D. Chen, Y. Tong, and G. Shen, Flexible energy-storage devices: design consideration and recent progress. Advanced Materials, 2014. 26(28): p. 4763-4782.

13. T. Chen, Y. Jin, H. Lv, A. Yang, M. Liu, B. Chen, Y. Xie, and Q. Chen, Applications of lithium-ion batteries in grid-scale energy storage systems. Transactions of Tianjin University, 2020. 26(3): p. 208-217.

14. J. Verma, and D. Kumar, Metal-ion batteries for electric vehicles: current state of the technology, issues and future perspectives. Nanoscale Advances, 2021. 3(12): p. 3384-3394.

15. H. Pinegar, and Y. R. Smith, Recycling of end-of-life lithium-ion batteries, Part I: Commercial processes. Journal of Sustainable Metallurgy, 2019. 5: p. 402-416.

16. Y. Wang, B. Liu, Q. Li, S. Cartmell, S. Ferrara, Z. D. Deng, and J. Xiao, Lithium and lithium-ion batteries for applications in microelectronic devices: A review. Journal of Power Sources, 2015. 286: p. 330-345.

17. A. Eftekhari, Energy efficiency: a critically important but neglected factor in battery research. Sustainable Energy & Fuels, 2017. 1(10): p. 2053-2060.

18. H. Ali, H. A. Khan, and M.G. Pecht, Circular economy of Li Batteries: Technologies and trends. Journal of Energy Storage, 2021. 40: p. 102690.

19. Y. Tian, G. Zeng, A. Rutt, T. Shi, H. Kim, J. Wang, J. Koettgen, Y. Sun, B. Ouyang, T. Chen, Z. Lun, Z. Rong, K. Persson, and G. Ceder, Promises and challenges of next-generation "beyond Li-ion" batteries for electric vehicles and grid decarbonization. Chemical Reviews, 2020. 121(3): p. 1623-1669.

20. B. Dunn, H. Kamath, and J. M. Tarascon, Electrical energy storage for the grid: a battery of choices. Science, 2011. 334(6058): p. 928-935.

21. D. P. Dubal, O. Ayyad, V. Ruiz, P. G. Romero, Hybrid energy storage: the merging of battery and supercapacitor chemistries. Chemical Society Reviews, 2015. 44(7): p. 1777-1790.

22. A. Pique, and D. B. Chrisey, Direct-write technologies for rapid prototyping applications: sensors, electronics, and integrated power sources. 2002: Academic Press.

23. R. Rath, P. Kumar, S. Mohanty, S. K. Nayak, Recent advances, unsolved deficiencies, and future perspectives of hydrogen fuel cells in transportation and portable sectors. International Journal of Energy Research, 2019. 43(15): p. 8931-8955.

24. A. G. Sharma, A. Aray, F. S. Mirsafi, R. Abolhassani, H. Rubahn, J. Yu, and Y. K. Mishra, Progress in electrode and electrolyte materials: path to all-solid-state Li-ion batteries, Energy Advances, 2022. 1(8): p. 457-510.

25. F. Chen, J. Han, D. Kong, Y. Yuan, J. Xiao, S. Wu, D. M. Tang, Y. Deng, W. Lv, J. Lu, F. Kang, and Q. H. Yang, 1000 Wh L^{-1} lithium-ion batteries enabled by crosslink-shrunk tough carbon encapsulated silicon microparticle anodes. National Science Review, 2021. 8(9): p. nwab012.

26. T. Placke, R. Kloepsch, S. Duhnen, and M. Winter, Lithium-ion, lithium metal, and alternative rechargeable battery technologies: the odyssey for high energy density. Journal of Solid State Electrochemistry, 2017. 21: p. 1939-1964.

27. A. Manthiram, An outlook on lithium-ion battery technology. ACS Central Science, 2017. 3(10): p. 1063-1069.

28. M. M. Thackeray, C. Wolverton, and E. D. Isaacs, Electrical energy storage for transportation approaching the limits of, and going beyond, lithium-ion batteries. Energy & Environmental Science, 2012. 5(7): p. 7854-7863.

29. X. Shen, X. Q. Zhang, F. Ding, J. Q. Huang, R. Xu, X. Chen, C. Yan, F. Y. Su, C. M. Chen, X. Liu, and Q. Zhang, Advanced electrode materials in lithium batteries: retrospect and prospect. Energy Material Advances, 2021. 2021.

30. E. K. Heidari, A. K. Gol, M. H. Sohi, and A. Ataie, Electrode materials for lithium-ion batteries: a review. Journal of Ultrafine Grained and Nanostructured Materials, 2018. 51(1): p. 1-12.

31. Z. J. Zhang, and P. Ramadass, Lithium-ion battery systems and technology, in Batteries for Sustainability: Selected Entries from the Encyclopedia of Sustainability Science and Technology. 2012, Springer. p. 319-357.

32. G. B. Goodenough, Evolution of strategies for modern rechargeable batteries. Accounts of Chemical Research, 2013. 46(5): p. 1053-1061.

33. M. S. Whittingham, Lithium batteries and cathode materials. Chemical Reviews, 2004. 104(10): p. 4271-4302.

34. B. Rowden, and N. G. Araez, Estimating lithium-ion battery behavior from half-cell data. Energy Reports, 2021. 7: p. 97-103.

35. T. M. Bandhauer, S. Garimella, and T. F. Fuller, A critical review of thermal issues in lithium-ion batteries. Journal of the Electrochemical Society, 2011. 158(3): p. R1.

36. C. Vincent, and B. Scrosati, Modern batteries. 1997: Elsevier.

37. Y. Liang, and Y. Yao, Designing modern aqueous batteries. Nature Reviews Materials, 2023. 8(2): p. 109-122.

38. M. S. Whittingham, Materials challenges facing electrical energy storage. Mrs Bulletin, 2008. 33(4): p. 411-419.

39. Y. Sasaki, Organic electrolytes of secondary lithium batteries. Electrochemistry, 2008. 76(1): p. 2-15.

40. L. Fan, S. Wei, S. Li, Q. Li, and Y. Lu, Recent progress of the solid-state electrolytes for high-energy metal-based batteries. Advanced Energy Materials, 2018. 8(11): p. 1702657.

41. J. Kalhoff, G. G. Eshetu, D. Bresser, and S. Passerini, Safer electrolytes for lithium-ion batteries: state of the art and perspectives. ChemSusChem, 2015. 8(13): p. 2154-2175.

42. H. Niu, L. Wang, P. Guan, N. Zhang, C. Yan, M. Ding, X. Guo, T. Huang, and X. Hu, Recent advances in application of ionic liquids in electrolyte of lithium-ion batteries. Journal of Energy Storage, 2021. 40: p. 102659.

43. J. Xing, S. Bliznakov, L. Bonville, M. Oljaca, and R. Maric, A Review of Nonaqueous Electrolytes, Binders, and Separators for Lithium-Ion Batteries. Electrochemical Energy Reviews, 2022. 5(4): p. 14.

44. G. Appetecchi, M. Montanino, and S. Passerini, Ionic liquid-based electrolytes for high energy, safer lithium batteries, in Ionic Liquids: Science and Applications. 2012, ACS Publications. p. 67-128.

45. X. Gao, F. Wu, A. Mariani, and S. Passerini, Concentrated Ionic-Liquid-Based Electrolytes for High-Voltage Lithium Batteries with Improved Performance at Room Temperature. ChemSusChem, 2019. 12(18): p. 4185-4193.

46. X. Tang, S. Lv, K. Jiang, G. Zhou, and X. Liu, Recent development of ionic liquid-based electrolytes in lithium-ion batteries. Journal of Power Sources, 2022. 542: p. 231792.

47. T. Yim, M. S. Kwon, J. Mun, and K. T. Lee, Room temperature ionic liquid-based electrolytes as an alternative to carbonate-based electrolytes. Israel Journal of Chemistry, 2015. 55(5): p. 586-598.

48. D. R. Macfarlane, N. Tachikawa, M. Forsyth, J. M. Pringle, P. C. Howlett, G. D. Elliott, J. H. Davis Jr., M. Watanabe, P. Simon, and C. A. Angell, Energy applications of ionic liquids. Energy & Environmental Science, 2014. 7(1): p. 232-250.

49. W. Zhang, J. Nie, F. Li, Z. L. Wang, and C. Sun, A durable and safe solid-state lithium battery with a hybrid electrolyte membrane. Nano Energy, 2018. 45: p. 413-419.

50. M. Forsyth, L. Porcarelli, X. Wang, N. Goujon, and David Mecerreyes, Innovative electrolytes based on ionic liquids and polymers for next-generation solid-state batteries. Accounts of Chemical Research, 2019. 52(3): p. 686-694.

51. X. Chen, Z. Guan, F. Chu, Z. Xue, F. Wu, and Y. Yu, Air-stable inorganic solid-state electrolytes for high energy density lithium batteries: Challenges, strategies, and prospects. InfoMat, 2022. 4(1): p. e12248.

52. B. D. McCloskey, Attainable gravimetric and volumetric energy density of Li–S, and Li ion battery cells with solid separator-protected Li metal anodes. The Journal of Physical Chemistry Letters, 2015. 6(22): p. 4581-4588.

53. J. W. Fergus, Ceramic and polymeric solid electrolytes for lithium-ion batteries. Journal of Power Sources, 2010. 195(15): p. 4554-4569.

54. L. Han, M. L. Lehmann, J. Zhu, T. Liu, Z. Zhou, X. Tang, C. T. Heish, A. P. Sokolov, P. Cao, X. C. Chen, and T. Saito, Recent developments and challenges in hybrid solid electrolytes for lithium-ion batteries. Frontiers in Energy Research, 2020. 8: p. 202.

55. T. Famprikis, P. Canepa, J. A. Dawson, M. S. Islam, and C. Masquelier, Fundamentals of inorganic solid-state electrolytes for batteries. Nature Materials, 2019. 18(12): p. 1278-1291.

56. J. Chen, J. Wu, X. Wang, and Z. Yang, Research progress and application prospect of solid-state electrolytes in commercial lithium-ion power batteries. Energy Storage Materials, 2021. 35: p. 70-87.

57. H. J. Chu, Potential Composite Solid-State Electrolyte for Lithium-Ion Batteries. 2023, University of California, Los Angeles.

58. V. Thangadurai, S. Adams, and W. Weppner, Crystal structure revision and identification of Li^+-ion migration pathways in the garnet-like $Li_5La_3M_2O_{12}$ (M= Nb, Ta) oxides. Chemistry of Materials, 2004. 16(16): p. 2998-3006.

59. L. V. Wullen, T. Echelmeyer, H. W. Meyer, and D. Wilmer, The mechanism of Li-ion transport in the garnet $Li_5La_3Nb_2O_{12}$. Physical Chemistry Chemical Physics, 2007. 9(25): p. 3298-3303.

60. J. Awaka, A. Takashima, K. Kataoka, N. Kijima, Y. Idemoto, and J. Akimoto, Crystal structure of fast lithium-ion-conducting cubic $Li_7La_3Zr_2O_{12}$. Chemistry Letters, 2011. 40(1): p. 60-62.

61. Y. Li, B. Xu, H. Xu, H. Duan, X. Lu, S. Xin, W. Zhou, L. Xue, G. Fu, A. Manthiram, and J. B. Goodenough, Hybrid polymer/garnet electrolyte with a small interfacial resistance for lithium-ion batteries. Angewandte Chemie International Edition, 2017. 56(3): p. 753-756.

62. Y. Inaguma, C. Liquan, M. Itoh, T. Nakamura, T. Uchida, H. Ikuta, and M. Wakihara, High ionic conductivity in lithium lanthanum titanate. Solid State Communications, 1993. 86(10): p. 689-693.

63. C. Cao, Z. B. Li, X. L. Wang, X. B. Zhao, and W. Q. Han, Recent advances in inorganic solid electrolytes for lithium batteries. Frontiers in Energy Research, 2014. 2: p. 25.

64. Y. Zhao, and L. L. Daemen, Superionic conductivity in lithium-rich anti-perovskites. Journal of the American Chemical Society, 2012. 134(36): p. 15042-15047.

65. I. Abrahams, and E. Hadzifejzovic, Lithium ion conductivity and thermal behaviour of glasses and crystallised glasses in the system Li_2O-Al_2O_3-TiO_2-P_2O_5. Solid State Ionics, 2000. 134(3-4): p. 249-257.

66. K. Takada, T. Inada, A. Kajiyama, M. Kouguchi, H. Sasaki., S. Kondo, Y. Michiue, S. Nakano, M. Tabuchi, and M. Watanabe, Solid-state lithium batteries with sulfide-based solid electrolytes, in Solid State Ionics: The Science and Technology of Ions in Motion. 2004, World Scientific. p. 425-436.

67. A. R. West, Crystal chemistry of some tetrahedral oxides. Zeitschrift für Kristallographie, 1975. 141(5-6): p. 422-436.

68. M. Murayama, R. Kanno, M. Irie, S. Ito, T. Hata, N. Sonoyama, Y. Kawamoto, Synthesis of new lithium ionic conductor thio-LISICON-lithium silicon sulfides system. Journal of Solid State Chemistry, 2002. 168(1): p. 140-148.

69. N. Kamaya, K. Homma, Y. Yamakawa, M. Hirayama, R. Kanno, M. Yonemura, T. Kamiyama, Y. Kato, S. Hama, K. Kawamoto, and Akio Mitsui, A lithium superionic conductor. Nature Materials, 2011. 10(9): p. 682-686.

70. Y. Mo, S. P. Ong, and G. Ceder, First principles study of the $Li_{10}GeP_2S_{12}$ lithium super ionic conductor material. Chemistry of Materials, 2012. 24(1): p. 15-17.

71. X. He, Y. Zhu, and Y. Mo, Origin of fast ion diffusion in super-ionic conductors. Nature Communications, 2017. 8(1): p. 15893.

72. Y. Zheng, Y. Yao, J. Ou, M. Li, D. Luo, H. Dou, Z. Li, K. Amine, A. Yu, and Z. Chen, A review of composite solid-state electrolytes for lithium batteries: fundamentals, key materials and advanced structures. Chemical Society Reviews 2020. 49(23): p. 8790-8839.

73. F. Croce, G. B. Appetecchi, L. Persi, and B. Scrosati, Nanocomposite polymer electrolytes for lithium batteries. Nature, 1998. 394(6692): p. 456-458.

74. H. H. Sumathipala, J. Hassoun, S. Panero, B. Scrosati, High performance PEO-based polymer electrolytes and their application in rechargeable lithium polymer batteries. Ionics, 2007. 13: p. 281-286.

75. Y. Jiang, X. Yan, Z. Ma, P. Mei, W. Xiao, Q. You, and Y. Zhang, Development of the PEO based solid polymer electrolytes for all-solid state lithium ion batteries. Polymers, 2018. 10(11): p. 1237.

76. S. Bandyopadhyay, N. Gupta, A. Joshi, A. Gupta, R. K. Srivastava, B. K. Kuila, and B. Nandan, Solid Polymer Electrolyte Based on an Ionically Conducting Unique Organic Polymer Framework for All-Solid-State Lithium Batteries. ACS Applied Energy Materials, 2023. 6(8): p. 4390-4403.

77. B. Huang, Z. Wang, L. Chen, R. Xue, and F. Wang, The mechanism of lithium ion transport in polyacrylonitrile-based polymer electrolytes. Solid State Ionics, 1996. 91(3-4): p. 279-284.

78. K. S. Perera, M. Dissanayake, S. Skaarup, and K. West, Application of polyacrylonitrile-based polymer electrolytes in rechargeable lithium batteries. Journal of Solid State Electrochemistry, 2008. 12: p. 873-877.

79. H. R. Jung, and W. J. Lee, Electrochemical characteristics of electrospun poly (methyl methacrylate)/polyvinyl chloride as gel polymer electrolytes for lithium ion battery. Electrochimica Acta, 2011. 58: p. 674-680.

80. H. T. T. Le, D. T. Ngo, R. S. Kalubarme, G. Cao, C. N. Park, and C. J. Park, Composite gel polymer electrolyte based on poly (vinylidene fluoride-hexafluoropropylene)(PVDF-HFP) with modified aluminum-doped lithium lanthanum titanate (A-LLTO) for high-performance lithium rechargeable batteries. ACS Applied Materials & Interfaces, 2016. 8(32): p. 20710-20719.

81. S. Zhou, S. Zhong, Y. Dong, Z. Liu, L. Dong, B. Yuan, H. Xie, Y. Liu, L. Qiao, J. Han, and W. He, Composition and Structure Design of Poly (vinylidene fluoride)-Based Solid Polymer Electrolytes for Lithium Batteries. Advanced Functional Materials, 2023. 33(20): p. 2214432.

82. K. Murata, S. Izuchi, and Y. Yoshihisa, An overview of the research and development of solid polymer electrolyte batteries. Electrochimica Acta, 2000. 45(8-9): p. 1501-1508.

83. K. Abraham, V. Koch, and T. Blakley, Inorganic-Organic Composite Solid Polymer Electrolytes. Journal of the Electrochemical Society, 2000. 147(4): p. 1251.

84. X. Judez, H. Zhang, C. Li, G. G. Eshetu, J. A. Gonzalez-Marcos, M. Armand and L. M. Rodriguez-Martinez, Solid electrolytes for safe and high energy density lithium-sulfur batteries: promises and challenges. Journal of The Electrochemical Society, 2017. 165(1): p. A6008.

85. Z. Xue, D. He, and X. Xie, Poly (ethylene oxide)-based electrolytes for lithium-ion batteries. Journal of Materials Chemistry A, 2015. 3(38): p. 19218-19253.

86. E. Staunton, Y. G. Andreev, and P. G. Bruce, Structure and conductivity of the crystalline polymer electrolyte β-PEO_6: $LiAsF_6$. Journal of the American Chemical Society, 2005. 127(35): p. 12176-12177.

87. B. Kumar, and L. G. Scanlon, Polymer-ceramic composite electrolytes. Journal of Power Sources, 1994. 52(2): p. 261-268.

88. S. Xia, X. Wu, Z. Zhang, Y. Cui, and W. Liu, Practical challenges and future perspectives of all-solid-state lithium-metal batteries. Chem, 2019. 5(4): p. 753-785.

89. F. Capuano, F. Croce, and B. Scrosati, Composite polymer electrolytes. Journal of the Electrochemical Society, 1991. 138(7): p. 1918.

90. J. Feng, L. Wang, Y. Chen, P. Wang, H. Zhang, and X. He, PEO based polymer-ceramic hybrid solid electrolytes: a review. Nano Convergence, 2021. 8: p. 1-12.

91. W. Wieczorek, Z. Florjanczyk, and J. Stevens, Composite polyether based solid electrolytes. Electrochimica Acta, 1995. 40(13-14): p. 2251-2258.

92. C. G. Tan, W. O. Siew, W. L. Pang, Z. Osman, and K. W. Chew, The effects of ceramic fillers on the PMMA-based polymer electrolyte systems. Ionics, 2007. 13: p. 361-364.

93. F. Croce, L. Persi, B. Scrosati, F. Serraino-Fiory, E. Plichta, and M.A Hendrickson, Role of the ceramic fillers in enhancing the transport properties of composite polymer electrolytes. Electrochimica Acta, 2001. 46(16): p. 2457-2461.

94. J. H. Choi, C. H. Lee, J. H. Yu, C. H. Doh, and S. M. Lee, Enhancement of ionic conductivity of composite membranes for all-solid-state lithium rechargeable batteries incorporating tetragonal $Li_7La_3Zr_2O_{12}$ into a polyethylene oxide matrix. Journal of Power Sources, 2015. 274: p. 458-463.

95. M. Keller, G. B. Appetecchi, G. Tae Kim, V. Sharova, M. Schneider, J. Schuhmacher, A. Roters, and S. Passerini, Electrochemical performance of a solvent-free hybrid ceramic-polymer electrolyte based on $Li_7La_3Zr_2O_{12}$ in $P(EO)_{15}LiTFSI$. Journal of Power Sources, 2017. 353: p. 287-297.

96. J. H. Cha, P. N. Didwal, J. M. Kim, D. R. Chang, C. J. Park, Poly(ethylene oxide)-based composite solid polymer electrolyte containing $Li_7La_3Zr_2O_{12}$ and poly(ethylene glycol) dimethyl ether. Journal of Membrane Science, 2020. 595: p. 117538.

97. J. Zhang, X. Zang, H. Wen, T. Dong, J. Chai, Y. Li, B. Chen, J. Zhao, S. Dong, J. Ma, L. Yue, Z. Liu, X. Guo, G. Cui and L. Chen, High-voltage and free-standing poly (propylene carbonate)/$Li_{6.75}La_3Zr_{1.75}Ta_{0.25}O_{12}$ composite solid electrolyte for wide temperature range and flexible solid lithium ion battery. Journal of Materials Chemistry A, 2017. 5(10): p. 4940-4948.

98. B. J. Sung, P. N. Didwal, R. Verma, A. G. Nguyen, D. R. Chang, and C. J. Park, Composite solid electrolyte comprising poly (propylene carbonate) and $Li_{1.5}Al_{0.5}Ge_{1.5}(PO_4)_3$ for long-life all-solid-state Li-ion batteries. Electrochimica Acta, 2021. 392: p. 139007.

99. W. Liu, N. Liu, J. Sun, P. C. Hsu, Y. Li, H. W. Lee, Y. Cui, Ionic conductivity enhancement of polymer electrolytes with ceramic nanowire fillers. Nano Letters, 2015. 15(4): p. 2740-2745.

100. W. Liu, S. W. Lee, D. Lin, F. Shi, S. Wang, A. D. Sendek, and Y Cui, Enhancing ionic conductivity in composite polymer electrolytes with well-aligned ceramic nanowires. Nature Energy, 2017. 2(5): p. 1-7.

101. Y. H. Zhang, M. N. Lu, Q. Li, and F. N. Shi, Hybrid lithium salts regulated solid polymer electrolyte for high-temperature lithium metal battery. Journal of Solid State Chemistry, 2022. 310: p. 123072.

102. Z. Stoeva, I. M. Litas, E. Staunton, Y. G. Andreev, and P. G. Bruce, Ionic conductivity in the crystalline polymer electrolytes PEO6: LiXF6, X= P, As, Sb. Journal of the American Chemical Society, 2003. 125(15): p. 4619-4626.

103. R. He and T. Kyu, Effect of plasticization on ionic conductivity enhancement in relation to glass transition temperature of crosslinked polymer electrolyte membranes. Macromolecules, 2016. 49(15): p. 5637-5648.

104. L. P. Teo, M. H. Buraidah, and A. K. Arof, Development on solid polymer electrolytes for electrochemical devices. Molecules, 2021. 26(21): p. 6499.

105. Y. Zhang, W. Lu, L. Cong, J. Liu, L. Sun, A. Mauger, C. M. Julien, H. Xie, and J. Liu, Cross-linking network based on Poly (ethylene oxide): Solid polymer electrolyte for room temperature lithium battery. Journal of Power Sources, 2019. 420: p. 63-72.

106. M. Kadir, S. Majid, and A. Arof, Plasticized chitosan–PVA blend polymer electrolyte based proton battery. Electrochimica Acta, 2010. 55(4): p. 1475-1482.

107. G. Hirankumar, and N. Mehta, Effect of incorporation of different plasticizers on structural and ion transport properties of PVA-LiClO4 based electrolytes. Heliyon, 2018. 4(12).

108. Y. Sun, T. Yang, H. Ji, J. Zhou, Z. Wang, T. Qian, and C. Yan, Boosting the optimization of lithium metal batteries by molecular dynamics simulations: A perspective. Advanced Energy Materials, 2020. 10(41): p. 2002373.

109. M. C. Roco, M. C. Hersam, C. A. Mirkin, M. Lundstrom, P. Cummings, and M Alam, Investigative tools: theory, modeling, and simulation. Nanotechnology Research Directions for Societal Needs in 2020: Retrospective and Outlook, 2011: p. 29-69.

110. J. Lim, K. K. Lee, C. Liang, K. H. Park, M. Kim, K. Kwak, and M. Cho, Two-dimensional infrared spectroscopy and molecular dynamics simulation studies of nonaqueous lithium ion battery electrolytes. The Journal of Physical Chemistry B, 2019. 123(31): p. 6651-6663.

111. F. M. Plathe, and W. F. Van Gunsteren, Computer simulation of a polymer electrolyte: Lithium iodide in amorphous poly (ethylene oxide). The Journal of Chemical Physics, 1995. 103(11): p. 4745-4756.

112. S. Neyertz, and D. Brown, Local structure and mobility of ions in polymer electrolytes: a molecular dynamics simulation study of the amorphous PEO_xNaI system. The Journal of Chemical Physics, 1996. 104(10): p. 3797-3809.

113. O. Borodin, and G. D. Smith, Molecular dynamics simulations of poly(ethylene oxide)/LiI melts. 2. Dynamic properties. Macromolecules, 2000. 33(6): p. 2273-2283.

114. D. Kony, W. Damm, S. Stoll, W. F. Van Gunsteren, An improved OPLS–AA force field for carbohydrates. Journal of Computational Chemistry, 2002. 23(15): p. 1416-1429.

115. Y. Sakae, and Y. Okamoto, Optimisation of OPLS–UA force-field parameters for protein systems using protein data bank. Molecular Simulation, 2010. 36(14): p. 1148-1156.

116. T. S. Asche, P. Behrens, and A. M. Schneider, Validation of the COMPASS force field for complex inorganic–organic hybrid polymers. Journal of Sol-Gel Science and Technology, 2017. 81: p. 195-204.

117. S. L. Mayo, B. D. Olafson, and W. A. Goddard, DREIDING: a generic force field for molecular simulations. Journal of Physical Chemistry, 1990. 94(26): p. 8897-8909.

118. X. Zhu, P. E. Lopes, and A. D. MacKerell Jr, Recent developments and applications of the CHARMM force fields. Wiley Interdisciplinary Reviews: Computational Molecular Science, 2012. 2(1): p. 167-185.

119. B. R. Brooks, C. L. Brooks, A. D. Mackerell Jr., L. Nilsson, R. J. Petrella, B. Roux, Y. Won, G. Archontis, C. Bartels, S. Boresch, A. Caflisch, L. Caves, Q. Cui, A. R. Dinner, M. Feig, S. Fischer, J. Gao, M. Hodoscek, W. Im, K. Kuczera, T. Lazaridis, J. Ma, V. Ovchinnikov, E. Paci, R. W. Pastor, C. B. Post, J. Z. Pu, M. Schaefer, B. Tidor, R. M. Venable, H. L. Woodcock, X. Wu, W. Yang, D. M. York, and M. Karplus, CHARMM: the biomolecular simulation program. Journal of Computational Chemistry, 2009. 30(10): p. 1545-1614.

120. W. R. P. Scott, P. H. Hunenberger, I. G. Tironi, A. E. Mark, S. R. Billeter, J. Fennen, A. E. Torda, T. Huber, P. Kruger, and W. F. van Gunsteren, The GROMOS biomolecular simulation program package. The Journal of Physical Chemistry A, 1999. 103(19): p. 3596-3607.

121. D. A. Case, T. E. Cheatham, T. Darden, H. Gohlke, R. Luo, K. M. Merz Jr., A. Onufriev, C. Simmerling, B. Wang, and R. J. Woods, The Amber biomolecular simulation programs. Journal of Computational Chemistry, 2005. 26(16): p. 1668-1688.

122. D. V. D. Spoel, E. Lindahl, B. Hess, G. Groenhof, A. E. Mark, H. J. C. Berendsen, GROMACS: fast, flexible, and free. Journal of Computational Chemistry, 2005. 26(16): p. 1701-1718.

123. P. G. Bruce, and C. Vincent, Polymer electrolytes. Journal of the Chemical Society, Faraday Transactions, 1993. 89(17): p. 3187-3203

124. R. A. G. Whba, L. TianKhoon, M. S. Suait, M. Y. A. Rahman, and A. Ahmad, Influence of binary lithium salts on 49% poly (methyl methacrylate) grafted natural rubber based solid polymer electrolytes. Arabian Journal of Chemistry, 2020. 13(1): p. 3351-3361.

123. R. Tao, and T. Fujinami, Application of mix-salts composed of lithium borate and lithium aluminate in PEO-based polymer electrolytes. Journal of power sources, 2005. 146(1-2): p. 407-411.

126. Q. Zhao, P. Chen, S. Li, X. Liu, and L. A. Archer, Solid-state polymer electrolytes stabilized by task-specific salt additives. Journal of Materials Chemistry A, 2019. 7(13): p. 7823-7830.

127. F. W. Poulsen, N. H. Andersen, K. Clausen, S. Skaarup, and O. T. Sørensen, Transport-Structure Relations in Fast Ion and Mixed Conductors: Proceedings of the 6. Risø International Symposium on Metallurgy and Materials Science. 1985.

128. M. Giua, S. Panero, B. Scrosati, X. Cao, and S. G. Greenbaum, Investigation of mixed cation effects in $PEO_9Zn_{1-x}Cu_x(CF_3SO_3)_2$ polymer electrolytes. Solid State Ionics, 1996. 83(1-2): p. 73-78.

129. B. Jing, X. Wang, Y. Shi, Y. Zhu, H. Gao, and sS. K. Fullerton-Shirey, Combining Hyperbranched and Linear Structures in Solid Polymer Electrolytes to Enhance

Mechanical Properties and Room-Temperature Ion Transport. Frontiers in Chemistry, 2021. 9: p. 563864.

130. M. L. Lehmann, G. Yang, J. Nanda, and T. Saito, Well-designed crosslinked polymer electrolyte enables high ionic conductivity and enhanced salt solvation. Journal of The Electrochemical Society, 2020. 167(7): p. 070539.

131. O. G. Calvo, N. Lago, S. Devaraj, M. Armand, Cross-linked solid polymer electrolyte for all-solid-state rechargeable lithium batteries. Electrochimica Acta, 2016. 220: p. 587-594.

132. Y. C. Tsai, and C. C. Chiu, Solute Diffusivity and Local Free Volume in Cross-Linked Polymer Network: Implication of Optimizing the Conductivity of Polymer Electrolyte. Polymers, 2022. 14(10): p. 2061.

133. F. Fu, Y. Zheng, N. Jiang, Y. Liu, C. Sun, A. Zhang, H. Teng, L. Sun, and H. Xie, A Dual-Salt PEO-based polymer electrolyte with Cross-Linked polymer network for High-Voltage lithium metal batteries. Chemical Engineering Journal, 2022. 450: p. 137776.

134. Y. Yang, W. Li, N. Zhou, and J. Shen, Design and construction of cross-linked PEO with the integration of helical polyurethane as an advanced all-solid-state polymer electrolyte for lithium batteries. Journal of Chemical Education, 2020. 97(10): p. 3758-3765.

135. S. K. Patla, R. Ray, K. Asokan, and S. Karmakar, Investigation of ionic conduction in PEO-PVDF based blend polymer electrolytes. Journal of Applied Physics, 2018. 123(12): p. 125102.

136. A. Ghosh, and P. Kofinas, PEO based block copolymer as solid state lithium battery electrolyte. ECS Transactions, 2008. 11(29): p. 131.

137. D. Lee, H. Y. Jung, and M. J. Park, Solid-state polymer electrolytes based on AB3-type miktoarm star copolymers. ACS Macro Letters, 2018. 7(8): p. 1046-1050.

138. A. Chandra, Hot-pressed PEO-PVP blended solid polymer electrolytes: ion transport and battery application. Polymer Bulletin, 2016. 73(10): p. 2707-2718.

139. H. W. Han, W. Liu, J. Zhang, and X. Z. Zhao, A hybrid poly (ethylene oxide)/poly (vinylidene fluoride)/TiO_2 nanoparticle solid-state redox electrolyte for dye-sensitized nanocrystalline solar cells. Advanced Functional Materials, 2005. 15(12): p. 1940-1944.

140. P. Pradeepa, S. Edwin raj, G. Sowmya, J. Kalaiselvimary, and M. Ramesh Prabhu, Optimization of hybrid polymer electrolytes with the effect of lithium salt concentration in PEO/PVdF-HFP blends. Materials Science and Engineering: B, 2016. 205: p. 6-17.

141. L. Fan, Z. Dang, C. W. Nan, and M. Li, Thermal, electrical and mechanical properties of plasticized polymer electrolytes based on PEO/P (VDF-HFP) blends. Electrochimica Acta, 2002. 48(2): p. 205-209.

142. Z. He, L. Chen, B. Zhang, Y. Liu, L. Z. Fan, Flexible poly (ethylene carbonate)/garnet composite solid electrolyte reinforced by poly (vinylidene fluoride-hexafluoropropylene) for lithium metal batteries. Journal of Power Sources, 2018. 392: p. 232-238.

143. M. Guo, M. Zhang, D. He, J. Hu, X. Wang, C. Gong, X. Xie, and Z. Xue, Comb-like solid polymer electrolyte based on polyethylene glycol-grafted sulfonated polyether ether ketone. Electrochimica Acta, 2017. 255: p. 396-404.

144. R. Sengwa, S. Choudhary, and P. Dhatarwal, Influences of ultrasonic-and microwave-irradiated preparation methods on the structural and dielectric properties of (PEO-PMMA)-$LiCF_3SO_{3-x}$ wt% MMT nanocomposite electrolytes. Ionics, 2015. 21: p. 95-109.

145. T. M. Liu, D. Saikia, S. Y. Ho, M. C. Chen, and H. M. Kao, High ion-conducting solid polymer electrolytes based on blending hybrids derived from monoamine and diamine polyethers for lithium solid-state batteries. RSC Advances, 2017. 7(33): p. 20373-20383.

146. J. L. Olmedo-Martinez, L. Meabe, R. Riva, G. Guzman-Gonzalez, L. Porcarelli, M. Forsyth, A. Mugica, I. Calafel, A. J. Muller, P. Lecomte, C. Jerome and D. Mecerreyes, Flame retardant polyphosphoester copolymers as solid polymer electrolyte for lithium batteries. Polymer Chemistry, 2021. 12(23): p. 3441-3450.

147. T. N. Phan, S. Issa, and D. Gigmes, Poly(ethylene oxide)-based block copolymer electrolytes for lithium metal batteries. Polymer International, 2019. 68(1): p. 7-13.

148. R. P. Sengwa, P. Dhatarwal, and S. Choudhary, Role of preparation methods on the structural and dielectric properties of plasticized polymer blend electrolytes: correlation between ionic conductivity and dielectric parameters. Electrochimica Acta, 2014. 142: p. 359-370.

149. S. R. Ibrahim, R. Ahmad, and M. R. Johan, Conductivity and optical studies of plasticized solid polymer electrolytes doped with carbon nanotube. Journal of Luminescence, 2012. 132(1): p. 147-152.

150. M. J. Reddy, J. S. Kumar, U. V. S Rao, and P. P. Chu, Structural and ionic conductivity of PEO blend PEG solid polymer electrolyte. Solid State Ionics, 2006. 177(3-4): p. 253-256.

151. A. Kumar, and R. K. Gupta, Fundamentals of polymer engineering. 2018: CRC press.

152. L. Z. Fan, X. L. Wang, and F. Long, All-solid-state polymer electrolyte with plastic crystal materials for rechargeable lithium-ion battery. Journal of Power Sources, 2009. 189(1): p. 775-778.

153. G. Cardini, R. Righini, and S. Califano, Computer simulation of the dynamics of the plastic phase of succinonitrile. The Journal of Chemical Physics, 1991. 95(1): p. 679-685.

154. M. Zachariah, M. Romanini, P. Tripathi, M. Barrio, J. L. Tamarit, and R. Macovez, Self-Diffusion, Phase Behavior, and Li^+ Ion Conduction in Succinonitrile-Based Plastic, Cocrystals. The Journal of Physical Chemistry C, 2015. 119(49): p. 27298-27306.

155. R. Yang, S. Zhang, L. Zhang, and W. Liu, Electrical properties of composite polymer electrolytes based on PEO-SN-$LiCF_3SO_3$. Int. J. Electrochem. Sci, 2013. 8: p. 10163-10169.

156. H. Wang, C. Lin, X. Yan, A. Wu, S. Shen, G. Wei, and J. Zhang, Mechanical property-reinforced PEO/PVDF/$LiClO_4$/SN blend all solid polymer electrolyte for lithium ion batteries. Journal of Electroanalytical Chemistry, 2020. 869: p. 114156.

157. L. Z. Fan, and J. Maier, Composite effects in poly (ethylene oxide)–succinonitrile based all-solid electrolytes. Electrochemistry Communications, 2006. 8(11): p. 1753-1756.

158. P. S. Whitfield, Y. L. Page, A. Abouimrane, and I. J. Davidson Ab initio structure determination of the low-temperature phase of succinonitrile from laboratory X-ray powder diffraction data-Coping with potential poor powder quality using DFT ab initio methods. Powder Diffraction, 2008. 23(4): p. 292-299.

159. W. Zha, F. Chen, D. Yang, Q. Shen, and L. Zhang, High-performance $Li_{6.4}La_3Zr_{1.4}Ta_{0.6}O_{12}$/Poly(ethylene oxide)/Succinonitrile composite electrolyte for solid-state lithium batteries. Journal of Power Sources, 2018. 397: p. 87-94.

160. Q. Zhang, K. Liu, F. Ding, and X. Liu, Recent advances in solid polymer electrolytes for lithium batteries. Nano Research, 2017. 10: p. 4139-4174.

161. T. Wei, Z. H. Zhang, Z. M. Wang, Q. Zhang, Y. S. Ye, J. H. Lu, Z. Rahman, and Z. W. Zhang, Ultrathin solid composite electrolyte based on $Li_{6.4}La_3Zr_{1.4}Ta_{0.6}O_{12}$/PVDF-

HFP/LiTFSI/succinonitrile for high-performance solid-state lithium metal batteries. ACS Applied Energy Materials, 2020. 3(9): p. 9428-9435.

162. B. Chen, Z. Huang, X. Chen, Y. Zhao, Q. Xu, P. Long, S. Chen, and X. Xu, A new composite solid electrolyte PEO/$Li_{10}GeP_2S_{12}$/SN for all-solid-state lithium battery. Electrochimica Acta, 2016. 210: p. 905-914.

163. R. He, M. Echeverri, D. Ward, Y. Zhu, and T. Kyu, Highly conductive solvent-free polymer electrolyte membrane for lithium-ion batteries: Effect of prepolymer molecular weight. Journal of Membrane Science, 2016. 498: p. 208-217.

164. L. Z. Fan, Y. S. Hu, A. J. Bhattacharyya, and J. Maier, Succinonitrile as a versatile additive for polymer electrolytes. Advanced Functional Materials, 2007. 17(15): p. 2800-2807.

165. M. Zachariah, M. Romanini, P. Tripathi, M. Barrio, J. L. Tamarit, and R. Macovez, Self-Diffusion, Phase Behavior, and Li^+ Ion Conduction in Succinonitrile-Based Plastic Cocrystals. The Journal of Physical Chemistry C, 2015. 119(49): p. 27298-27306.

166. D. Devaux, R. Bouchet, D. Gle, and R Denoyel, Mechanism of ion transport in PEO/LiTFSI complexes: Effect of temperature, molecular weight and end groups. Solid State Ionics, 2012. 227: p. 119-127.

167. J. Wang, L. Fan, Q. Du, and K Jiao, Lithium ion transport in solid polymer electrolyte filled with alumina nanoparticles. Energy Advances, 2022. 1(5): p. 269-276.

168. D. J. Brooks, B. V. Merinov, W. A. Goddard, B. Kozinsky, and Jonathan Mailoa, et al., Atomistic Description of Ionic Diffusion in PEO-LiTFSI: Effect of Temperature, Molecular Weight, and Ionic Concentration. Macromolecules, 2018. 51(21): p. 8987-8995.

169. Y. Mallaiaha, V. R. Jeedi, R. Swarnalatha, A. Raju, S. N. Reddy, and A. S. Chary, Impact of polymer blending on ionic conduction mechanism and dielectric properties of sodium

based PEO-PVdF solid polymer electrolyte systems. Journal of Physics and Chemistry of Solids, 2021. 155: p. 110096.

170. M. Kerner, N. Plylahan, J. Scheers, and P. Johansson, Thermal stability and decomposition of lithium bis(fluorosulfonyl)imide(LiFSI) salts. Rsc Advances, 2016. 6(28): p. 23327-23334.

172. Frisch, M., et al., Fox Gaussian 09, Revision C. 01. Gaussian Inc, 2010.

173. A. Noorjahan, and P. Choi, Thermodynamic properties of poly(vinyl alcohol) with different tacticities estimated from molecular dynamics simulation. Polymer, 2013. 54(16): p. 4212-4219.

174. Y. Lv, and C. Ruan, Molecular dynamics simulation of nonisothermal crystallization of a single polyethylene chain and short polyethylene chains based on OPLS force field. E-Polymers, 2022. 22(1): p. 136-146.

175. R. Zangi, Refinement of the OPLSAA Force-Field for Liquid Alcohols. ACS Omega, 2018. 3(12): p. 18089-18099.

176. N. Molinari, J. P. Mailoa, B. Kozinsky, Effect of Salt Concentration on Ion Clustering and Transport in Polymer Solid Electrolytes: A Molecular Dynamics Study of PEO-LiTFSI. Chemistry of Materials, 2018. 30(18): p. 6298-6306.

177. M. I. Chaudhari, J. R. Nair, L. R. Pratt, F. A. Soto, P. B. Balbuena, and S. B. Rempe, Scaling atomic partial charges of carbonate solvents for lithium ion solvation and diffusion. Journal of Chemical Theory and Computation, 2016. 12(12): p. 5709-5718.

178. M. A. M. Marquez, M. Zarrabeitia, S. Passerini, and T. Rojo, Structure, Composition, Transport Properties, and Electrochemical Performance of the Electrode-Electrolyte

Interphase in Non-Aqueous Na-Ion Batteries. Advanced Materials Interfaces, 2022. 9(8): p. 2101773.

179. E. Jonsson, Ionic liquids as electrolytes for energy storage applications–A modelling perspective. Energy Storage Materials, 2020. 25: p. 827-835.

180. I. Leontyev, and A. Stuchebrukhov, Accounting for electronic polarization in non-polarizable force fields. Physical Chemistry Chemical Physics, 2011. 13(7): p. 2613-2626.

181. S. Mogurampelly, and V. Ganesan, Structure and mechanisms underlying ion transport in ternary polymer electrolytes containing ionic liquids. The Journal of Chemical Physics, 2017. 146(7).

182. L. T. Costa, B. Sun, F. Jeschull, and D. Brandell, Polymer-ionic liquid ternary systems for Li-battery electrolytes: Molecular dynamics studies of LiTFSI in a EMIm-TFSI and PEO blend. The Journal of Chemical Physics, 2015. 143(2).

183. S. Mohapatra, S. Sharma, A. Sriperumbuduru, S. R. Varanasi, and S. Mogurampelly, Effect of succinonitrile on ion transport in PEO-based lithium-ion battery electrolytes. The Journal of Chemical Physics, 2022. 156(21).

184. X. Chen, F. Chen, M. S. Liu, and M. Forsyth, Polymer architecture effect on sodium ion transport in PSTFSI-based ionomers: A molecular dynamics study. Solid State Ionics, 2016. 288: p. 271-276.

185. L. Meabe, S. R. Pena, M. M. Ibanez, Y. Zhang, E. Lobato, H. Manzano, M. Armand, J. Carrasco, and H. Zhang, et al., Insight into the ionic transport of solid polymer electrolytes in polyether and polyester blends. The Journal of Physical Chemistry C, 2020. 124(33): p. 17981-17991.

186. P. Kang, L. Wu, D. Chen, Y. Su, Y. Zhu, J. Lan, X. Yang, and G. Sui, Dynamical Ion Association and Transport Properties in PEO-LiTFSI Electrolytes: Effect of Salt Concentration. The Journal of Physical Chemistry B, 2022. 126(24): p. 4531-4542.

187. T. I. Morrow, and E. J. Maginn, Molecular dynamics study of the ionic liquid 1-n-butyl-3-methylimidazolium hexafluorophosphate. The Journal of Physical Chemistry B, 2002. 106(49): p. 12807-12813.

188. L. Breton, and G. L. Joly, Molecular modeling of aqueous electrolytes at interfaces: Effects of long-range dispersion forces and of ionic charge rescaling. The Journal of Chemical Physics, 2020. 152(24).

189. R. Ishizuka, N. Matubayasi, Self-consistent determination of atomic charges of ionic liquid through a combination of molecular dynamics simulation and density functional theory, Journal of Chemical Theory and Computation, 2016. 12(2): p. 804-811.

190. M. Buhl, A. Chaumont, R. Schurhammer, and G. Wipff, Ab initio molecular dynamics of liquid 1, 3-dimethylimidazolium chloride. The Journal of Chemical Physics B, 2005. 109(39): p. 18591-18599.

191. V. Chaban, Polarizability versus mobility: atomistic force field for ionic liquids. Physical Chemistry Chemical Physics, 2011. 13(35): p. 16055-16062.

192. T. G. Youngs, and C. Hardacre, Application of static charge transfer within an ionic-liquid force field and its effect on structure and dynamics. ChemPhysChem, 2008. 9(11): p. 1548-1558.

193. A. D. Becke, Density-Functional Thermochemistry. III. The Role of Exact Exchange. J. Chem. Phys., 98: 5648-5652. 1993.

194. Abraham, M., et al., the GROMACS development team, GROMACS User Manual version 2019. 2018.

195. B. Hess, H. Bekker, H. J. C. Berendsen, and J. G. E. M. Fraaije, LINCS: A linear constraint solver for molecular simulations. Journal of Computational Chemistry, 1997. 18(12): p. 1463-1472.

196. G. Bussi, D. Donadio, and M.. Parrinello, Canonical sampling through velocity rescaling. 2007. 126(1): p. 014101.

197. M. R. Shirts, D. L. Mobley, J. D. Chodera, and V. S. Pande, Accurate and Efficient Corrections for Missing Dispersion Interactions in Molecular Simulations. The Journal of Physical Chemistry B, 2007. 111(45): p. 13052-13063.

198. U. Essmann, L. Perera, M. L. Berkowitz, T. Darden, H. Lee and L. G. Pedersen, A smooth particle mesh Ewald method, Journal of Chemical Phyics. 1995. 103(19): p. 8577-8593.

199. L. Marinez, R. Andrade, E. G. Birgin, and J. M. Martinez, PACKMOL: a package for building initial configurations for molecular dynamics simulations. J. Comput Chem, 2009. 30(13): p. 2157-64.

200. Y. Zhao, D. Liu, H. Tang, J. Lu and F. Cui, A MD Simulation and Analysis for Aggregation Behaviors of Nanoscale Zero-Valent Iron Particles in Water via MS. The Scientific World Journal, 2014. 2014: p. 768780.

201. J. V. L. Mota, M. Albuquerque, D. Brandell, and L. T. Costa, Exploring structural and dynamical properties of polymer-ionic liquid ternary electrolytes for sodium ion batteries, Electrochimica Acta, 2023. 461: p. 142635.

202. L. J. Siqueira, and M. C. C. Ribeiro, Molecular dynamics simulation of the polymer electrolyte poly (ethylene oxide)/$LiClO_4$. II. Dynamical properties. The Journal of Chemical Physics, 2006. 125(21).

203. Z. J. Hoffman, D. B. Shah, and N. P. Balsara, Temperature and concentration dependence of the ionic transport properties of poly(ethylene oxide) electrolytes. Solid State Ionics, 2021. 370: p. 115751.

204. K. Timachova, H. Watanabe, and N. P. Balsara, Effect of Molecular Weight and Salt Concentration on Ion Transport and the Transference Number in Polymer Electrolytes. Macromolecules, 2015. 48(21): p. 7882-7888.

205. T. K. Mabuchi, K. Nakajima, and T. Tokumasu, Molecular Dynamics Study of Ion Transport in Polymer Electrolytes of All-Solid-State Li-Ion Batteries. Micromachines, 2021. 12(9): p. 1012.

206. M. S. Min, C. Booth, and V. M. Nace, Specific volumes of poly (oxybutylene) and poly (oxyethylene) dimethyl ethers in the liquid state. European Polymer Journal, 1997. 33(7): p. 991-996.

207. Tawfik, W.Y. and A.S. Teja, The densities of polyethylene glycols. Chemical Engineering Science, 1989. 44(4): p. 921-923.

208. K. Pozyczka, M. Marzantowicz, J. R. Dygas, and F. Krok, Ionic conductivity and lithium transference number of poly (ethylene oxide): LiTFSI system. Electrochimica Acta, 2017. 227: p. 127-135

209. F. S. Genier, and I. D. Hosein, Effect of coordination behavior in polymer electrolytes for sodium-ion conduction: a molecular dynamics study of poly (ethylene oxide) and poly (tetrahydrofuran). Macromolecules, 2021. 54(18): p. 8553-8562.

210. J. D. Londono, B. K. Annis, A. Habenschuss, O. Borodin, G. D. Smith, J. Z. Turner, and A. K. Soper, Cation Environment in Molten Lithium Iodide Doped Poly(ethylene oxide). Macromolecules, 1997. 30(23): p. 7151-7157.

211. A. F. Lanord, and J. C. Grossman, Correlations from Ion Pairing and the Nernst-Einstein Equation. Physical Review Letters, 2019. 122(13): p. 136001.

212. F. Baskoro, H. Q. Wong, and H. J. Yen, Strategic Structural Design of a Gel Polymer Electrolyte toward a High Efficiency Lithium-Ion Battery. ACS Applied Energy Materials, 2019. 2(6): p. 3937-3971.

213. G. Mao, M. L. Saboungi, D. L. Price, M. B. Armand, and W. S. Howells, Structure of Liquid PEO-LiTFSI Electrolyte. Physical Review Letters, 2000. 84(24): p. 5536-5539.

214. Q. Zheng, D. M. Pesko, B. M. Savoie, K. Timachova, A. L. Hasan, M. C. Smith, T. F. Miller, G. W. Coates, and N. P. Balsara, Optimizing Ion Transport in Polyether-Based Electrolytes for Lithium Batteries. Macromolecules, 2018. 51(8): p. 2847-2858.

215. D. M. Seo, P. D. Boyle, R. D. Sommer, J. S. Daubert, O. Borodin, and W. A. Henderson, Solvate Structures and Spectroscopic Characterization of LiTFSI Electrolytes. The Journal of Physical Chemistry B, 2014. 118(47): p. 13601-13608.

216. K. Pozyczka, M. Marzantowicz, J. R. Dygas, and F. Krok, Ionic conductivity and lithium transference number of poly (ethylene oxide): LiTFSI system, Electrochimica Acta, 2017. 227: p. 127-135.

217. Y. Wu, Y. Li, Y. Wang, Q. Liu, Q. Chen, and M. Chen, Advances and prospects of PVDF based polymer electrolytes. Journal of Energy Chemistry, 2022. 64: p. 62-84.

218. D. Diddens, and A. Heuer, Lithium ion transport mechanism in ternary polymer electrolyte-ionic liquid mixtures: A molecular dynamics simulation study. ACS Macro Letters, 2013. 2(4): p. 322-326.

219. M. H. Kowsari, S. Alavi, M. Ashrafizaadeh, and B. Najafi, Molecular dynamics simulation of imidazolium-based ionic liquids. I. Dynamics and diffusion coefficient, Journal of Chemical Physics 2008. 129(22).

220. O. Borodin, and G. D. Smith, Mechanism of Ion Transport in Amorphous Poly(ethylene oxide)/LiTFSI from Molecular Dynamics Simulations. Macromolecules, 2006. 39(4): p. 1620-1629.

221. W. Gorecki, M. Jeannin, E. Belorizky, C. Roux, and M. Armand, Physical properties of solid polymer electrolyte PEO (LiTFSI) complexes. Journal of Physics: Condensed Matter, 1995. 7(34): p. 6823.

222. S. Bhattacharja, S. Smoot, and D. H. Whitmore, Cation and anion diffusion in the amorphous phase of the polymer electrolyte $(PEO)_8LiCF_3SO_3$. Solid State Ionics, 1986. 18: p. 306-314.

223. H. Hafezi, and J. Newman, Verification and analysis of transference number measurements by the galvanostatic polarization method. Journal of the Electrochemical Society, 2000. 147(8): p. 3036.

224. G Oradd, L. Edman, and A. Ferry, Diffusion: A comparison between liquid and solid polymer LiTFSI electrolytes. Solid State Ionics, 2002. 152: p. 131-136.

225. B. M. Savoie, M. A. Webb, and T. F. Miller, Enhancing cation diffusion and suppressing anion diffusion via Lewis-acidic polymer electrolytes. J. Phys. Chem, 2017. 8(3): p. 641-646.

226. P. G. Bruce, Solid state electrochemistry / edited by Peter G. Bruce. Chemistry of solid State Materials ; [5], ed. P.G. Bruce. 1995, Cambridge ; New York, NY, USA: Cambridge University Press.

227. D. M. Pesko, K. Timachova, R. Bhattacharya, M. C. Smith, I. Villaluenga, J. Newman, and N. P. Balsara, Negative transference numbers in poly(ethylene oxide)-based electrolytes. Journal of The Electrochemical Society, 2017. 164(11): p. E3569.

228. M. Siekierski, M. Bukat, M. Ciosek, M. Piszcz, and M. M. Szerszen, Transference Number Determination in Poor-Dissociated Low Dielectric Constant Lithium and Protonic Electrolytes. Polymers, 2021. 13(6).

229. E. E. Ushakovaabd, A. V. Sergeev, A. Morzhukhin, F. S. Napolskiy, O. Kristavchuk, A. V. Chertovich, L. V. Yashina and D. M. Itkis, Free-standing $Li^{(+)}$-conductive films based on PEO-PVDF blends. RSC Adv, 2020. 10(27): p. 16118-16124.

230. Paul Bauer, B.H., & Erik Lindahl., GROMACS 2022.5 Source code (2022.5). Zenodo. (2023).

Appendix A. GROMACS Programs

This information is based on the GROMACS reference manual and user guide.[193]

GROMACS program	Description	Output
gmx pdb2gmx	to introduce a new residue into an existing force field	generates coordinates (.gro) and topology (.itp) file in GROMACS format
gmx editconf	to move the molecule a little bit off center	Rescaled structure files (.pdb, .gro)
gmx insert-molecules	inserts n copies of the system specified in the input file into a new or existing system	Structure files with new added number of molecules (.pdb, .gro)
gmx grompp	Reads the topology file, checks the validity of the file, expands the topology from a molecular description to an atomic description. Also checks the parameters used for MD run.	A binary file is produced that can serve as the sole input file for the MD program

gmx mdrun	It is the main computational chemistry engine in gromacs. It can conducts MD simulations, e.g. energy minimization or n equilibration run of a system under isothermal-isobaric or isothermal-isochoric conditions.	A new set of files that describes the newly simulated system
gmx energy	Extracts energy components from an energy file (.edr) by making the user select which energy component to be studied.	.xvg file (used for plotting graphs) of selected energy configuration and displays averages of the selected energy.
gmx convert-tpr	Modifies the number of steps in a run input file.	Modified run input file, so the simulation can be extended by further simulation steps
gmx rdf	Calculates radial distribution functions in different.	Returns the RDF over time in a .xvg file.

gmx msd	It computes the mean square displacement (MSD) of atoms from a set of initial positions.	Returns the MSD over time in a .xvg file. This also provides diffusion constant using the Einstein relation.
gmx make_index	It ca generate the index file of all atoms and molecules.	An index file with default groups of a complete system and individual molecules

Appendix B. GROMACS Code and Simulation Setup

I utilized GROMACS (version 2022.5) to perform the molecular dynamics simulations. The source code can be found on the official GROMACS website.[230] Below is the code snippet used to set up the simulations.

B.1 Energy Minimization

```
; Parameters describing what to do, when to stop, and what to save
 integrator     = steep    ; Algorithm (steep = steepest descent minimization)
 emtol          = 10.0     ; Stop minimization when the maximum force < 10.0 kJ/mol/nm
 emstep         = 0.0005  ; Minimization step size
 nsteps         = 500000 ; Maximum number of (minimization) steps to perform
 constraints    =  none
 nstenergy      =  500
; Parameters describing how to find the neighbors of each atom and how to calculate the interactions

 nstlist         = 10       ; Frequency to update the neighbor list and long range forces
 cutoff-scheme   = Verlet  ; Buffered neighbor searching
 ns_type         = grid     ; Method to determine neighbor list (simple, grid)
 coulombtype     = PME     ; Treatment of long range electrostatic interactions
 rcoulomb        = 1        ; Short-range electrostatic cut-off
 rvdw            = 1        ; Short-range Van der Waals cut-off
 pbc             = xyz      ; Periodic Boundary Conditions in all 3 dimensions
```

B.2 Equilibration Run

```
; Preprocessing
 ;define          = -DPOSRES  ; defines to pass to the preprocessor
; Run Control
 integrator      = md         ; md integrator
 tinit           = 0          ; [ps] starting time for run
 dt              = 0.001      ; [ps] time step for integration
 nsteps          = 25000000    ; maximum number of steps to integrate, 0.001 * 25000000 =
                 25 ns
; Output Control
 nstxout         = 500        ; [steps] freq to write coordinates to trajectory
 nstvout         = 500        ; [steps] freq to write velocities to trajectory
 nstfout         = 500        ; [steps] freq to write forces to trajectory
 nstlog          = 500        ; [steps] freq to write energies to log file
 nstenergy       = 500        ; [steps] freq to write energies to energy file
 nstxout-        = 500        ; [steps] freq to write coordinates to xtc trajectory
 compressed
 compressed-     = 500       ; [real] precision to write xtc trajectory
 x-precision
 compressed-     = System    ; group(s) to write to xtc trajectory
 x-grps
 energygrps      = System    ; group(s) to write to energy file
; Neighbor Searching
```

```
 cutoff-scheme   = Verlet
 nstlist         = 10        ; [steps] freq to update neighbor list
 ns_type         = grid      ; method of updating neighbor list
 pbc             = xyz       ; periodic boundary conditions in all directions
 rlist           = 1.2       ; [nm] cut-off distance for the short-range neighbor list
;VdW
 vdwtype         = cut-off   ; twin-range cut-off with rlist where rvdw >= rlist
 rvdw            = 1.1       ; [nm] distance for LJ cut-off
 vdw-modifier    = Potential-shift ; Smoothly switches the potential to zero between rvdw-switch
                   and rvdw.
 rvdw-switch     = 1.095     ;  switching interaction energy to zero over last 0.5 A
 DispCorr        = EnerPres  ; apply long range dispersion corrections
; 7.3.10 Electrostatics
 coulombtype     = PME       ; Particle-Mesh Ewald electrostatics
 rcoulomb        = 1.2       ; [nm] distance for Coulomb cut-off
; 7.3.13 Ewald
 fourierspacing  = 0.12      ; [nm] grid spacing for FFT grid when using PME
 pme_order       = 4         ; interpolation order for PME, 4 = cubic
 ewald_rtol      = 1e-5        ; relative strength of Ewald-shifted potential at rcoulomb
; 7.3.14 Temperature Coupling
 tcoupl          = V-rescale   ; temperature coupling with Berendsen-thermostat
```

```
  tc_grps              = system           ; groups to couple seperately to temperature bath
  tau_t                =   0.2            ; [ps] time constant for coupling
  ref_t                = 298.15           ; [K] reference temperature for coupling
; Pressure Coupling
  pcoupl                  = berendsen    ; pressure coupling where box vectors are variable
  pcoupltype              = isotropic     ; pressure coupling in x-y-z directions
  tau_p                   = 0.5           ; [ps] time constant for coupling
  compressibility         = 4.5e-5 4.5e-5 4.5e-5            ; [bar^-1] compressibility
  ref_p                   = 1.01325 ;bar ; [bar] reference pressure for coupling
  refcoord_scaling        = com
; 7.3.17 Velocity Generation
  gen_vel                 = no              ; velocity generation turned off
; Bonds
  constraints                 = h-bonds   ; convert all bonds to constraints
  constraint_algorithm        = LINCS     ; LINear Constraint Solver
  continuation                = yes        ; apply constraints to the start configuration
  lincs_order                 = 4            ; highest order in the expansion of the contraint coupling
                              matrix
  lincs_iter                  = 1            ; number of iterations to correct for rotational lengthening
  lincs_warnangle             = 30           ; [degrees] maximum angle that a bond can rotate before
                              LINCS will complain
```

B.3 Production Run

```
; Preprocessing
 ;define          = -DPOSRES         ; defines to pass to the preprocessor
; Run Control
 integrator       = md               ; md integrator
 tinit            = 0                ; [ps] starting time for run
 dt               = 0.001            ; [ps] time step for integration
 nsteps           = 250000000             ; maximum number of steps to integrate, 0.001 *
                  250000000 = 250 ns
; Output Control
 nstxout          = 500               ; [steps] freq to write coordinates to trajectory
 nstvout          = 500              ; [steps] freq to write velocities to trajectory
 nstfout          = 500              ; [steps] freq to write forces to trajectory
 nstlog           = 500              ; [steps] freq to write energies to log file
 nstenergy        = 500              ; [steps] freq to write energies to energy file
 nstxout-         = 500              ; [steps] freq to write coordinates to xtc trajectory
 compressed
 compressed-      = 500              ; [real] precision to write xtc trajectory
 x-precision
 compressed-      = System           ; group(s) to write to xtc trajectory
 x-grps
```

```
  energygrps        = System              ; group(s) to write to energy file
; Neighbor Searching
  cutoff-scheme     = Verlet
  nstlist           = 10                   ; [steps] freq to update neighbor list
  ns_type           = grid                 ; method of updating neighbor list
  pbc               = xyz                  ; periodic boundary conditions in all directions
  rlist             = 1.2                  ; [nm] cut-off distance for the short-range neighbor list
;VdW
  vdwtype           = cut-off              ; twin-range cut-off with rlist where rvdw >= rlist
  rvdw              = 1.1                  ; [nm] distance for LJ cut-off
  vdw-modifier      = Potential-shift      ; Smoothly switches the potential to zero between rvdw-
                    switch and rvdw.
  rvdw-switch       = 1.095                ;  switching interaction energy to zero over last 0.5 A
  DispCorr          = EnerPres             ; apply long range dispersion corrections
; 7.3.10 Electrostatics
  coulombtype       = PME                  ; Particle-Mesh Ewald electrostatics
  rcoulomb          = 1.2                  ; [nm] distance for Coulomb cut-off
; 7.3.13 Ewald
  fourierspacing    = 0.12                 ; [nm] grid spacing for FFT grid when using PME
  pme_order         = 4                    ; interpolation order for PME, 4 = cubic
  ewald_rtol        = 1e-5                 ; relative strength of Ewald-shifted potential at rcoulomb
; 7.3.14 Temperature Coupling
```

```
  tcoupl              = V-rescale          ; temperature coupling with Berendsen-thermostat
  tc_grps             = system             ; groups to couple seperately to temperature bath
  tau_t               =   0.2              ; [ps] time constant for coupling
  ref_t               = 298.15             ; [K] reference temperature for coupling
; Pressure Coupling
  pcoupl                = berendsen        ; pressure coupling where box vectors are variable
  pcoupltype            = isotropic         ; pressure coupling in x-y-z directions
  tau_p                 = 0.5               ; [ps] time constant for coupling
  compressibility       = 4.5e-5 4.5e-5 4.5e-5              ; [bar^-1] compressibility
  ref_p                 = 1.01325 ;bar      ; [bar] reference pressure for coupling
  refcoord_scaling      = com
; 7.3.17 Velocity Generation
  gen_vel              = yes                  ; velocity generation turned off
; Bonds
  constraints                = h-bonds        ; convert all bonds to constraints
  constraint_algorithm       = LINCS        ; LINear Constraint Solver
  continuation               = yes            ; apply constraints to the start configuration
  lincs_order                = 4             ; highest order in the expansion of the contraint coupling
                               matrix
  lincs_iter                 = 1             ; number of iterations to correct for rotational lengthening
  lincs_warnangle            = 30           ; [degrees] maximum angle that a bond can rotate before
                               LINCS will complain
```